POLITECNICO DI TORINO

Corso di Laurea Magistrale

in ingegneria civile

Tesi di Laurea Magistrale

Numerical models of punching shear of reinforced slabs without shear reinforcement

Relatore:
Prof. Gabriele Bertagnoli

……

Autore:
Benedetto La Fauci

……

ANNO ACCADEMICO 2017-2018

Acknowledgments

First and foremost I would like to thank Professor Antonio Marì and Dr. Noemi Duarte for their guidance during my work on this thesis during my experience abroad.

I also would like to thank Prof. Gabriele Bertagnoli, that helped me in further improvements on this work.

Finally I want to thank my family that always supported me during these years far away from them.

Contents

Chapter 1

introduction

Punching shear is a type of failure of reinforced concrete slabs subjected to high localized forces. In flat slab structures this occur at columns support points and in this situation the failure is due to shear.

This type of failure is catastrophic because no visible signs are shown prior to failure (brittle failure). Punching shear failure disasters have occurred several times in this past decades [1], [2], [3].

A typical flat plate punching shear failure is characterized by the slab failing at the intersection point of the column. This results in the column breaking through the portion of the surrounding slab. This type of failure is one of the most critical problems to consider when determining the thickness of flat plates at the column-slab intersection, accurate prediction of punching shear strength is a major concern and absolutely necessary for engineers so they can design a safe structure.

Figure 1.1: Punching failure of a slab with the typical view of the slab portion outside the shear crack.

This brittle failure was examined by many researchers in the form of tests, analytical models, and finite element analyses. Several researchers proposed empirical equations based on tests observations, which provide the basis of the existing design codes [4], [5], [6], [7].

The existing punching shear testing database, even though it is large, cannot address all aspects of punching shear stress transfer mechanisms. Therefore, in modern research in structural engineering, finite element analyses (FEA) are essential for supplementing experimental research in providing insights into structural behaviour, and, in the case presented, on punching shear transfer mechanisms. The work described herein, is on modelling concrete slab-column using a 3D analysis, in order to investigate the behaviour of this structures and to verify a new model for punching proposed by Prof. Antonio Marí Bernat [8].

Flat slabs simulations with nonlinear finite element analyses have been performed using the software MIDAS FEA. Initially, have been conducted experiments in order to validate if the modelling technique, the FE-analyses showed good agreement for peak loads and structural responses during loading.

A geometrically simple prototype of a reinforced concrete slab supported on its centre by a column was used in the present work, then other two slabs (edge and corner) were simulated. The critical events that preceded punching failure were similar to what had been observed in previous investigations where concrete columns were employed.

The sensitivity of the material and the FEA model to various parameters is discussed. The constitutive model is described in detail, including the effects of various material parameters on the accuracy of the analysis. Then, the finite element simulation results are presented. The numerical results are compared to the test results in terms of forces and deflections.

The aim of this work is to present the effectiveness of the proposed calibrated finite element model in describing and analyzing punching shear tests by identifying key parameters of the model. Furthermore, a new mechanical model for the estimation of the punching shear strength of reinforced concrete slabs without shear reinforcement is presented. The model is an adaption of a previously existing model for shear strength, developed by the authors A.Marí, A.Cladera, J. Bairán, C. Ribas, E. Oller, N. Duarte [8], which incorporates the contribution of the main shear resisting mechanisms. This model's accuracy is strengthened by comparing its hypothesis of multiaxial state of stresses in the compressed zone with the FEA results, which shows a satisfactory similarity in terms of stresses distribution.

Chapter 2

State of knowledge

2.1 Punching shear models

Several researchers have conducted laboratory tests to study the structural behaviour of reinforced concrete slabs supported on columns. In the available literature two major groups of tests can be distinguished. The first group deals with punching failure where the shear stress in the vicinity of the column is assumed to be uniform, which is the case for most interior columns. The other group deals with non-symmetric shear stresses around the column due to unbalanced moments over the column.

The available experiments can be divided into yet another two groups; those with and those without shear reinforcement. In the present study shear reinforced flat slabs have not been treated.

In this chapter are presented the principal models that have been developed through the past decades.

2.1.1 Kinnunen and Nylander (1960)

The structural response of reinforced concrete slabs supported on interior columns was experimentally investigated by Kinnunen and Nylander (1960) [4]. The test specimens consisted of circular slab portions supported on circular columns placed in its centre and loaded along the circumference. Kinnunen and Nylander observed two main failure modes; namely, yielding of the flexural reinforcement at small reinforcement ratios (failure in bending) and failure of the slab along a conical crack within which a concrete plug was punched.

The initiation of cracking was similar in all the test specimens that suffered punching failure, starting with the formation of flexural cracks in the bottom surface of the slab caused by moments.

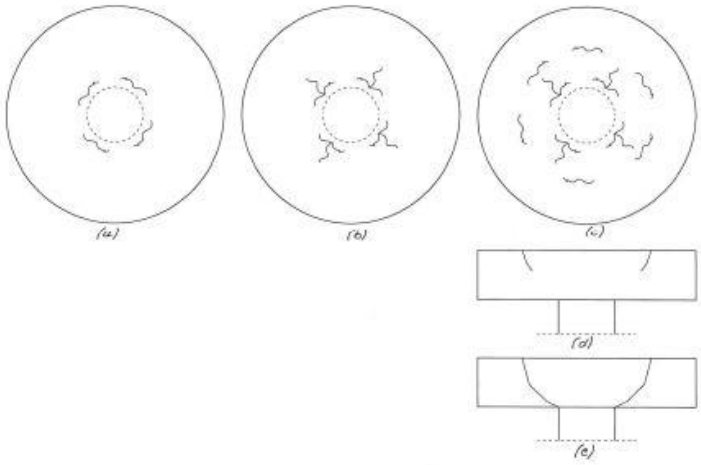

Figure 2.1: Crack propagation for Kinnunen's and Nylander's tests on centrically supported slabs.

On the basis of their test results, Kinnunen and Nylander developed a rational theory for the estimation of the punching shear strength in the early 1960s based on the assumption that the punching strength is reached for a given critical rotation ψ, not only did the model agree well with the test results, it was also the first model that thoroughly described the flow of forces.

Their observations during the tests led to the mechanical model, illustrated in Figure 2.2. They divide the slab outside the shear crack into sectors/elements between radial cracks. Each element is assumed to act as a rigid body supported by an imaginary conical shell in the part of the slab immediately above the column (see Figure 2.2).

Failure is assumed to occur when the stress in the conical shell and the compression strain in the tangential direction reach critical values.

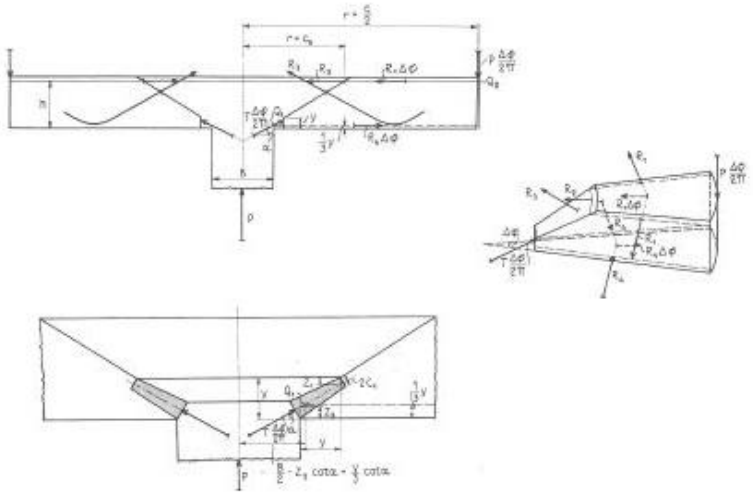

Figure 2.1: Mechanical model developed by Kinnunen and Nylander (1960).

Kinnunen in 1971 continued his research on punching shear with an investigation on flat slabs supported at their edges [5].

Thus far, this proposal remains one of the best models for the phenomenon of punching. Subsequently, some improvements were proposed by and Carl Erik Broms (1990) [6] to account for size effects and the effect of increasing concrete brittleness.

2.1.2 Broms (1990)

While very elegant and leading to good results, this model was never directly included in codes of practice because its application is too complex. Punching failure is here treated in a manner similar to Kinnunen and Nylander's but which utilizes generally recognized values for concrete properties, different compression zone heights in radial and tangential directions, and more realistic position for the bottom of the stable shear crack.

The author's hypothesis is that punching occurs when the concrete in compression near the column is distressed by either a high circumferential strain or a high radial stress V_c and V_σ denote the corresponding ultimate capacities.

For the high tangential compression strain failure mechanism is considered a uniaxially compressed cylinder specimen. It behaves elastically up to a strain of 0.0008, so when the specimen is strained to more than 0.0008, the behaviour of the specimen changes.

Now consider the compression zone in a flat plate between the inclined shear crack and the column face (Figure 2.2).

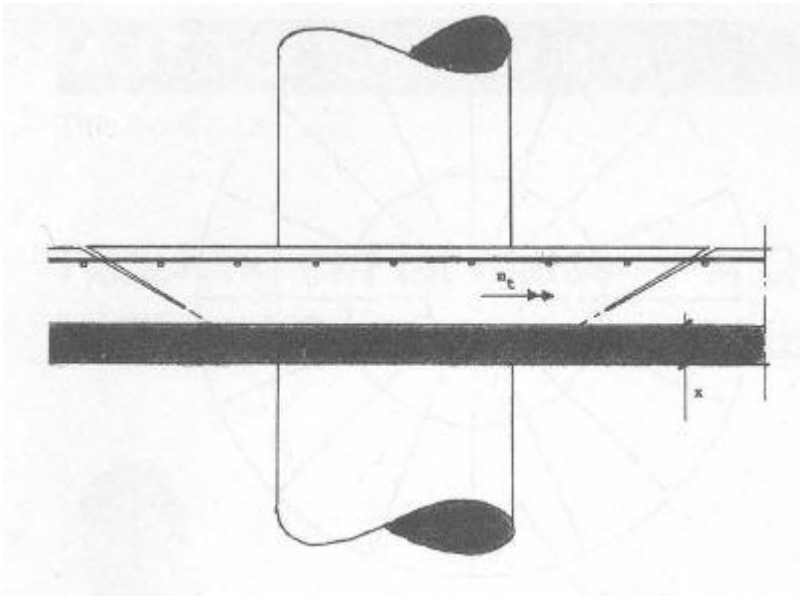

Figure 2.1: High tangential compression strain failure mechanism by Broms (1990).

If the tangential concrete strain exceeds 0.0008 macro cracks will start to form. It is then possible for the inclined shear crack to propagate to the column face and cause punching to occur.

Small slabs exhibit a concrete strain capacity greater than 0.008 due to size effect and different concrete grades show an increasing brittleness (decreasing strain capacity) with increasing strength. This two conditions are assumed to affect the critical value ε_{cpu} , once the critical value ε_{cpu} is determined, then the punching failure load V_c can be calculated.

The second punching failure mechanism is the high radial compression stress failure mechanism. Looking at the compression zone in the vicinity of the column, as shown in Figure 2.2. The column force V is transferred to the slab via inclined radial forces that must pass under the root of the shear crack.

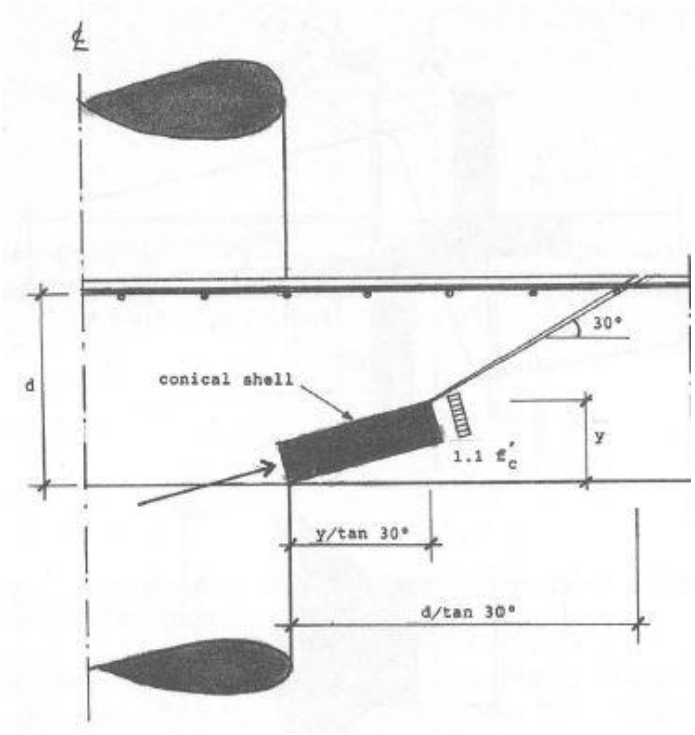

Figure 2.2: High radial compression stress failure mechanism by Broms (1990).

The inclination of the crack is assumed to be 30 degrees, which is in conformity with test results. The radially compressed concrete is assumed to form an imaginary conical shell with constant thickness.

Punching is assumed to occur when the stress in the conical shell reaches the value $1.1f_c'$ (where f_c' is the specified compressive strength of concrete in psi) at the bottom of the shear crack. The factor 1.1 is applied since some strength increase can be anticipated due to the concrete being biaxially stressed. The punching load V_σ can now be determined by the condition of equilibrium in the vertical direction.

2.1.3 Guandalini, Burdet and Muttoni (2009)

Muttoni (2008) [9] gave evidence supporting the role of the shear critical crack in the punching shear strength. Muttoni presented a mechanical explanation of the phenomenon of punching shear on the basis of the opening of a critical shear crack. It leads to the formulation of a new failure criterion for punching shear based on the rotation of a slab. This criterion correctly describes punching shear failures observed in experimental testing, even in slabs with low reinforcement ratios. The critical shear crack theory describes the relationship between the punching shear strength of a slab and its rotation at failure. After reaching a maximum level, the radial compressive strain decreases; and shortly before punching, tensile

strains may be observed. These strains can be explained by the development of an elbow shaped strut (Figure. 2.3) with a horizontal tensile member along the soffit due to the development of the critical shear crack.

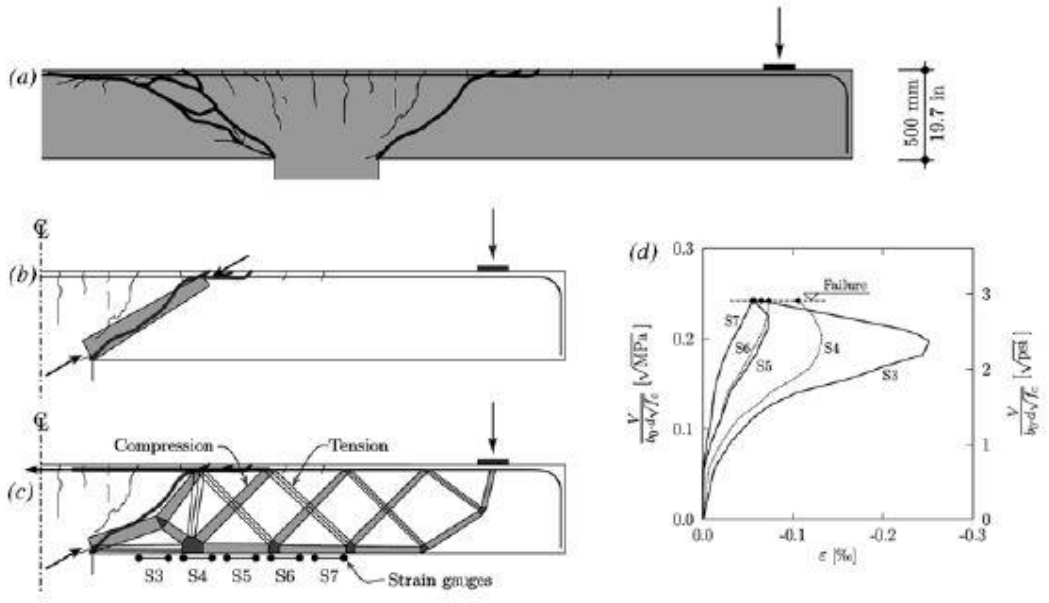

Figure 2.3: Test by Guandalini and Muttoni: (a) cracking pattern of slab after failure; (b) theoretical strut developing across the critical shear crack; (c) elbow-shaped strut; and (d) plots of measured radial strains in soffit of slab as function of applied load, Muttoni (2008).

Also, experimental results on slabs with a particular lay-out of circular reinforcement in which only radial cracks form and in which the formation of circular cracks is avoided, confirmed the role of the critical shear crack.

Then in 2009 the critical shear crack theory is described in Guandalini, Burdet and Muttoni.

This theory is based on the assumption that the shear strength of members without transverse reinforcement is governed by the width and roughness of an inclined shear crack that develops through the inclined compression strut carrying shear. In two-way slabs the width w_c of the critical shear crack is assumed proportional to the slab rotation ψ and the effective depth d of the member (Fig. 2.4).

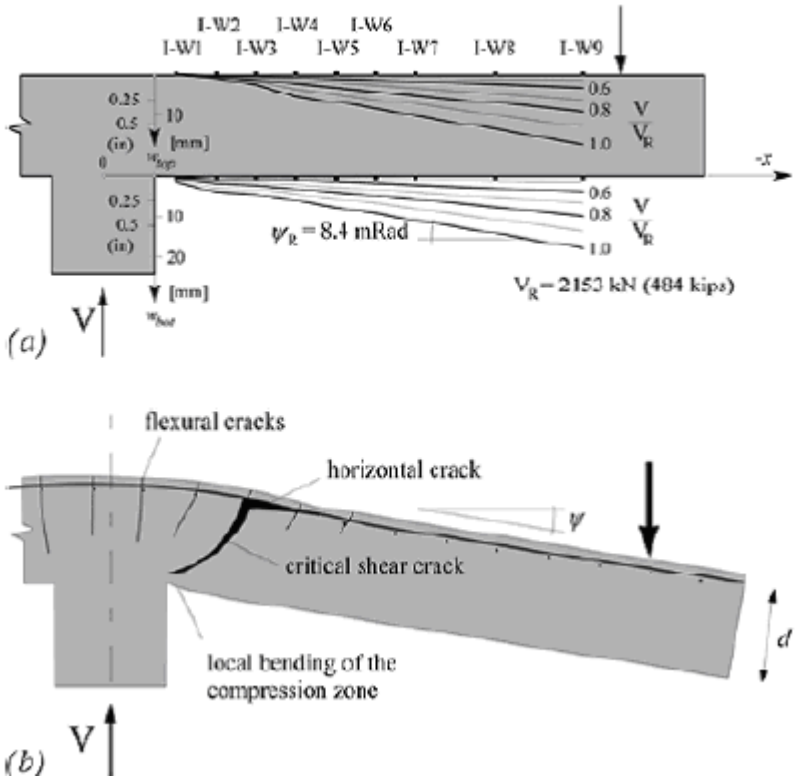

Figure 2.3: Slab deflection during punching test: (a) measured values of *w* at top and bottom face of a slab tested by Guandalini, Burdet and Muttoni (2009); and (b) interpretation of measurements according to critical shear crack theory.

The failure load is obtained at the intersection (Figure. 2.4) of the failure criterion with the load-rotation curve of the slab.

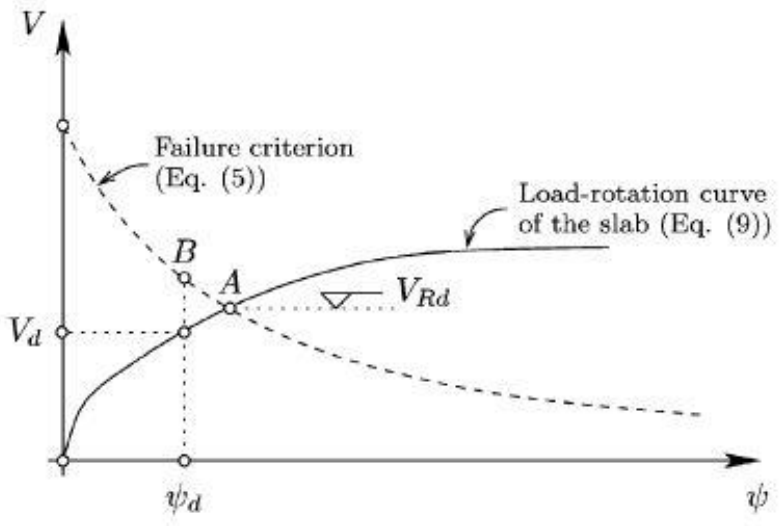

Figure 2.4: Design procedure to check punching strength of slab.

According to Muttoni, the load-rotation relationship can, in a more general case, be obtained from a nonlinear numerical simulation of the flexural behavior of the slab, or in the axial symmetric case by a numerical integration of the moment-curvature relationship.

An advantage of this method is that it finds the value of the rotation capacity of the slab, and thus of its ductility. Due to the relation between the shear carried across a crack and the depth of a section, this method takes the size effect into account.

2.2 Code provisions

2.2.1 Eurocode 2, EN 1992-1-1: 2004 [10]

Punching shear can result from a concentrated load or reaction acting on a relatively small area, called the loaded area A_{load} of a slab or a foundation. The shear resistance should be checked at the face of the column and at the basic control perimeter u_1.

An appropriate verification model for checking punching failure at the ultimate limit state is shown in Figure 2.5.

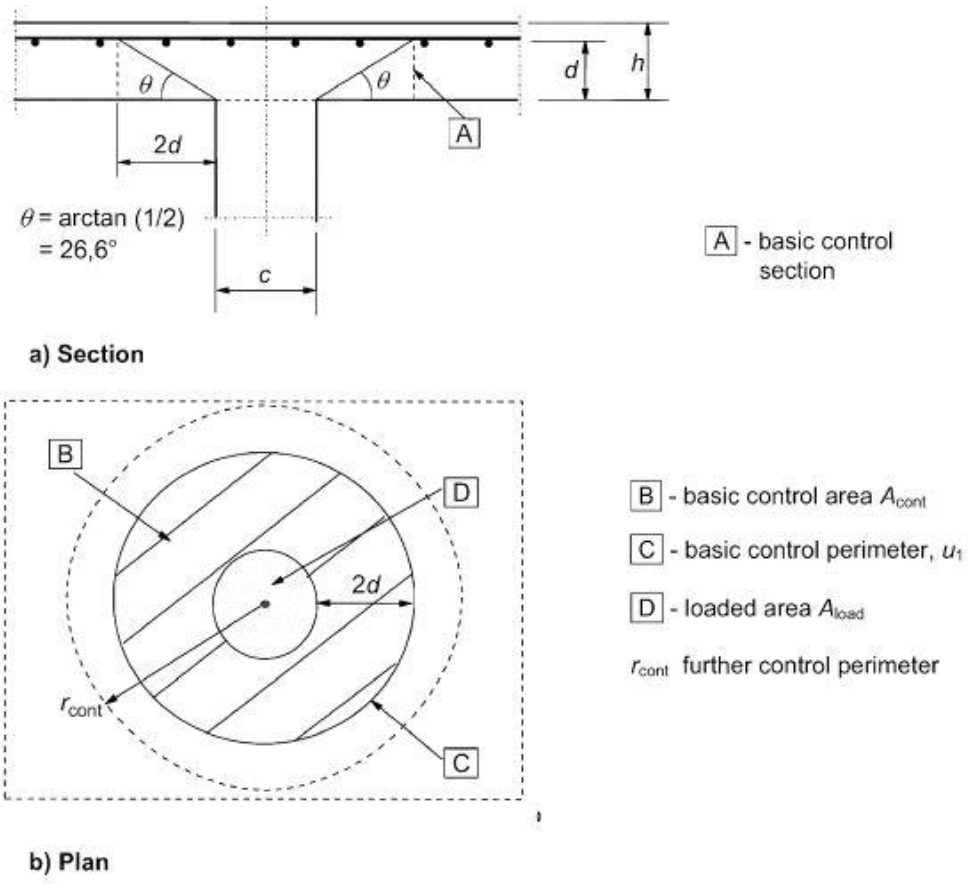

Figure 2.5: Verification model for punching shear at the ultimate limit state

The basic control perimeter u_1 may normally be taken to be at a distance *2d* from the loaded area and should be constructed so as to minimize its length (Figure 2.6).

The effective depth of the slab is assumed constant and may normally be taken as:

$$d_{eff} = \frac{\left(d_y + d_z\right)}{2} \tag{2.1}$$

where d_y and d_z are the effective depths of the reinforcement in two orthogonal directions.

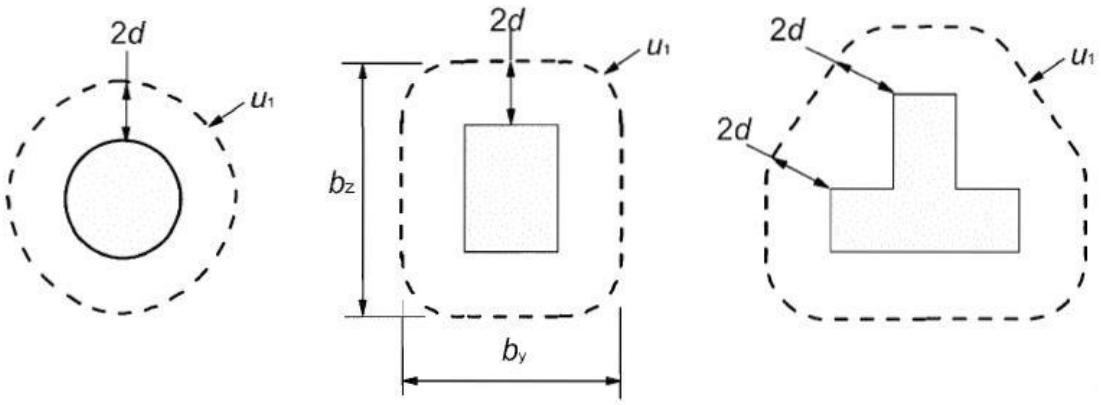

Figure 2.6: Typical basic control perimeters around loaded areas

Control perimeters at a distance less than *2d* should be considered where the concentrated force is opposed by a high pressure (e.g. soil pressure on a base), or by the effects of a load or reaction within a distance *2d* of the periphery of area of application of the force.

For a loaded area situated near an edge or a corner, the control perimeter should be taken as shown in Figure 2.7, if this gives a perimeter (excluding the unsupported edges) smaller than that obtained from Figure 2.6 above.

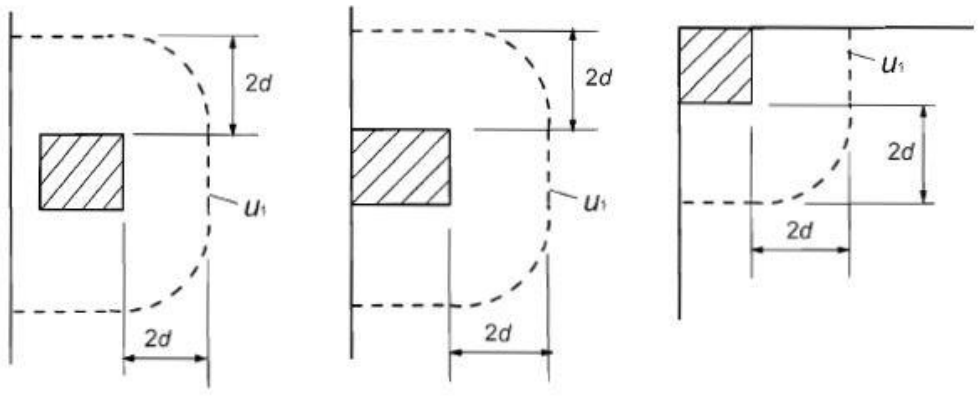

Figure 2.7: Basic control perimeters for loaded areas close to or at edge or corner

The control section is that which follows the control perimeter and extends over the effective depth *d*. For slabs of constant depth, the control section is perpendicular to the middle plane of the slab.

The design procedure for punching shear is based on checks at the face of the column and at the basic control perimeter u_1.

The design shear stress (MPa) along the control sections, is $V_{Rd,c}$:

$V_{Rd,c}$ is the design value of the punching shear resistance of a slab without punching shear reinforcement along the control section considered.

The check that should be carried out is: $V_{Ed} \le V_{Rd,c}$

Where the support reaction is eccentric with regard to the control perimeter, the maximum shear stress should be taken as:

$$v_{Ed} = \beta \frac{V_{Ed}}{u_1 d} \tag{2.2}$$

Where:

d is the mean effective depth of the slab, which may be taken as $\left(d_y + d_z\right)/2$ where:

d_y, d_z is the effective depths in the y- and z- directions of the control section.

u_1 is the length of the control perimeter being considered.

For structures where the lateral stability does not depend on frame action between the slabs and the columns, and where the adjacent spans do not differ in length by more than 25%, approximate values for β may be used as it shown in Figure 2.8.

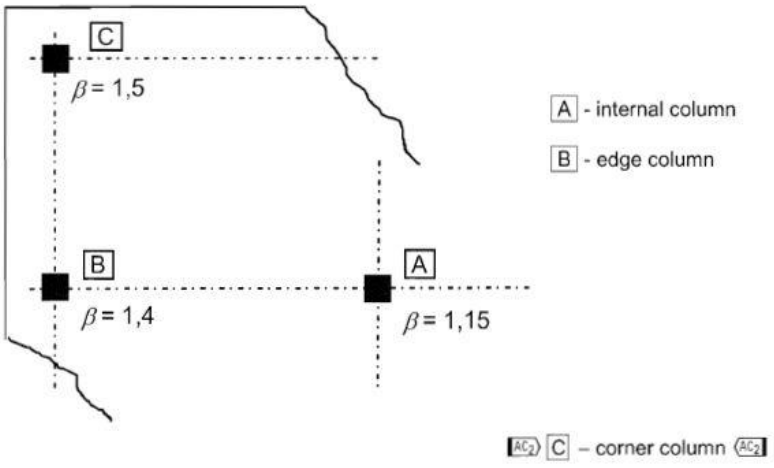

Figure 2.8: Recommended values of β.

The design punching shear resistance [MPa] may be calculated as follows:

$$v_{Rd,c} = C_{Rd,c} k \left(100 \cdot \rho_l \cdot f_{ck}\right)^{1/3} + k_1 \sigma_{cp} \geq \left(v_{\min} + k_1 \sigma_{cp}\right) \tag{2.3}$$

Where:

f_{ck} is the characteristic concrete strength in MPa.

d is the effective depth in mm.

$k = 1 + \sqrt{\frac{200}{d}} \leq 2$

$\rho_l = \sqrt{\rho_{ly} \cdot \rho_{lz}} \leq 0.02$ is the length of the control perimeter being considered.

$\rho_{ly} \cdot \rho_{lz}$ relate to the bonded tension steel in y- and z- directions respectively. The values ρ_{ly} and ρ_{lz} should be calculated as mean values taking into account a slab width equal to the column width plus 3d each side.

$\sigma_{cp} = \left(\sigma_{cy} + \sigma_{cz}\right) / 2$

σ_{cy}, σ_{cz} are the normal concrete stresses in the critical section in y- and z directions (Mpa, positive if compression):

$\sigma_{cy} = \frac{N_{Ed,y}}{A_{cy}}$ and $\sigma_{cz} = \frac{N_{Ed,z}}{A_{cz}}$

$N_{Ed,y}$ and $N_{Ed,z}$ are the longitudinal forces across the full bay for internal columns and the longitudinal force across the control section for edge columns. The force may be from a load or prestressing action.

A_c is the area of concrete according to the definition of N_{Ed}

The values of the parameters depend on the National Annex. The recommended values are:

$C_{Rd,c} = \frac{0{,}18}{\gamma_c}$ with $\gamma_c = 1.5$

$v_{\min} = 0.035 k^{3/2} f_{ck}^{1/2}$

$k_1 = 0.1$

The punching resistance of column bases should be verified at control perimeters within *2d* from the periphery of the column.

2.2.2 fib Model Code 2010

The provisions of *fib* Model Code 1990 are the basis of the present Eurocode 2 as only minor adjustments were carried out. The *fib* Model Code 2010 [11] provides a new design concept for punching shear based on critical shear crack theory developed by Muttoni (2008) [9]. In this physical In this physical model with empirical adjustment factors, the punching shear resistance depends on the width of the critical shear crack, which is related to the slab rotation. The design model was derived from punching shear tests on isolated flat slab elements, but the model can also be used for ground slabs and footings.

As the Eurocode 2, the check that should be carried out is: $V_{Ed} \leq V_{Rd,c}$

$$V_{Rd,c} = k_{\psi} \frac{\sqrt{f_{ck}}}{\gamma_c} b_0 d_v \tag{2.4}$$

Where:

f_{ck} is the characteristic concrete strength in MPa.

d_v is the shear resisting effective depth (distance between centroid of flexural reinforcement and surface at which slab is supported.

$\gamma_c = 1.5$ is the partial safety factor for concrete.

The parameter k_{ψ} considers the influence of the width of the critical shear crack and depends on the slab rotation ψ and the maximum aggregate size.

$$k_{\psi} = \left(1.5 + 0.9\ \psi\ d\ k_{dg}\right)^{-1} \leq 0.6 \tag{2.5}$$

Where:

d is the mean value of the flexural effective depth in mm.

$k_{dg} = \frac{32}{\left(16 + d_g\right)} \geq 0.75$ (with d_g in mm), considers the influence of the aggregate size.

The critical shear resisting perimeter can be estimated as:

$$b_0 = k_e b_{1,red} \tag{2.6}$$

k_e accounts for a non-symmetrical shear stress distribution along the critical perimeter. In non-sway systems and where differences between adjacent spans are <25%, this factor may be taken as 0.9, 0.7 and 0.65 for interior, edge and corner columns, respectively.

$b_{1,red}$ is the basic control perimeter at a distance $0.5d$ from the periphery of the loaded area (Figure 2.9).

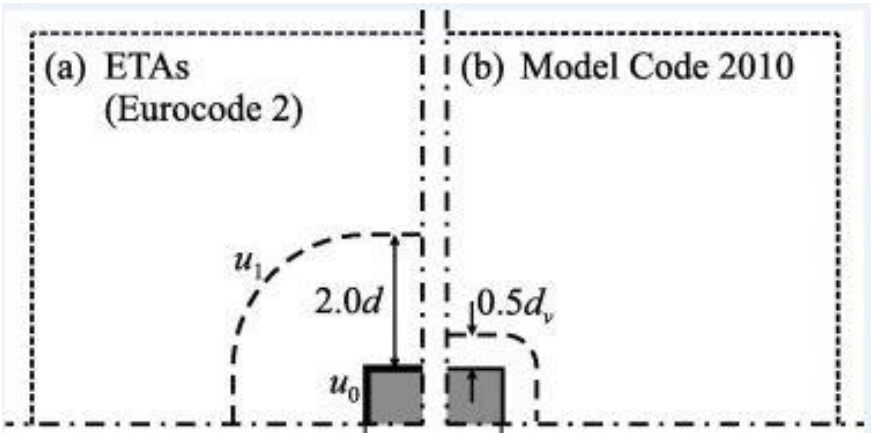

Figure 2.9: Design perimeters according to Eurocode 2 (a) and *fib* Model Code 2010 (b).

The Model Code 2010 introduced different levels of approximation (LoA) from LoAI to LoAIV, with increasing accuracy of determination of the slab rotation ψ.

As LoA increases, so the calculated slab rotations generally decrease, leading to higher punching shear capacities.

2.2.3 ACI 318-2008 [12]

The critical section for shear in slabs subjected to bending in two directions follows the perimeter at the edge of the loaded area. The shear stress acting on this section at factored loads is a function of $\sqrt{f_c'}$ (f_c' is the specified compressive strength of concrete in psi) and the ratio of the side dimension of the column to the effective slab depth. A much simpler design equation results by assuming a pseudo critical section located at a distance $d/2$ from the periphery of the concentrated load.

When this is done, the shear strength is almost independent of the ratio of column size to slab depth. For rectangular columns, this critical section was defined by straight lines drawn parallel to and at a distance $d/2$ from the edges of the loaded area.

The nominal shear strength V_c shall be taken as the smallest of (ACI 318-08 §11.11.2.1, in US customary units):

$$V_c = \left(2 + \frac{4}{\beta}\right)\lambda\sqrt{f_c'}b_0 d \tag{2.7}$$

$$V_c = \left(\frac{\alpha_s d}{b_0} + 2\right)\lambda\sqrt{f_c'}b_0 d \tag{2.8}$$

$$V_c = 4\lambda\sqrt{f_c'}b_0 d \tag{2.9}$$

Where:

f_c' is the specified concrete cylinder strength, in psi.

β is the ratio of the long side to the short side of the column, concentrated load of reaction area.

λ is the factor to account for concrete density, to be taken as 1 for normal density concrete.

b_0 is the perimeter of the critical section for shear.

α_s in interior columns is equal to 40, edge columns is equal to 30 and corner columns is equal to 20.

d the distance from the extreme compression fiber to the centroid of tensile reinforcement.

2.2.4 Comparison of code provisions

Gardner (2005) [13] compared experimental data with the provisions of ACI 318-05 [12], Figure 2.10 and Figure 2.11, and EN 1992-1-1:2003 10], Figure 2.12.

According to Gardner, comparison of the code provisions with experimental results is not straightforward because the code expressions were developed to be conservative and use specified or characteristic concrete strengths, reported for experimental studies.

The code punching shear predictions were calculated using the reported mean concrete cylinder strengths. A second note to the data is that the median thickness of the tested slabs was 140 mm (5.51 inches), with a maximum of 320 mm (12.6 inches), which is smaller than slabs used in practice.

The data show that only ACI 318-05 with a rounded shear perimeter meets the criterion of a 5% fractile value greater than one. The results obtained by using EN 1992-1-1:2003 seemed to be unconservative, but the coefficient of variation was smaller than for the results obtained by using ACI 318-05.

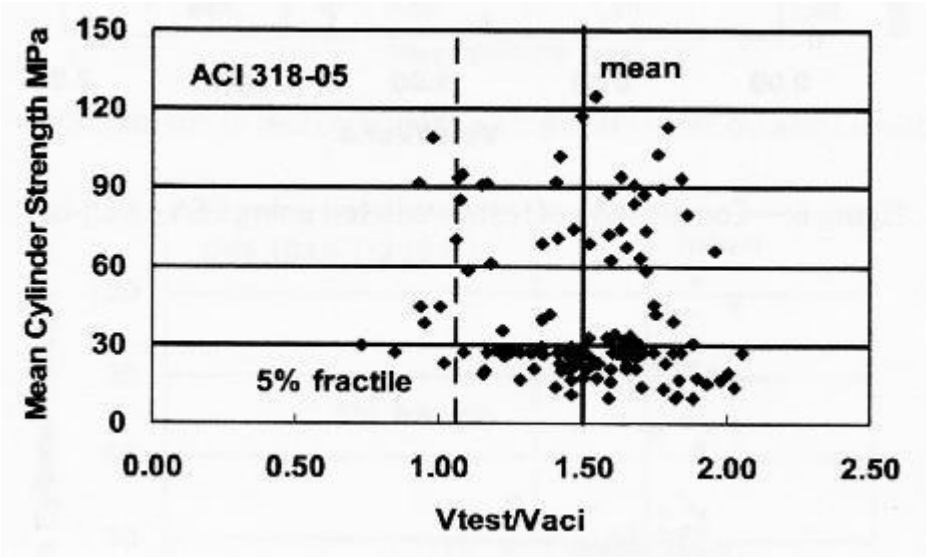

Figure 2.10: Comparison of test/predicted using ACI 318-05 with rounded corners shear perimeter, by Gardner (2005).

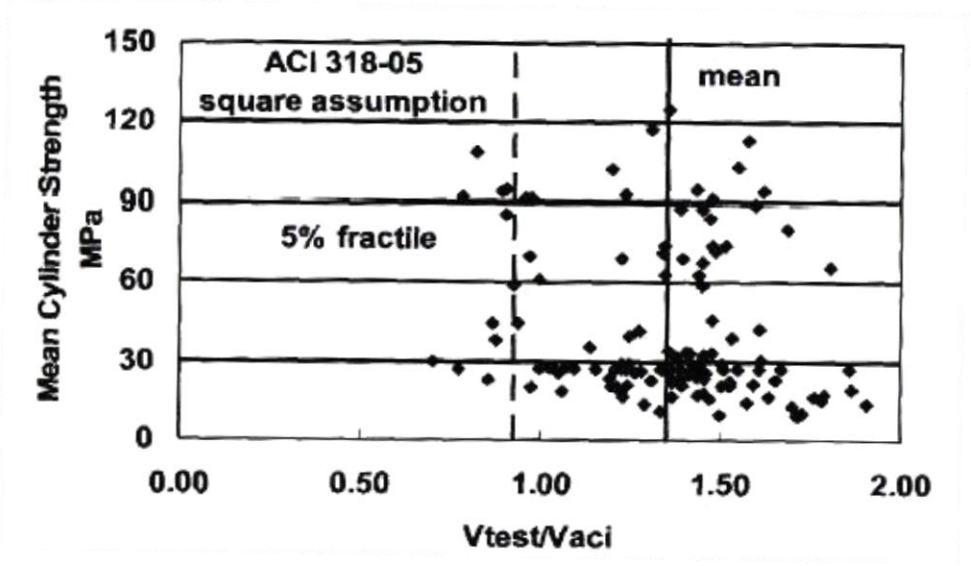

Figure 2.11: Comparison of test/predicted using ACI 318-05 with assumption of square shear perimeter, by Gardner (2005).

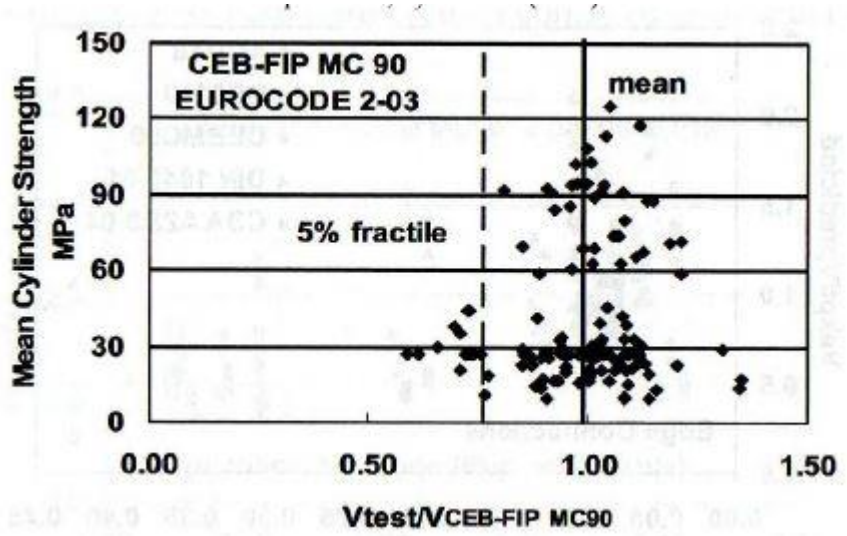

Figure 2.12: Comparison of test/predicted using CEB-FIP MC90 and EN 1992-1-1:2003, by Gardner (2005).

Chapter 3

Description of a new punching shear mechanical model for RC slabs

Even though shear punching of slabs has been experimentally and theoretically studied from long time, there is not yet a consensus about the resisting mechanisms and the modes of failure that take place.

This is evidenced by the differences in the treatment of the shear punching strength in the most important codes provisions, such as EC2 [10] and ACI [12], these differences concern some essential design parameters such as the position of the critical perimeter or the minimum and maximum distances to the column faces where the punching reinforcement should be placed.

It can be said, that many of the punching codes provisions are based on empirical models, adjusted to tests results, but without a consistent theory behind.

Furthermore, for the case of slabs with transverse reinforcement, the code provisions provide results very disperse and even unsafe when compared with experimental results, as evidenced in chapter 2.

Most existing punching tests are not representative of real structures, since they only represent a part of the slab near the column (usually internal column, and much less side or corner columns), and they do not take into account structural effects such as redistribution of moments due to cracking or membrane effects.

Certainly, advanced numerical models are capable to simulate the local and global observed behaviour. However, there is still a lack of objectivity in the selection of the parameters such

as constitutive equations, cracking, size effect, mesh configuration, bond between concrete and reinforcement, etc. which drives to a large variability in the results. Numerical methods are also too time consuming for being used in daily design.

Since punching is a brittle and undesirable failure, in order to reach the required safety level without an unaffordable cost, simplified but safe and accurate design models are needed. Such models should be capable to capture the most important phenomena that take place and should be verified with available experimental results. As described in chapter 2, Kinnunen and Nylander (1960) [4] were the first ones to set the theoretical bases for a sound analysis of the problem; Broms (1990) [6] then focused his research on the multiaxial stress state of the problem, faced the size effect and formulated a model for eccentrically loaded columns; finally Muttoni (2008) [9] applied the critical shear crack theory to punching.

However, some important aspects are still in discussion, for example:

1) A clear criterion to define the position of the critical perimeter;
2) The efficiency of the shear reinforcement used, which depends on its position and on its anchorage capacity;
3) The influence of the presence of punching reinforcement on the concrete contribution (due to the change in the crack inclination);
4) The influence of the moment transferred from the slab to the column on the punching strength.

In this chapter, a new mechanical model for the estimation of the punching shear strength of reinforced concrete slabs is presented. The model is an adaption of a previously existing model (compression chord capacity model) for shear strength, developed by the authors A. Cladera, A. Marí, J. Bairán, C. Ribas, E. Oller, N. Duarte [8], which incorporates the contribution of the main shear resisting mechanisms. For this purpose, the differences between the shear and punching resistant mechanisms are identified and accounted for into the equilibrium and compatibility equations and into the failure criterion. The model is validated by comparing their results with those available punching tests on slabs with and without punching reinforcement. The results of the model have been compared with those of two large punching databases, without and with shear reinforcement [14] and general good agreement has been obtained. Finally, conclusions are drawn about the practical applicability of the model and the possibilities of its extension. First of all, it is necessary a brief description of the previously existing model for shear and then will be described the adaptation for the punching phenomena.

3.1 The compression chord capacity model

This model incorporates in a compact formulation, the contributions of the concrete compression chord, the cracked web, the dowel action and the shear reinforcement.

The mechanical character of the model provides valuable information about the physics of the problem and incorporates the most relevant parameters governing the shear strength of structural concrete members.

3.1.1 Theoretical background

The model consider that the shear strength, V_u (eq. 3.1) is the sum of the shear resisted by concrete and by the transverse reinforcement V_s, furthermore it must be lower than the shear force that produce failure in the concrete struts, $V_{u,\max}$.

The concrete contribution is explicitly separated into the shear resisted in the uncracked compression chord V_c, shear transferred across web cracks V_w and the dowel action in the longitudinal reinforcement V_l. The importance of the different contributing actions is considered to be variable as cracks open and propagate.

$$V_u = \left(V_c + V_w + V_l\right) + V_s = f_{ctm} \cdot b \cdot d \cdot \left(v_c + v_w + v_l\right) + v_s \cdot f_{ctm} \cdot b \cdot d \tag{3.1}$$

variables v_c , v_w , v_l , and v_s are the dimensionless values of the shear transfer actions considered in the multi-action model or background mechanical model, (Eq. 3.2, 3.3, 3.4*a*,*b*, 3.5).

$$v_c = \xi \left\{ \left(\left(0.88 + 0.2 + 0.5 \frac{b}{b_w} \right) v_s \right) \frac{x}{d} + 0.02 \right\} \frac{b_{v,eff}}{b} K_p \tag{3.2}$$

$$v_w = 167 \frac{f_{ctm}}{E_{cm}} \frac{b_w}{b} \left(1 + \frac{2 G_f E_{cm}}{f_{ctm}^2 d_0} \right) \tag{3.3}$$

$$v_l = 0.23 \frac{\alpha_e \rho_l}{(1-x)/d} \quad \text{if } v_s > 0 \qquad v_l = 0 \quad \text{if } v_s = 0 \tag{3.4 a,b}$$

$$v_s = \left(d_s - x\right) \cot \vartheta \frac{A_{sw} \cdot f_{yw}}{s \cdot f_{ctm} \cdot b \cdot d} \approx \frac{0.85 d_s A_{sw} f_{yw}}{s \cdot f_{ctm} \cdot b \cdot d} \tag{3.5}$$

Where:

$\xi = 1.2 - 0.2a \geq 0.65$ considers the size effect in the compression chord, (a in meters);

$\frac{x}{d} = \frac{x_0}{d} + \left(\frac{h - x_0}{d}\right)\left(\frac{d}{h}\right)\frac{\sigma_{cp}}{\sigma_{cp} + f_{ctm}}$ is the neutral axis depth ratio with $\frac{x_0}{d} = \alpha_e \rho_l \left(-1 + \sqrt{1 + \frac{2}{\alpha_e \rho_l}}\right)$;

$b_{v,eff} = b_w + 2h_f \leq b$ if $x < h_f$

$b_{v,eff} = b_v \eta + b_w (1 - \eta)$ if $x > h_f$, $\eta = 3\left(\frac{h_f}{x}\right)^2 - 2\left(\frac{h_f}{x}\right)^3$;

$K_p = 1 + 0.3\frac{P \cos\alpha \left(x + d_s - d_p\right)}{f_{ctm} b d^2}$ is the strength factor related to M_{cr};

$\cot\vartheta = \frac{0.85 d_s}{d_s - x} \leq 2.5$ is the critical crack inclination;

For the maximum shear strength due to the strut crushing, (Eq. 3.6), this model adopts the formulation of the current EC2, derived from plasticity models, but assuming that the angle of the compression strut is equal to the angle of the critical crack given in (Eq. 3.5).

$$V_{u,\max} = \alpha_{cw} b_w z \nu_1 f_{cm} \frac{\cot\vartheta}{1 + \cot^2\vartheta} \tag{3.6}$$

Strut crushing is not a common failure mode, but it is possible in cases when larger contribution of V_s exists, so the verification is introduced.

As larger values of V_s implies large amount of stirrups, usually this will occur with smear cracking in the web. Therefore, Eq. 3.6 represents a check that another failure mode, strut crushing, prevents the occurrence of the compression chord failure.

Note that these expressions do not include partial safety factors and that depend on mean values of the mechanical properties.

A main assumption of the model is to consider that failure occurs when, at any point of the compression chord, the principal stresses (σ_1, σ_2) reach the Kupfer's biaxial failure envelope, in the compression-tension branch (Figure 3.1).

This assumption is based on the experimental observation that when this happens, the concrete in the compression chord, subjected to a multi-axial stress state, initiates softening, reducing its capacity as the crack propagates.

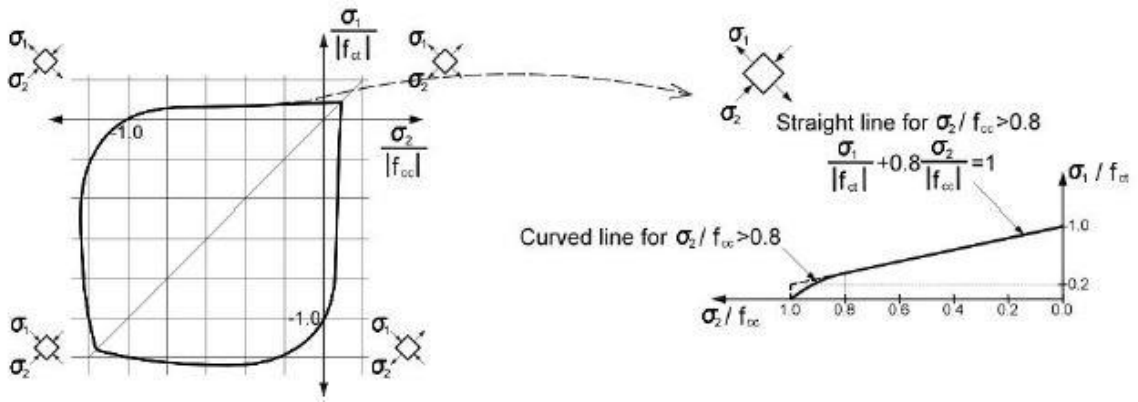

Figure 3.1: Adopted failure envelope for concrete under a biaxial stress state.

When the load is increasingly applied, flexural cracks appear as the bending moment increases. It is assumed that the critical crack is the closest crack to the zero-bending moment point and that it starts where the bending moment diagram at failure reaches the cracking moment of the cross section. The critical section, where failure occurs, is assumed to be located where the critical crack reaches the neutral axis depth. This assumption is justified because any other section closer to the zero-bending moment point has a bigger depth of the compression chord, produced by the inclination of the strut and will resist a higher shear force.

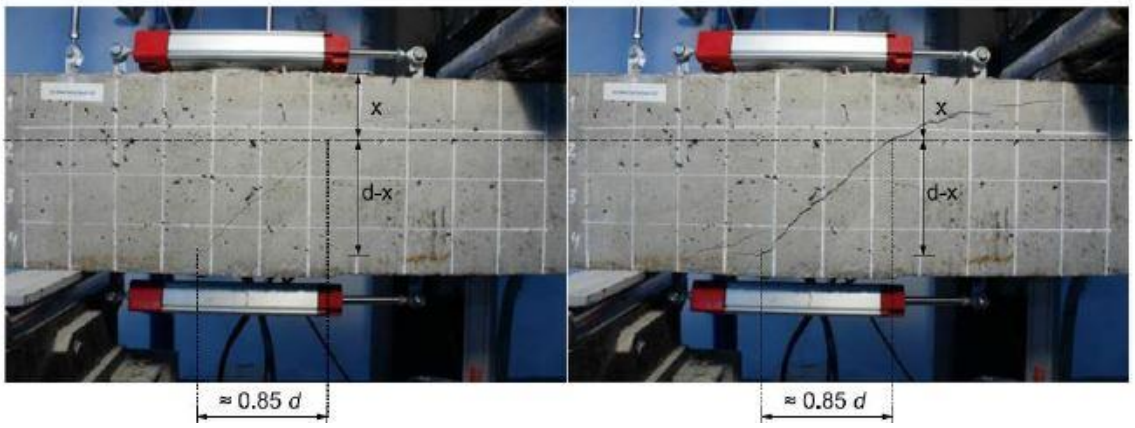

Figure 3.2: Critical shear crack evolution and horizontal projection of the first branch of this crack.

On the other hand, any other section placed between this section and the maximum moment section will have the same depth of the compression chord but will be subjected to higher normal stresses and, therefore, the uncracked concrete zone will have a higher shear transfer capacity.

It is possible to consider the horizontal projection of the first branch of the flexural-shear critical crack to be equal to $0.85d$, this is equivalent to considering that its inclination is approximated as in (Eq. 3.5).

As a result of the above assumptions, the distance between the zero bending moment point and the initiation of the critical crack is $s_{cr} = M_{cr} / V_u$, and the position of the critical section will be $s_u = s_{cr} + 0.85d_s$, which is usually a little higher than d_s.

This is the reason why for design purposes, d_s is adopted as the position of the section where shear strength must be checked for reinforced concrete members.

In prestressed members, the cracking moment is higher and the position of the critical crack is shifted away from the zero-bending moment point with respect to members with ordinary reinforcements. For this reason, it is proposed that the shear strength is checked at a section placed at a distance $d_s\left(1+0.4\sigma_{cp} / f_{ctm}\right)$.

The higher cracking moment in a prestressed concrete section, with respect to a reinforced concrete section, is considered in the background mechanical model by means of the strength factor K_p (Eq. 3.2).

Figure 3 plots, in a schematic way, the different contributing actions in the proposed model (Figure 3a, 3b) and compares them with the contributing actions in the Level III of Approximation of Model Code 2010 (Figure 3c), and the steel contribution of a variable angle truss model (Figure 3d), as the one given in EC2 for members with shear reinforcement.

The different models are not contradictory; in fact, the fundamental difference is that they have been derived from different simplifying assumptions. The model developed by the authors considers that the maximum load occurs slightly after the first branch of the critical crack reaches the neutral axis depth, as also proposed by [15]. Other models take into account the full crack development.

When the second branch of the critical crack is developed, the aggregate interlock in the first branch is activated. It could be understood that the shear transferred by the non-cracked concrete zone in this model (Figure 3a, 3b) is approximately equal to the contributing actions in the other models that takes place after the development of the second branch of the critical crack (aggregate interlock or stirrups crossing that zone).

Note that the angle ϑ (Figure 3a, 3c) is the angle of the critical crack, and it is an angle fixed by the assumptions carried out in the models.

However, the angle ϑ in Figure 3d is the angle of the compression field, an equilibrium angle that can be chosen by the designer.

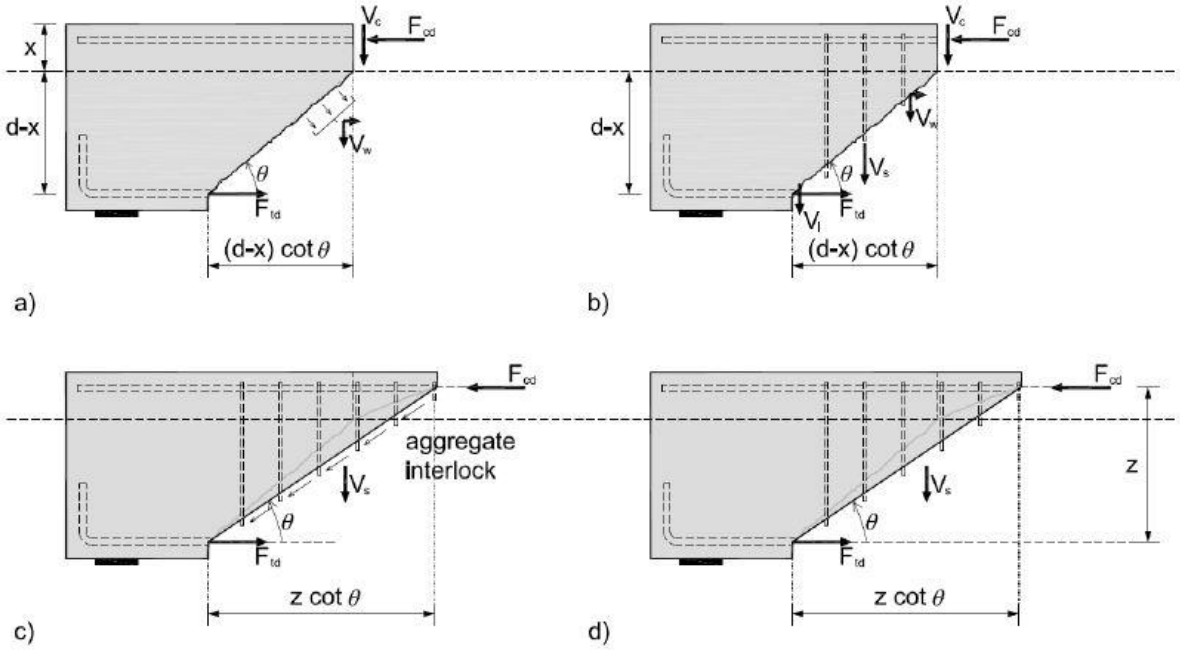

Figure 3.3: Shear contributing actions at failure. a) Background mechanical model for elements without stirrups. b) Background mechanical model for elements with stirrups. c)Model Code 2010 model. d)Variable angle truss model.

3.1.2 General and minor changes to simplify the procedure

The theoretical background of the new mechanical model has been presented in the previous section. However, for design purposes, some simplifications are necessary in order to make the model easier to use in daily engineering practice.

Considering that when shear-flexure failure takes place, both the residual tensile stresses, v_w (Eq. 3.3), and the dowel action, v_l (Eq. 3.4), are small compared to the shear resisted by the uncracked zone, v_c (Eq. 3.2), the two first mentioned contributing actions, v_w and v_l have been incorporated into v_c (Eq. 3.2).

The resulting equation is presented in Eq. 3.7:

$$V_u = \left(v_c + v_w + v_l\right) f_{ctm} \cdot b \cdot d + V_s = 0.3 \cdot \xi \cdot \frac{x}{d} \cdot f_{ck}^{(2/3)} \cdot b_{v,eff} \cdot d + V_s \left(1 + \Delta_{Vcu}\right) \tag{3.7}$$

All the parameters of Eq. 3.7 have been defined previously and Δ_{Vcu} is a non-dimensional confinement factor which considers the increment of the shear resisted by the concrete caused by the stirrup confinement in the compression chord (Eq. 3.8).

This parameter will be taken constant and equal to 0.4 for simplicity reason in the type-code expression, although its actual value is generally between 0.2 and 0.6 for normal members.

$$\Delta_{Vcu} = 0.5\xi\left(1 + \frac{b}{b_w}\right)\frac{x}{d}\frac{b_{v,eff}}{b} \approx 0.4 \tag{3.8}$$

Note that the influence of normal forces in Eq. 3.7 is considered by the parameter *x/d*. The strength factor K_p, which consider the higher cracking moment in a prestressed concrete section with respect to a reinforced concrete section, has been considered equal to 1.0 due to its relatively low influence and for simplicity reasons.

Eq. 3.7 depends on the neutral axis depth ratio, *x/d*. This value may be computed using the value taken from Eq. 3.2 disregarding the compression reinforcement, but it may be also simplified as proposed in Eq. 3.9.

$$\frac{x_0}{d} = \alpha_e \rho_l \left(-1 + \sqrt{1 + \frac{2}{\alpha_e \rho_l}}\right) \approx 0.75\left(\alpha_e \rho_l\right)^{1/3} \tag{3.9}$$

Consequently, the model considers the influence of the amount of the longitudinal tensile reinforcement in an indirect way, through the variation of the neutral axis depth. An increase of the amount of the longitudinal reinforcement would increase the neutral axis depth, increasing the shear strength and decreasing the inclination of the critical crack.

The longitudinal compression reinforcement is disregarded in Eq. 3.9 because its effect decreasing the neutral axis depth but is compensated by the increase of the shear strength caused by the presence of steel in the concrete compression chord.

Eq. 3.7 has been derived taken into account that, in most beams, the residual tensile stresses v_w, and the dowel action v_l, are small compared to the shear resisted by the uncracked zone v_c. However, in some members, (e.g. one-way slabs) with low levels of longitudinal reinforcement and without stirrups, this assumption would lead to too conservative results, as the dimensionless shear contribution due to residual stresses along the crack may be comparable to the contribution of the uncracked zone, since *x/d* is small.

In this situation, it is possible to derive an equation for the minimum shear strength $V_{cu,\min}$ that takes explicitly into account the residual tensile stresses action. This expression will be very useful for elements with low amounts of longitudinal reinforcement.

The resulting equation for this minimum shear strength is given by Eq. 3.10, in which *x/d* shall not be taken higher than 0.20.

$$V_{cu,\min} = \left(v_c + v_w\right) f_{ctm} \cdot b \cdot d \approx 0.25\left(\xi \frac{x}{d} + \frac{20}{d_0}\right) f_{ck}^{(2/3)} \cdot b_w \cdot d \tag{3.10}$$

The influence of the compression flange is considered in the general model by means of the effective shear width given by the values in Eqs. 3.2. In the case in which $x > h_f$, the effective width shall be interpolated between the web width b_w, and the effective width in the compression flange b_v.

The value of $b_{v,eff}$,due to its complexity in Eq. 3.2, can be calculated with the simplified expression (Eq. 3.11):

$$b_{v,eff} = b_v = b_w + 2h_f \le b \qquad \text{if } x < h_f \tag{3.11 a}$$

$$b_{v,eff} \approx b_w + \left(b_v + b_w\right)\left(\frac{h_f}{x}\right)^{3/2} \qquad \text{if } x > h_f \tag{3.11 b}$$

These values are compared with the ones of Eq. 3.2 in Figure 3.4 for some T-beams with compression flanges.

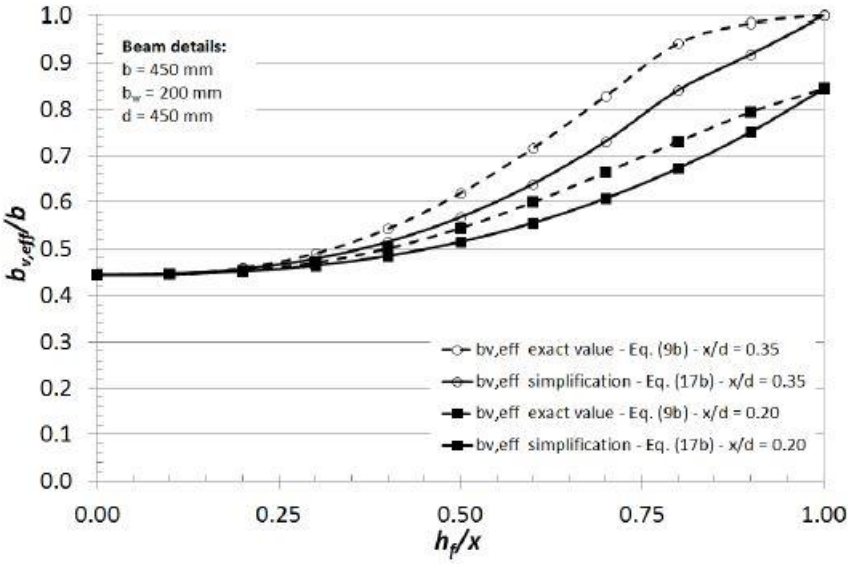

Figure 3.4: Comparison between exact and simplified relative effective width for shear strength calculations.

The results shown that the error between the original formulation and the simplification is generally lower than 10%.

3.1.3 Size effect

Due to the brittle character of the failure that takes place when the second branch of the critical crack propagates, it is necessary to take into account the size effect.

The empirical factor proposed by other authors [16] was adopted in the background mechanical model, by means of the term ξ which can be assimilated to the size effect of a splitting test. According to such model, the size effect on the shear failure of slender beams seems to depend on the size of the shear span a, that would be proportional to the diameter of the specimen of a hypothetical splitting test that occurs at the beam compression chord, between the point where the load is applied and the tip of the first branch of the critical shear crack. The value of ξ given by Eq. 3.2 was derived from a previous experimental work carried out by Hasegawa et al. [17], in which a linear relationship was proposed for the size effect.

However, this work was lately re-examined by Bažant et al. [18], suggesting that the splitting tensile strength followed the size effect term developed by fracture mechanics with an asymptote, as shown in Eq. 3.12:

$$\sigma_N = \max\left(\frac{B \cdot f_t'}{\sqrt{1+\beta_0}}, \sigma_y\right) \tag{3.12}$$

Where f_t' is a measure of material tensile strength, β_0 is proportional to the diameter of the cylinder, B is an empirical constant and σ_y is the asymptote. Moreover, the shear strength of structural concrete members is affected, not only by the element size, but also by its slenderness *a/d*. For the previous reasons, a new empirical size effect term is proposed which depends on *d* and *a/d*. The factor depending on *d* will be taken as the factor proposed by ACI Committee 446 [19], Eq. 3.13, which is an expression similar to the one on the left inside the parenthesis in Eq. 3.12.

$$v_c = \frac{v_0}{\sqrt{1+\frac{d}{k_d}}} \tag{3.13}$$

The new combined size and slenderness effect factor is given in Eq. 3.14:

$$\xi = \frac{2}{\sqrt{1+\frac{d_0}{200}}}\left(\frac{d}{a}\right)^{0.2} < 0.45 \tag{3.14}$$

Figure 3.5 compares Eq. 3.14 with previous size effect factor ξ given by Eq. 3.2.

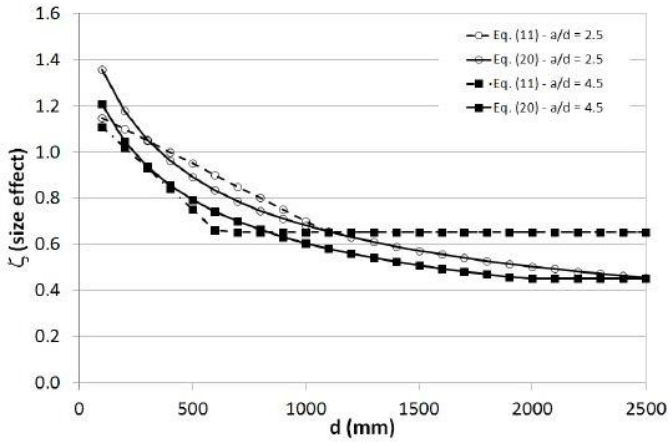

Figure 3.5: Comparison between size effect term given by Eq. 3.14 and new size effect term given by Eq. 3.2.

3.1.4 Simplified shear design

The design procedure of members with or without shear reinforcement shall verify equilibrium and shall consider the influence of the stresses transferred across cracked concrete V_w, by the compression chord V_c, and the contribution of the shear reinforcements V_s and longitudinal reinforcements V_l, (Figure 3.6).

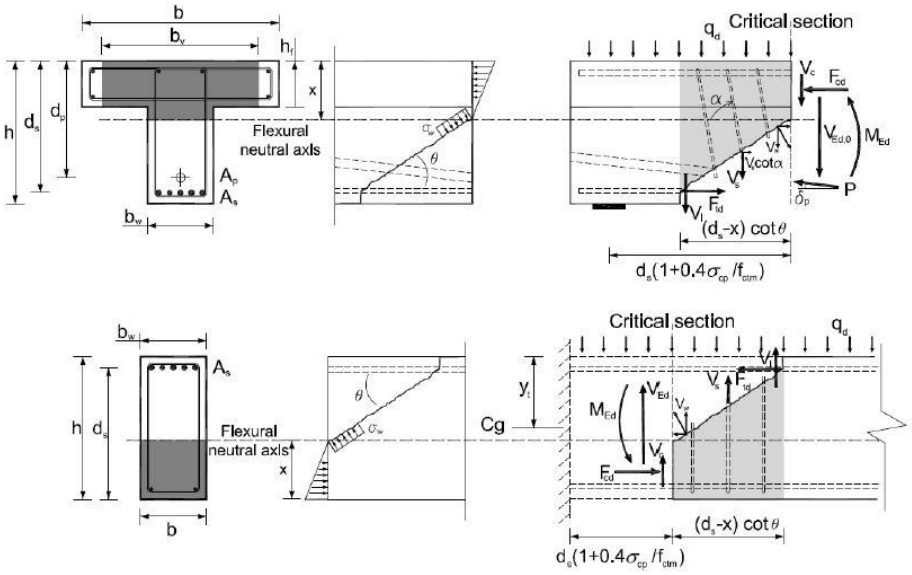

Figure 3.6: Shear contributions and notation for simple supported beam and cantilever beam.

Shear strength shall be checked at least at a distance $d_s\left(1+0.4\sigma_{cp}/f_{ctm}\right)$ from the support axis and at any other potential critical section, where $\sigma_{cp}=N_{Ed}/A_c$ is the mean concrete normal stress due to axial loads or prestressing (compression positive) and f_{ctm} is the mean concrete tensile strength, not greater than 4.60 MPa.

The inclination of the compression strut is considered equal to the mean inclination of the shear crack, computed as follows:

$$\cot\vartheta=\frac{0.85d_s}{d_s-x}\le 2.5 \tag{3.15}$$

where x is the neutral axis depth of the cracked section, obtained assuming zero concrete tensile strength. For reinforced concrete members without axial loads, $x=x_0$ (see Eq. 3.9).

The shear strength, is the smaller value given by Eqs. 3.16 and 3.17

$$V_{Rd} = V_{cu} + V_{su} \tag{3.16}$$

$$V_{Rd,\max} = \alpha_{cw} b_w z \, \nu_1 f_{cd} \frac{\cot\vartheta + \cot\alpha}{1 + \cot^2\vartheta} \tag{3.17}$$

Where V_{cu} is the shear resisted by the concrete considering the different contributions given in (Eq. 3.18), $V_{cu} = V_c + V_l + V_w$

$$V_{cu} = 0.3\xi \frac{x}{d} f_{cd}^{2/3} b_{v,eff} d \;<\; V_{cu,\min} = 0.25\left(\xi K_c + \frac{20}{d_0}\right) f_{cd}^{2/3} b_w d \tag{3.18}$$

And V_{su} the shear resisted due to the shear reinforcement:

$$V_{su} = 1.4 \frac{A_{sw}}{s} f_{ywd} \left(d_s - x\right) sen\alpha \left(\cot\vartheta + \cot\alpha\right) \tag{3.19}$$

ξ is a combined size and slenderness effect factor, given by Eq. 3.14.

The parameter $b_{v,eff}$ shall be calculated using Eqs. 3.11.

For the determination of f_{cd} in Eq. 3.18, f_{ck} shall not be taken greater than 60 MPa. K_c is equal to the relative neutral axis depth, *x/d*, but not greater than 0.20 when computing $V_{cu,\min}$.

The constant 1.4 is not a calibration factor, but a term to take into account the confinement of the concrete in the compression chord caused by the stirrups, as shown in Eq.3.8. The rest of terms can be seen in the notations. Shear reinforcement is necessary when the shear design force exceeds the shear resisted by the concrete without shear reinforcement given by Eq. 3.18.

Then, the necessary shear reinforcement is:

$$\frac{A_{sw}}{s} = \frac{V_{Ed} - V_{cu}}{1.4 \cdot f_{ywd} \left(d_s - x\right) sen\alpha \left(\cot\vartheta + \cot\alpha\right)} \tag{3.20}$$

The additional tensile force ΔF_{td} in the longitudinal reinforcement due to the shear force V_{Ed} may be calculated from:

$$\Delta F_{td} = V_{Ed} \cot\vartheta - 0.5 V_{su} \left(\cot\vartheta + \cot\alpha\right) \tag{3.21}$$

The tensile force of the longitudinal reinforcement, $\left(M_{Ed}/z\right)+\Delta F_{td}$ should be taken not greater than $\left(M_{Ed,\max}/z\right)+\Delta F_{td}$, where $M_{Ed,\max}$ is the maximum moment along the beam.

In elements with inclined prestressing tendons, longitudinal reinforcement at the tensile chord should be provided to carry the longitudinal tensile force due to shear defined by Eq. 3.21.

3.2 Adaptation of the compression chord capacity model to punching shear

The model presented before was created to predict shear resistance for reinforced concrete slabs and beams. In order to adapt this mechanical model for the estimation of the punching shear strength it is necessary an adaption of the existing model for shear strength.

For this purpose, the differences between the shear and punching resistant mechanisms are identified and accounted for into the equilibrium and compatibility equations and into the failure criterion. The model is validated by comparing their results with those available punching tests on slabs with and without punching reinforcement.

3.2.1 Relevant differences between shear and punching failures which must be accounted for.

Even though punching may be considered as a slab shear failure around a column, the following differential aspects must be taken into account when formulating the punching strength of a slab:

- **Position of the critical crack and of the critical section**

In a two-way slab supported by isolated columns, the bending moment law does not follow the same pattern than in a beam (see Figure 2), the section where the cracking moment is reached is placed at a distance of the column face, generally s_{crack} less than 2*d*.

Therefore, the critical crack develops in a “D” region, following an almost straight path from its initiation to the intersection of the compressed face of the slab with the support perimeter.

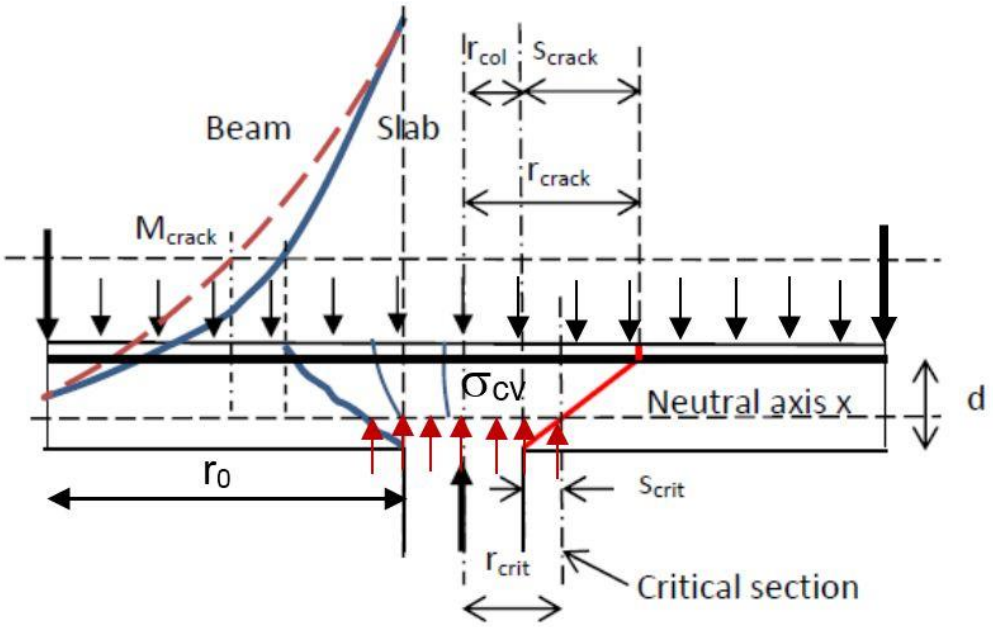

Figure 3.7: Position of critical crack and critical perimeter geometry.

Then, the critical section will be that where the critical crack reaches the neutral axis, placed at a distance to the column face given by Eq. 3.22:

$$s_{crit} = x \cot \vartheta = s_{crack} \frac{x}{d} \tag{3.22}$$

Equaling the radial bending moment per unit width $m_r(r)$ to the cracking moment per unit width, the value of s_{crack} can be obtained.

According to the elastic theory of plates, for a uniformly distributed load, $m_r(r)$ is given by Eq. 3.23:

$$m_r(r) = \frac{V_{Ed}}{4\pi}(1+\nu)\ln\frac{r_0}{r} = m_{crack} \rightarrow r_{crack} \simeq r_0 e^{-10.5\frac{m_{crack}}{V_{Ed}}} \rightarrow s_{crack} = r_{crack} - r_{col} \tag{3.23}$$

Where V_{Ed} is the total shear transferred by the slab to the column, ν is the Poisson coefficient, r_0 and r are the distances to the column axis from the zero bending moment point and from the point where the moment is calculated, respectively, and r_{col} is the radius of a column with equal perimeter than the actual column.

Combining Eq. 3.22 and Eq. 3.23, the distance from the critical perimeter to the column face and the inclination of the critical crack are given by Eq. 3.24:

$$\frac{s_{crit}}{d} = \frac{s_{crack}}{d}\frac{x}{d} = \frac{r_{col}}{d}\left(\frac{r_0}{r_{col}}e^{-10.5\frac{m_{crack}}{V_{Ed}}} - 1\right)\frac{x}{d} \tag{3.24}$$

$$\cot\vartheta = \frac{s_{crack}}{d} \leq 2.5 \tag{3.25}$$

Eq. 3.24 shows that the position of the critical perimeter, it depends on r_{col}/d, on r_0/r_{col} (and, therefore from span length and from the bending moments law) on $m_{crack}/\mathrm{V}_{Ed}$ (thus from the column depth, the concrete tensile strength and the shear force transferred to the column) and from *x/d*.

Since for design purposes it is desirable a simpler way to define the critical perimeter, two studies have been done to estimate the value of s_{crit}/d:

1) A study of the cases included in the database of experimental tests [20].

2) A parametric study on 648 cases of typical slabs and columns including two slab concrete strengths, three span lengths, four slab slenderness L/d, three total load levels, three bending moments distributions, and three values of the column relative axial ratio $\nu = N_d/(f_{cd}A_c)$.

The results of s_{crit}/d obtained in the tests were slightly higher than in the simulation, since the reinforced amount in the tests was forced to avoid flexural failure. The average value was 0.55 so $s_{crit} = 0.5d$ will be conservatively adopted in this work. So, if we suppose the critical distance $0.5d$ from the support, the length became λd (Eq. 3.26).

$$\frac{0.5d}{x} = \frac{\lambda d}{d-x} \rightarrow \lambda = 0.5\left(\frac{d-x}{x}\right) \tag{3.26}$$

- **Effect of the radial geometry**

Eq. 3.18 has been derived for beams with constant width *b*, however, in a slab supported on isolated columns, the critical perimeter is smaller than the cracking perimeter (Figure 3.8).

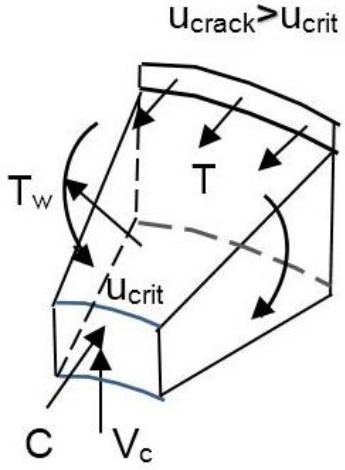

Figure 3.8: Effect of radial geometry.

Since Eq. 3.18 is referred to the critical perimeter, the cracking moment at the cracking section should be substituted by $\mu = \mu_{crack} \cdot (r_{crack} / r_{crit}) = 0.2(r_{crack} / r_{crit})$, where 0.2 is the dimensionless cracking moment of a rectangular section.

Thus, according to the compression chord capacity model for shear resistance when the moment at the cracking section is $\mu > \mu_{crack}$ the value of V_c should be multiplied by factor $K_b = 0.94 + 0.3\mu$, which in this case is shown in Eq. 3.27:

$$K_b = 0.94 + 0.06\frac{r_{crack}}{r_{crit}} \simeq 0.94 + 0.06\frac{\frac{r_{col}}{d} + 0.5\frac{d}{x}}{\frac{r_{col}}{d} + 0.5} \simeq 0.94 + 0.06\frac{\frac{r_{col}}{d} + 1.65}{\frac{r_{col}}{d} + 0.5} \tag{3.27}$$

Where r_{col} is the radius of a column with the same perimeter than the actual column.

For design purposes, a conservative value of $d / x = 3$ can be adopted, thus resulting an average value of $K_b = 1.1$.

In addition, there are circumferential moments which compress the bottom part of the slab, which is subjected to a triaxial stress state. These moments produce transverse compressions in the bottom of the slab, of similar value to the radial compressions, generating a triaxial compression state, which enhances the shear strength of the uncracked concrete zone, in approximately 15-20%.

In this work an increment of 18% is adopted, according to the studies made.

- **Local effect of the support on the stress state at the critical point.**

In the case of punching, the critical section is placed at a distance of around $0.5d$ of the column face, so the critical point is close enough to column's face to be affected by the vertical stresses σ_{cv}, introduced by the column.

Figure 3.7 shows a scheme of the vertical stresses σ_{cv} in the vicinity of the column where, for simplicity, a constant average value has been assumed, obtained by dividing V_{Ed} (total shear transferred from the slab to the column) by A_{crit} (slab area surrounded by the critical perimeter).

The adequacy of such assumption was verified by means of a nonlinear analysis.

In this model, the shear resisted by the compressed concrete chord is that existing when the critical crack propagates inside the compressed zone. This is assumed to take place when the principal stresses (σ_1, σ_2) at the weakest point of the compression chord in the critical section reach the Kupfer biaxial stresses failure envelope, see Figure 3.1.

Once the normal and principal stresses that produce failure are known, the shear stress at the critical point can be obtained. Assuming a parabolic distribution of shear stresses with zero values at both ends of the parabola, the shear force V_c is obtained through direct integration (Eq. 3.28).

$$V_c = \zeta \int_0^c \tau(y) \cdot b \cdot dy = 0{,}682\ \sigma_1\, b\, x \sqrt{1 - \frac{\sigma_x + \sigma_y}{\sigma_1} + \frac{\sigma_x \cdot \sigma_y}{\sigma_1^{\,2}}} \tag{3.28}$$

Where σ_1 is the principal tensile stress at failure, expressed as $\sigma_1 = R_t f_{ct}$, where $R_t = 1 - 0.8(\sigma_2 / f_{cc})$.

In order to estimate the influence of such vertical stresses, Eq. 3.28 has been solved for different longitudinal reinforcement ratios $\eta\rho$, concrete strengths and vertical stresses, σ_{cv}.

It has been found that V_c increases affect almost linearly with σ_{cv} / f_{ct} according to a factor K_σ defined in Eq. 3.29:

$$K_\sigma = \left(1 + 0.56 \frac{\sigma_{cv}}{f_{ctm}}\right) \quad ; \quad \sigma_{cv} = \frac{V_{Ed}}{A_{crit}} \tag{3.29}$$

Where A_{crit} is the surface of slab surrounded by the critical perimeter.

3.2.2 Proposed equations for punching shear strength of slabs without shear reinforcement

Taking into account the above considerations, Eq. 3.18 can be adapted to punching as follows:

$$V_c = k_b V_{c0} = 1.18 k_b \cdot \zeta \frac{x}{d} \cdot \left(0.3 f_{cd}^{2/3} + 0.56\sigma_{cv}\right) \cdot u_{crit} d \;\geq\; V_{cu,\min} \tag{3.30}$$

$$V_{cu,\min} = 0.25 f_{cd}^{2/3} \left(0.36\zeta + \frac{20}{d_0}\right) \cdot u_{crit} d \tag{3.31}$$

which is almost equal to Eq. 3.18, but substituting the width b by the critical perimeter u_{crit}, and including the effect of the radial geometry and the effect of the column confining stresses σ_{cv}.

For building slab floors subjected to distributed loads, the shear span, *a,* to be used in the size effect parameter ξ, defined in Eq. 3.14, can be estimated as the average distance from the position of the line of zero radial bending moment to the edge of the column, $l_0 = \sqrt{l_{0y} \cdot l_{0z}}$, where $l_{0y} \simeq 0.2 l_y$ and $l_{0z} \simeq 0.2 l_z$, and l_z are the span lengths in the y and z directions.

The neutral axis depth x/d should be obtained using the average of the longitudinal reinforcement ratios ρ_{ly}, ρ_{lz}, in the two orthogonal directions, adopting an effective slab width $b_{s,eff}$ approximately equal to the column side or diameter plus 3 times the slab effective depth at each side of the column. When computing the minimum punching strength $V_{cu,\min}$ (Eq. 3.31), $b_{s,eff}$ is the effective depth of the slab *d*, but not less than 100 mm.

Chapter 4

Modelling of reinforced concrete slabs in Midas FEA

Three slab-column specimens (*SB1*, *R1* and *no.2*) without shear reinforcement were analyzed using a 3D analysis with the commercial FEA program Midas FEA.

The purpose of this project has been to simulate punching failure of reinforced concrete slabs supported at their edges in order to study the structural behaviour during this phenomenon, furthermore has been verified that one of the hypothesis of the compression chord capacity model, the multiaxial state of stresses in the compressed zone, was respected in the results.

The aim of the study has been to provide information that can be of use when appropriate designs of reinforced concrete slabs supported on steel columns are sought.

4.1 Nonlinear FE analysis and numerical methods.

The finite element method is used to numerically solve field problems. In structural engineering this method is employed by dividing the structure into finite elements, each allowed to only one spatial variation. Since element variations are believed to be more complex than limited by a simple spatial variation, the solution becomes approximate.

Each element is connected to its neighbouring element by nodes. At these nodes equilibrium conditions are solved by means of algebraic equations. The assembly of elements in a finite element analysis is referred to as the mesh.

Due to the approximation of the spatial variation within each element the solved quantities over the entire structure are not exact.

However, the overall solution can be improved by assigning a finer mesh to the structure.

4.1.1 Nonlinearity in the analysis

In a nonlinear analysis it is possible to follow nonlinear structural responses throughout the loading history as the load is applied in several distinguished steps.

These load steps, or increments, are considered as a form of nonlinearity, superordinate to the types of nonlinearity that will be described further on.

A mathematical description of the overall structural response is presented by the following equation system:

$$\underline{\underline{A}} \cdot \underline{x} = \underline{b} \tag{4.1}$$

Where:

$\underline{\underline{A}}$ is the structural matrix.

$\underline{x}$ is the vector of displacements.

$\underline{b}$ is the unknown vector containing internal forces.

Within each load step a number of iterations are carried out until equilibrium is found for the equation system.

Nonlinearity can also be employed for constitutive, geometrical and contact relations all of which have been used in the simulations in this work. Nonlinear constitutive relations consider the range of material responses from elastic to plastic behaviour;

It is possible to account for nonlinear material behaviours, such as cracking of concrete and yielding of reinforcement. These in turn cause redistribution of forces within the structure. Geometrical nonlinearity accounts for the ongoing deformations of the structure including the change of force direction.

The analysis accounts for the changing structural matrix due to deformations and uses an updated matrix for the consequent load increment. When fluctuating contact between two adjacent parts of a structure is experienced, contact nonlinearity accounts for the changes of contact forces and presence of frictional forces.

4.1.2 Numerical solution methods

In order to solve nonlinear equation systems iterative solution methods are used. Their scope is to find approximate numerical solutions to the equation systems that correlate the external forces to the structural response.

In Midas FEA iterations are carried out using either one of the four default solution methods, namely *Newton-Raphson, modified Newton-Raphson, Arc Length and Initial Stiffening*.

Within an analysis it may be appropriate or even necessary to switch between solution methods due to regional responses in the load-displacement function.

- **The Newton-Raphson method**

The Newton-Raphson (N-R) iteration is an iterative solution method using the concept of incremental step-by-step analysis to obtain the displacement u_i for a given load P_i.

N-R method keeps the load increment unchanged and iterates displacements and is therefore suitable to use in cases when load values must be met. The N-R iteration can also be used for incremental increase of the deformation *u*.

The search for the unknown deformation is described by the tangent of the load-displacement function. This is known as the tangent stiffness $K_{t,i}$ and describes the equilibrium path for each increment. The N-R iteration scheme is illustrated in Figure 4.1 which describes the search for the unknown deformation when a load is applied.

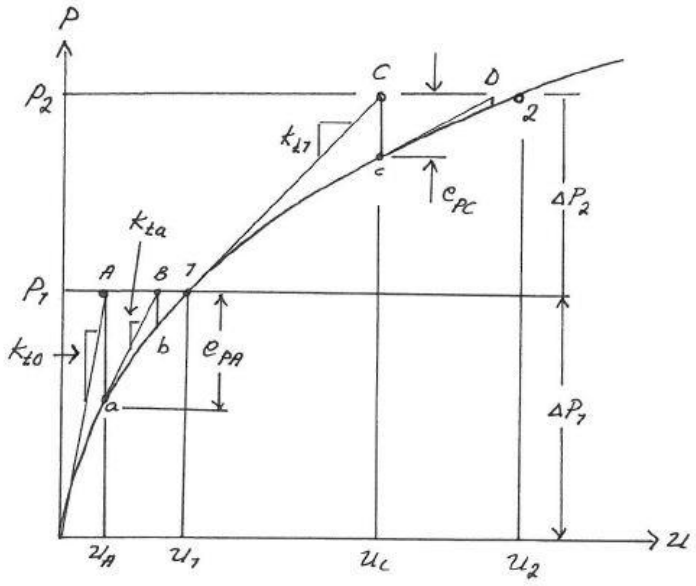

Figure 4.1: Newton-Raphson iteration scheme.

For the case where the initial deformation is u_0 the method according to which equilibrium is found can be described as follows. For the load increment ΔP_1 the corresponding displacement u_1 is sought. By means of the initial tangential stiffness $K_{t,0}$ the displacement increment Δu can be determined as:

$$\Delta u = K_{t,0}^{-1} \Delta P_1 \tag{4.2}$$

Adding this increment to the previous displacement u_0 gives the current estimate u_A of the sought displacement u_1 according to:

$$u_A = u_0 + \Delta u \tag{4.3}$$

The current error, or load imbalance, e_{PA} is defined as the difference between the desired force P_1 and the spring force $K \cdot u_A$ educed by the estimated displacement u_A.

The stiffness *K* is evaluated from the tangent of the function at the point where u_A is found.

$$e_{PA} = P_1 - K \cdot u_A \tag{4.4}$$

However, since the deformation has not been deduced by the current force P_1 this solution is not exact. If the error is larger than the limiting tolerance another attempt is made to find equilibrium.

The new displacement increment Δu starting from the point *a* is calculated by means of the previous imbalance e_{PA}. Hence a displacement u_B closer to the desired u_1 is determined:

$$\Delta u = K_{t,A}^{-1} \cdot e_{PA} \tag{4.5}$$

$$u_B = u_A + \Delta u \tag{4.6}$$

Analogously, if the displacement u_B does not meet the tolerances for the load imbalance according to (4.4) yet another iteration within this load increment is carried out, now starting from point *b*. The iterations continue until the load imbalance approaches zero, the analysis then enters the next load increment ΔP_2 where these iterations are carried out until the load equilibrates to P_2 and the analysis has converged to a numerically acceptable solution u_2 for the load step.

Continued iterations normally cause force errors to decrease, succeeding displacement errors to approach zero and the updated solution to approach the correct value of the displacement. Moreover, smaller load increments can enhance the probability of finding equilibrium within each step.

- **The modified Newton-Raphson method**

The nonlinearity of the equations lies in the internal forces and the stiffness matrix having nonlinear properties. The stiffness matrix is deformation dependent and is therefore updated for each repetition. However, the recalculation of the stiffness matrix is very time consuming and this dependency can be neglected within a load increment in order to preserve linearity of the stiffness tangent. When neglected, the stiffness matrix is calculated based on the value of the deformations prior to the load increment.

This simplification is referred to as the modified Newton-Raphson iteration where the stiffness matrix is only updated for the first iteration in each step (see Figure 4.2).

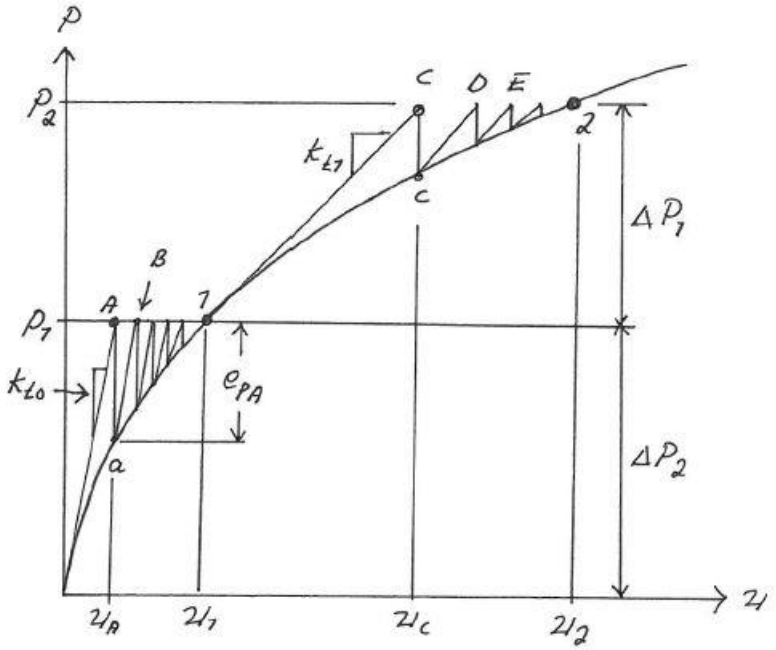

Figure 4.2: Modified Newton-Raphson iteration scheme.

Apart from increasing computing pace, the drawback of this simplification is reduced accuracy.

In the beginning of an analysis quite large load increments can be used. However, when the structure experiences significant loss of stiffness, normally during excessive crack propagation or when approaching failure load, increments need to decrease in order to achieve equilibrium.

The use of smaller load increments can sometimes be insufficient since the stiffness reduction implies increasing deflections while loading decreases. Graphically this is visualized as the change of tangent direction. When the stiffness tangent becomes negative iterations by means of the N-R method fail to find the sought solution.

The Arc Length iteration is such a method.

- **The Arc Length iteration method**

In the Arc Length (AL) iteration a load multiplier is introduced that increases or decreases the intensity of the applied load in order to obtain convergence within a step faster.

With this method the solution path is kept constant and increments of both forces and displacements are iterated as shown in Figure 4.3.

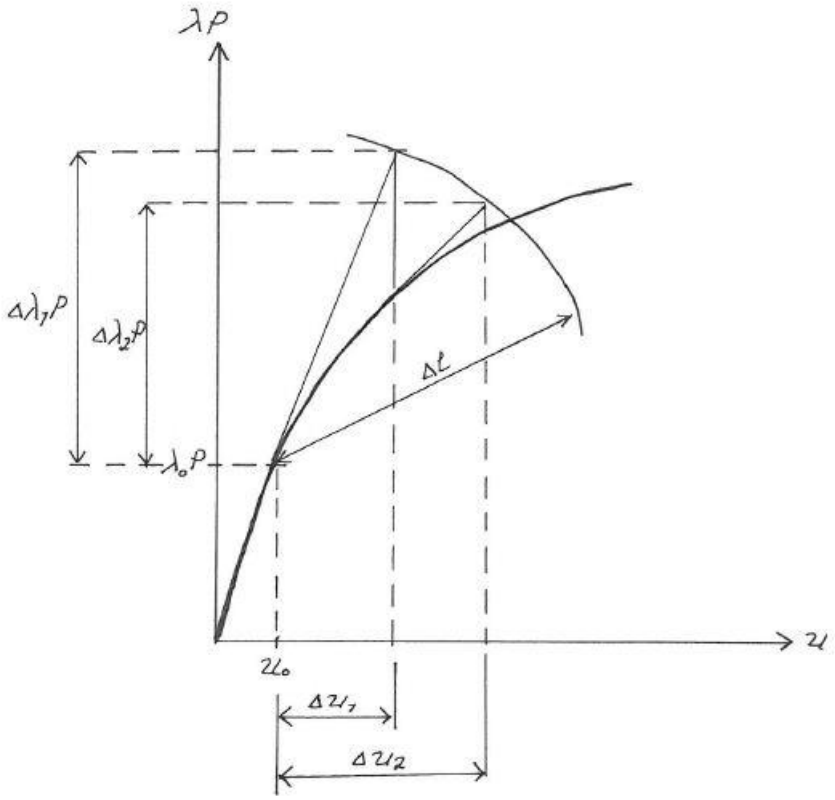

Figure 4.3: Arc Length iteration scheme.

At the end of each step both loading and displacement conditions become fixed. The fixation is performed by establishing the length of the loading vector.

In the N-R formulation the degrees of freedom were associated with the displacements, but for this method an ulterior degree of freedom for the loading must be introduced; the load multiplier λ.

Depending on the structural response the value of λ varies throughout the analysis leading to an increase or decrease of the increment within the step. The value is based on the previous iteration. If convergence difficulties are encountered λ is reduced, whilst for easily converged responses the value is increased resulting in larger load increments.

The Arc Length method presents some advantages compared to the Newton-Raphson as it is very robust and computational efficient. For this reason, it can provide good results even when the N-R method cannot be used. For instance, it is well applicable when large cracks occur and is also able to capture behaviours when the stiffness is decreased, such as snap-through and snap-back phenomena (see Figure 4.4).

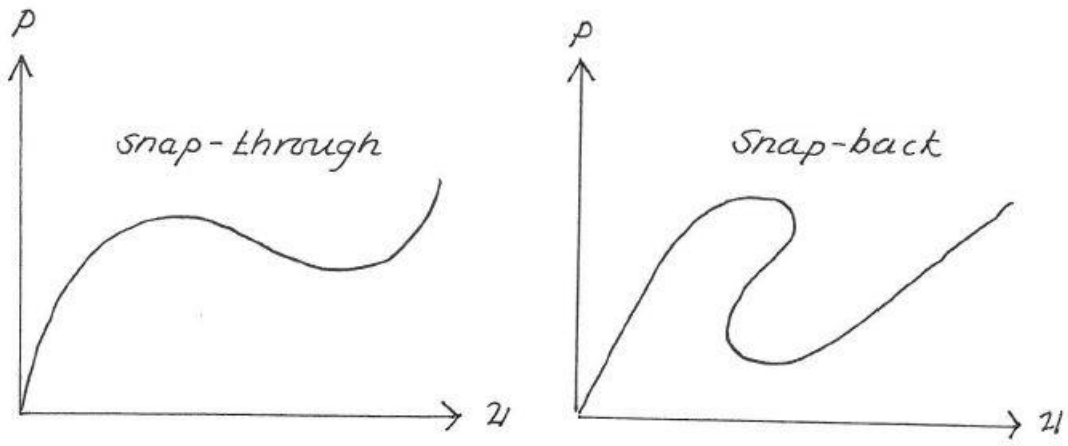

Figure 4.4: Snap-trough and snap-back phenomena.

- **The Initial Stiffening iteration method**

The initial stiffness method uses the stiffness matrix, calculated at the beginning of the analysis stage. And regardless of the load level, the stiffness matrix remains unchanged during the entire process of analysis. This method is used for those analyses, which tend to exhibit instability. Stable solutions are generally found, but relatively small increments result in slow convergence.

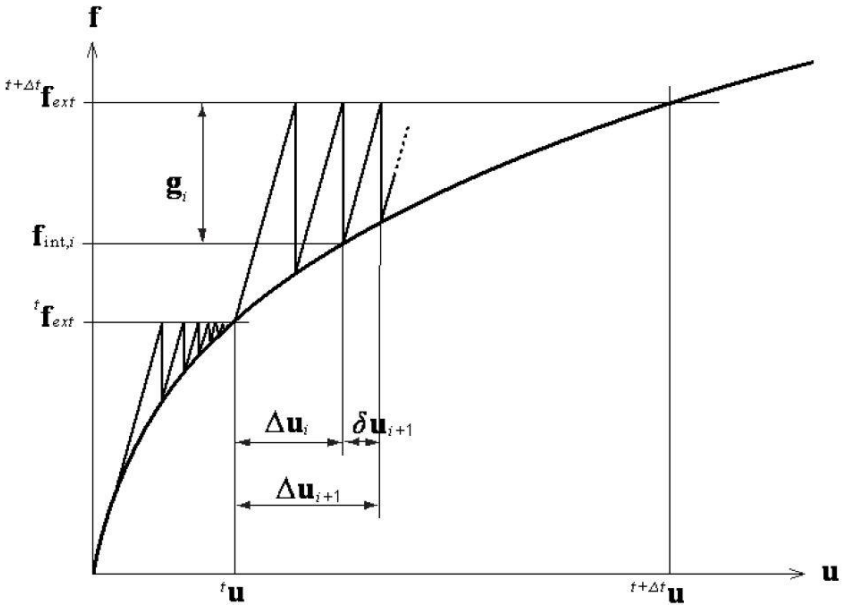

Figure 4.5: Initial Stiffening iteration scheme.

For this work has been chosen the normal Newton-Raphson iteration method. This method has shown good behaviour during the analysis, the only disadvantage shown was that the stiffness matrix must be set up at each iteration and, if a direct solver is used to solve the linear set of equations, the time-consuming decomposition of the matrix has to be performed every iteration as well. In summary, the Regular Newton–Raphson method usually needs only a few iterations, but each iteration is relatively time-consuming.

4.2 Modelling reinforced concrete in Midas FEA.

The modelling and simulations presented in this report have been performed using the Midas FEA software for nonlinear finite element analysis of civil engineering structures.

Now implemented theories and modelling considerations are presented.

Realistic nonlinear finite element analyses of reinforced concrete structures require proper and adequate definitions of material models. When simulating a structural response by means of nonlinear finite element analyses, there are a few aspects regarding the input parameters that need to be addressed. First and foremost, it is important to distinguish between the different aims of analyses before determining the material parameters.

If attempting to simulate an actual response, i.e. behaviour of a conducted experiment, material values as close as possible to the properties of the actual specimen are desirable.

If the aim is to simulate the real response of a no conducted experiment it is appropriate to assign mean values to the material models.

If the purpose of the simulation is to obtain an appropriate design, a safety format must be adopted. In case of an analysis for design, the material parameters should be chosen as the lower characteristic values with applied partial safety factors. Then, the obtained ultimate load from the analysis corresponds to the design resistance. If other safety margins than those proposed by EC2, characteristic values can be combined with the safety factors that are of interest. However, Broo, Lundgren and Plos (2008) [21] have recently confirmed that the use of design values in an analysis does not only scale the response but can in some cases simulate non-realistic responses. Then it is more appropriate to use mean values for the analysis and scale the results for design purposes by means of a global safety factor. How this safety factor should be determined is currently under investigation. In this work, only mean values were used for the material modelling.

4.2.1 Material modelling

With Midas FEA, material properties are automatically generated by the input of concrete compressive strength or the yield strength of steel. However, all values of the generated material properties, especially regarding concrete, are not always in correspondence to the expressions given in EC2 [10] or MC2010 [11] and have therefore been manually assigned to the materials within this study using values obtained during the real tests of these slabs.

Concrete was modelled with the "total strain crack model".

In general analysis models for concrete cracking can be classified into a discrete crack model (discontinuum model) and a smeared crack model (continuum model). The discrete crack model uses finite elements at which concrete cracks are separately represented as boundaries. In the smeared crack model, concrete cracks are assumed to be scattered and distributed, such that discrete elements are not used at the crack locations. The discrete crack model has the advantage of being able to specifically represent such behaviors as physical discontinuity due to concrete cracking and failure and bond slips of reinforcing bars. However, it has some disadvantages in that the accuracy of analysis significantly depends on the material properties required, and that finite element modeling can be quite complex. The smeared crack model assumes that locally generated cracks are evenly scattered over a wide surface. This model is known to be suitable for reinforced concrete structures with reasonable amount of reinforcement, and its finite element modeling is relatively simple.

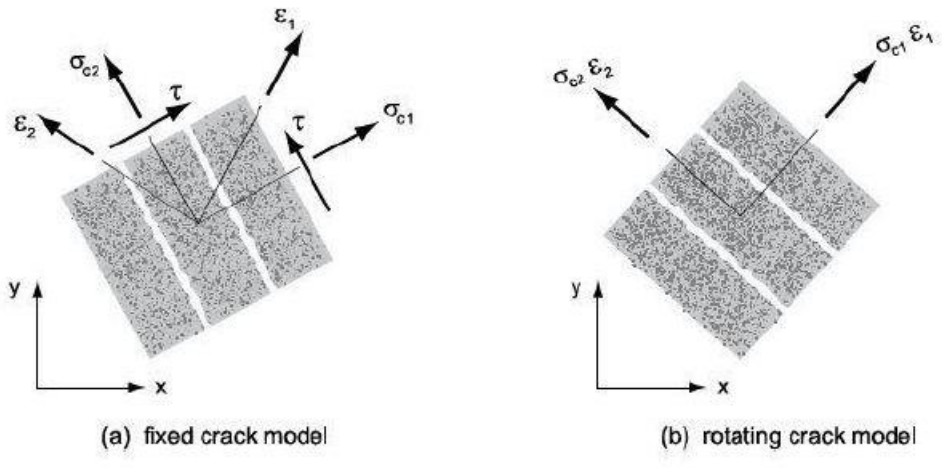

Figure 4.6: Fixed and rotating crack models.

The total strain crack model is classified under the smeared crack model and provides two methods, which are separated into the fixed crack model and the rotating crack model depending on the reference crack axes.

The former assumes that the axes of cracks remain unchanged once the crack axes are defined. On the contrary, the latter is a method in which the directions of the cracks are assumed to continuously rotate depending on the changes in the axes of principle strains, in both cases of the fixed and rotating models the first crack at the integral points always initiates in the directions of the principle strains.

The smeared crack approach is more advantageous than the discrete one, giving satisfying accuracies of global results at low computational costs. In the material model the smeared crack approach is implemented and the features of the cracks are smeared over an entire element. It is important to bear in mind that the smeared crack model disables the cracks to fully open and thus the transfer of tensile stresses through the crack is somewhat higher than in reality.

In addition, concrete subjected to compressive stresses shows a pressure-dependent behavior, i.e., the strength and ductility increase with increasing isotropic stress [22]. Due to the lateral confinement, the compressive stress–strain relationship is modified to incorporate the effects of the increased isotropic stress. Furthermore, it is assumed that the compressive behavior is influenced by lateral cracking [23].

The increase in the strength with increasing isotropic stress is modeled with the four-parameter Hsieh-Ting-Chen failure surface, which is defined as:

$$f = 2.0108\frac{J_2}{f_{cc}^2} + 0.9714\frac{\sqrt{J_2}}{f_{cc}} + 9.1412\frac{f_{c1}}{f_{cc}} + 0.2312\frac{I_1}{f_{cc}} - 1 = 0 \tag{4.7}$$

with the invariants I_1 and J_2 defined in terms of the stress in the concrete σ_{ci} according to:

$$I_1 = \sigma_{c1} + \sigma_{c2} + \sigma_{c3} \tag{4.8}$$

$$J_2 = \frac{1}{6}\left\{\left(\sigma_{c1} - \sigma_{c2}\right)^2 + \left(\sigma_{c2} - \sigma_{c3}\right)^2 + \left(\sigma_{c3} - \sigma_{c1}\right)^2\right\} \tag{4.9}$$

The maximum principle stress f_{c1} is:

$$f_{c1} = \max\left(\sigma_{c1}, \sigma_{c2}, \sigma_{c3}\right) \tag{4.10}$$

This is not the maximum tensile stress but the maximum principal stress. The parameters in Eq. 4.7 are determined by fitting of the uniaxial tensile and compressive strength, the biaxial compressive strength and experimental data of triaxial tests on concrete specimen.

The stress f_{c3} is assumed to result in failure and is determined by scaling the linear elastic stress vector $\sigma_c = s \cdot E \cdot \varepsilon_{nst}$ such that Eq. 4.7 holds true.

The compressive failure stress in multi-axial stress situation is then given by:

$$f_{c3} = s \cdot \min\left(\sigma_{c1}, \sigma_{c2}, \sigma_{c3}\right) \tag{4.11}$$

If the scaling factor *s* is negative, thus resulting in a positive failure stress, the stress vector f_{c3} is scaled to the tensile side of the failure surface, and the failure strength is set equal to a large negative value ($-30 f_{cc}$). The failure strength f_{cf} is given by:

$$f_{cf} = -f_{c3} \tag{4.12}$$

The peak stress factor K_σ is given by Selby:

$$K_\sigma = \frac{f_{cf}}{f_{cc}} \geq 1 \tag{4.13}$$

and the peak strain factor is assumed to be:

$$K_\varepsilon = K_\sigma \tag{4.14}$$

In unconfined compression, the values at the peak are given by the values of uniaxial compressive strength, and the peak stress factor is equal to one.

The parameters of the compressive stress– strain function now become:

$$f_{cf} = K_\sigma f_{cc} \quad , \quad \varepsilon_p = K_\sigma \varepsilon_0 \tag{4.15}$$

The value of the initial strain ε_0 is given by the relationship:

$$\varepsilon_0 = -\frac{n}{n-1}\frac{f_{cc}}{E_c} \tag{4.16}$$

The equations given above result in a gradual increase in the maximum strength in confined compression, with an initial slope of the stress–strain diagram given by the Young's modulus. In a full triaxial stress situation, the failure surface cannot be reached and a linear stress–strain relation is obtained (Figure 4.7)

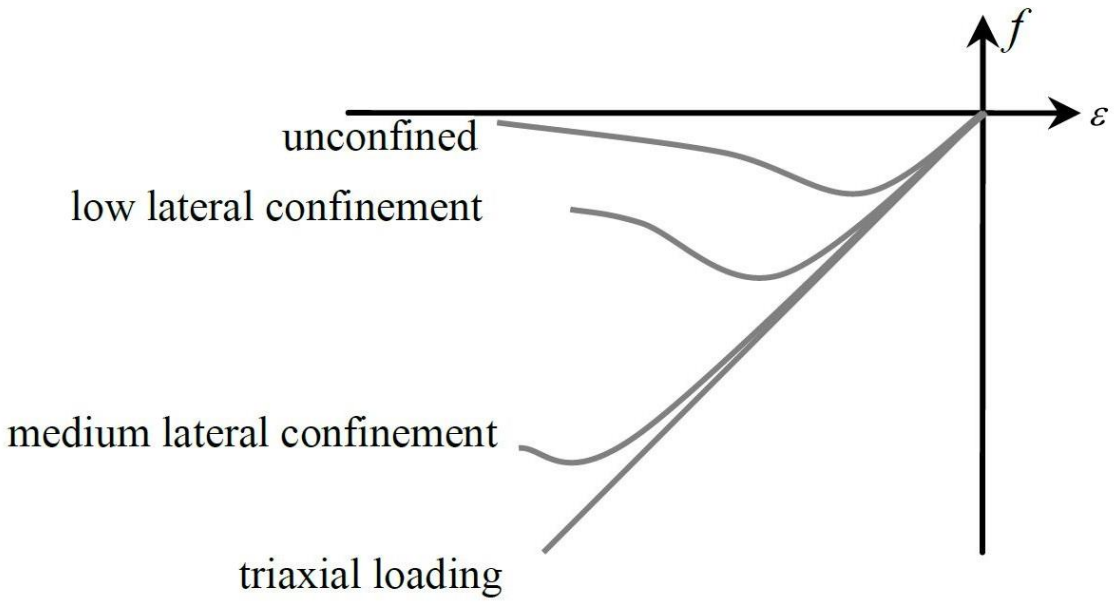

Figure 4.7: Influence of lateral confinement on compressive-strain curves.

Furthermore, it is assumed that the compressive behavior is influenced by lateral cracking.

In cracked concrete, large tensile strains perpendicular to the principal compressive direction reduce the concrete compressive strength. The compressive strength f_p is consequently not only a function of the internal variable ε_i, but is also a function of the internal variables governing the tensile damage in the lateral directions $\varepsilon_{l,1}$, $\varepsilon_{l,2}$. The reduction factors due to lateral cracking are denoted as $\beta_{\varepsilon cr} = \beta_{\varepsilon cr}(\varepsilon_{lat})$ and $\beta_{\sigma cr} = \beta_{\sigma cr}(\varepsilon_{lat})$ which are functions of the average lateral damage variable given by $\varepsilon_{lat} = \sqrt{\varepsilon_{l,1}^2 + \varepsilon_{l,2}^2}$.

The relationship for reduction due to lateral cracking is the model according to Vecchio and Collins (Figure 4.8).

$$\beta_{\sigma cr} = \frac{1}{1+K_c} \leq 1 \tag{4.17}$$

Where $K_c = 0.27\left(-\frac{\varepsilon_{lat}}{\varepsilon_0} - 0.37\right)$ and $\beta_{\varepsilon cr} = 1$

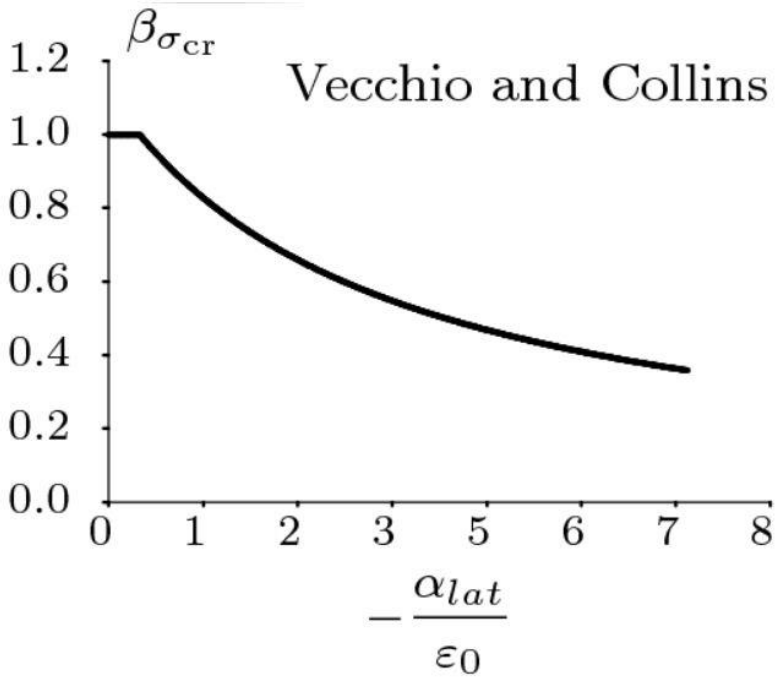

Figure 4.8: Reduction factor due to lateral cracking (Vecchio and Collins).

Midas FEA has implemented various models that simulate concrete's behaviour and in particular three of these were used for compression behaviour and one for tension. Then a parametric analysis has been conducted in order to obtain the best fitting result.

- **Thorenfeldt model**

The first model for compression behaviour is the one proposed by Thorenfeldt [24] (Figure 4.9).

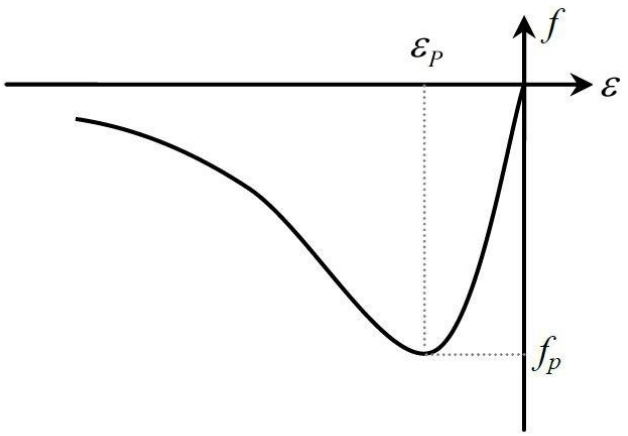

Figure 4.9: Thorenfeldt model.

The equation of the Thorenfeldt curved line is expressed by:

$$f = -f_p \frac{\varepsilon_i}{\varepsilon_p} \left(\frac{n}{n - 1 + \left(\frac{\varepsilon_i}{\varepsilon_p} \right)^{nk}} \right) \tag{4.18}$$

Where *n* and *k* are:

$$n = 0.8 + \frac{f_{cc}}{17} \tag{4.19}$$

$$k = \begin{cases} 1 & \text{if } 0 > \varepsilon > \varepsilon_p \\ 0.67 + \frac{f_{cc}}{62} & \text{if } \varepsilon \le \varepsilon_p \end{cases} \tag{4.20}$$

This model requires the value of f_p that is known, and the peak strain ε_p that needs some consideration about the confinement conditions of concrete and lateral cracking.
The increased ductility of confined concrete is modeled by a linear adoption of the descending branch of the Thorenfeldt curve according to:

$$f_i = -f_p \left(1 - (1 - r) \frac{\varepsilon_i - \varepsilon_p}{\varepsilon_u - \varepsilon_p} \right) \le -r \cdot f_p \tag{4.21}$$

r is the factor, which models the residual strength of the material (see Figure 4.10).

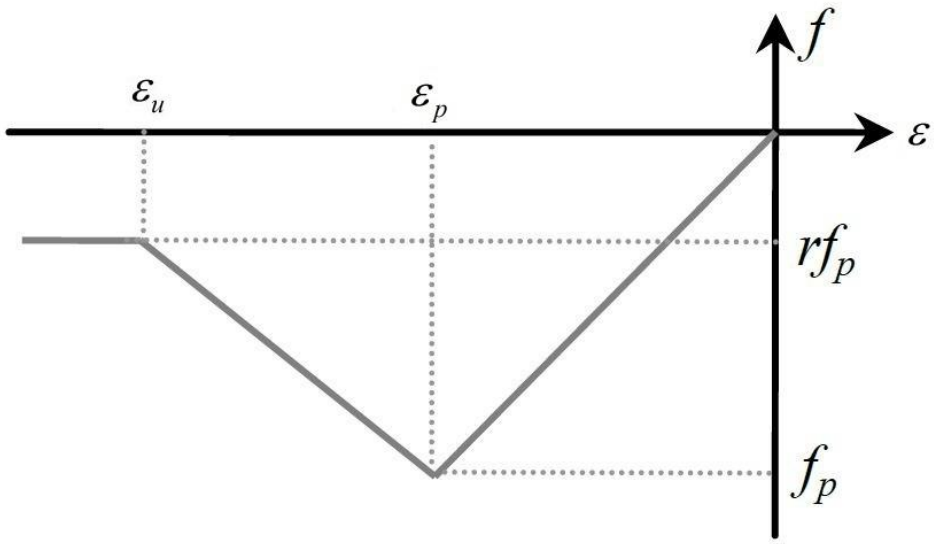

Figure 4.10: Compressive behaviour under lateral confinement used for thorenfeldt.

The ultimate strain in compression is assumed to be determined by the ratio between the peak strength and the compression strength and the strain at the peak according to Eq. 4.22

$$\varepsilon_u = \left(\frac{f_p}{f_{cc}} \right)^{\gamma} \varepsilon_p \tag{4.22}$$

The scalar γ needs to be determined; in this work $\gamma = 3$ is assumed.

The residual strength $r \cdot f_p$ also depends on the ratio between the peak strength and the compressive strength according to Eq. 4.23

$$r = \left(\frac{f_p}{f_{cc}} \right)^{\gamma} r_0 \tag{4.23}$$

r_0 is an initial value. It is assumed $r_0 = 0.1$.

The linear compression–softening relationship is only applied to the Thorenfeldt curve if the peak value f_p is considerably larger than the compressive strength f_{cc}. Has been assumed $f_p / f_{cc} > 1.05$. In case lateral compression and lateral cracking result in $f_p / f_{cc} < 1.05$, the ductility of the material will not increase.

- **Parabolic model (Feenstra)**

The Parabolic Model suggested by Feenstra [25] is derived on the basis of the fracture energy (Figure 4.11).

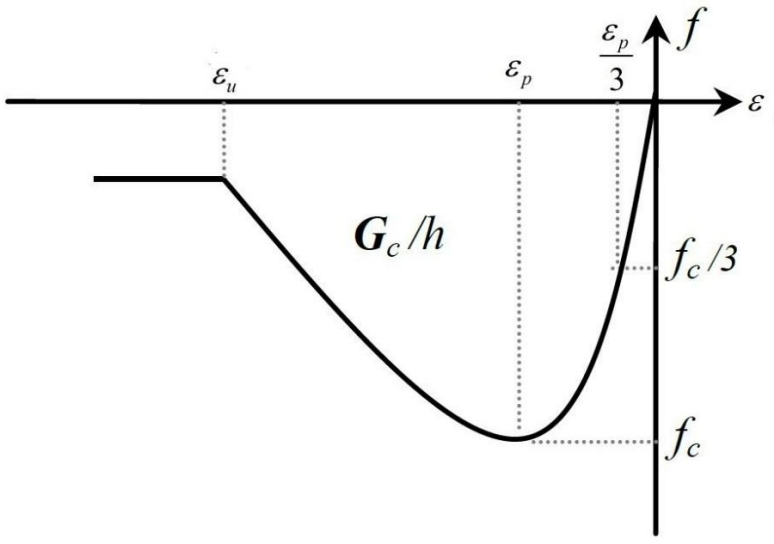

Figure 4.11: Feenstra model.

This curved line is presented by the following three characteristic variables: compressive strength $f_c > 0$, compressive fracture energy $G_c > 0$, characteristic element length $h > 0$.

$$G_c = 100 \cdot G_f = 100 \cdot \left(0{,}028 \cdot {f_{cm}}^{0{,}18} \cdot {d_g}^{0{,}32}\right) \tag{4.24}$$

Where:

G_f is the tensile fracture energy.

f_{cm} is the mean compressive strength.

d_g is the maximum size of the aggregate.

The strain $\varepsilon_p / 3$ at which one-third of the maximum compressive strength f_c is reached, is:

$$\frac{\varepsilon_p}{3} = \frac{1}{3}\frac{f_c}{E_c} \tag{4.25}$$

The strain ε_p at which the maximum compressive strength is reached, is:

$$\varepsilon_p = -\frac{4}{3}\frac{f_c}{E_c} = 4\frac{\varepsilon_p}{3} \tag{4.26}$$

Note that $\varepsilon_p / 3$ and ε_p are determined irrespective of the element size or compressive fracture energy. Finally, the ultimate strain ε_p, at which the material is completely softened in compression, is:

$$\varepsilon_u = \varepsilon_p - \frac{3}{2}\frac{G_c}{h \cdot f_c} \tag{4.27}$$

Based on the above variables, the following curved line is defined:

$$f = \begin{cases} -f_c \dfrac{1}{3}\dfrac{\varepsilon_j}{\varepsilon_{p/3}} & if\ \ 0 \le \varepsilon_j < \varepsilon_{p/3} \\ -f_c \dfrac{1}{3}\left(1 + 4\left(\dfrac{\varepsilon_j - \varepsilon_{p/3}}{\varepsilon_p - \varepsilon_{p/3}}\right) - 2\left(\dfrac{\varepsilon_j - \varepsilon_{p/3}}{\varepsilon_p - \varepsilon_{p/3}}\right)^2\right) & if\ \ \varepsilon_{p/3} \le \varepsilon_j < \varepsilon_p \\ -f_c\left(1 - \left(\dfrac{\varepsilon_j - \varepsilon_p}{\varepsilon_u - \varepsilon_p}\right)^2\right) & if\ \ \varepsilon_p \le \varepsilon_j < \varepsilon_u \\ 0 & if\ \ \varepsilon_u \le \varepsilon_j \end{cases} \tag{4.28}$$

It could now easily be verified that the fracture energy G_c and the characteristic element length *h* govern the softening part of the curve only:

$$\int_{\varepsilon_p}^{\varepsilon_u} f \, d\varepsilon_j = f_c \left(\varepsilon_j - \frac{1}{3} \left(\frac{\varepsilon_j - \varepsilon_p}{\varepsilon_u - \varepsilon_p} \right)^3 \right) = \frac{G_c}{h} \tag{4.29}$$

- **Parabola-rectangle stress distribution (EC2)**

The third model is the simplified constitutive law for concrete compressive behaviour named parabola-rectangle distribution [10].

This model depends only on the final compressive strength f_c, and the strains $\varepsilon_{c2} = 2‰$ and $\varepsilon_{cu} = 3.5‰$.

The following curved line is defined:

$$\begin{cases} \sigma_c(\varepsilon_c) = 2\dfrac{f_c}{\varepsilon_{c2}}\varepsilon_c\left(1 - \dfrac{\varepsilon_c}{2\varepsilon_{c2}}\right) & if \ \varepsilon_c \le \varepsilon_{c2} \\ \sigma_c(\varepsilon_c) = f_c & if \ \varepsilon_{c2} \le \varepsilon_c \le \varepsilon_{cu} \end{cases} \tag{4.30}$$

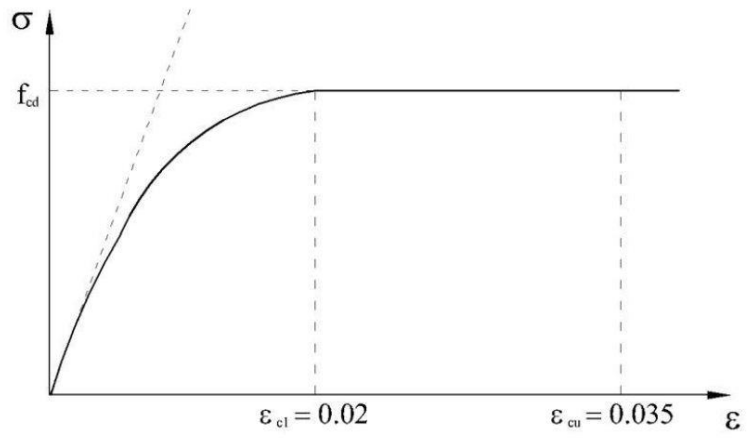

Figure 4.12: Parabola-rectangle model EC2.

This model has been created using a Multilinear model in Midas FEA (Figure 4.13).

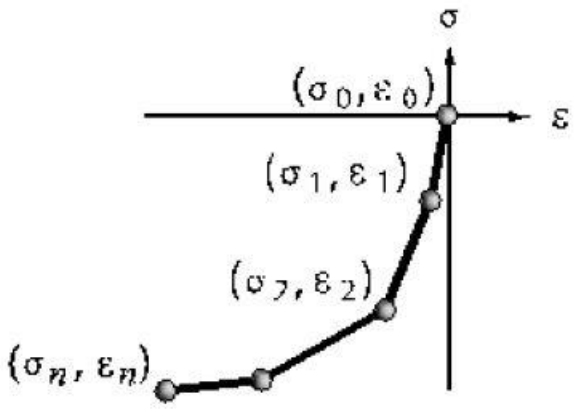

Figure 4.13: Multilinear function in Midas FEA.

The concrete material model has been developed with two separate models for tensile and compression behaviour that can be used simultaneously.

The tensile behavior model defined by the total strain crack model has elastic, ideal, brittle, linear, exponential, Hordijk, multi-linear and user-defined behaviors. The total strain crack model materializes the softening function based on the fracture energy. In case of a smeared crack model, these models have a relation with crack bandwidth.

Only the Hordijk model was used in this work.

- **Hordijk model**

Hordijk, Cornelissen and Reinhardt [26] proposed an expression for the softening behavior of concrete, which also results in a crack stress equal to zero at a crack strain (Figure 4.21). Use the following values as input: tensile strength $f_t > 0$, tensile fracture energy $G_f > 0$, crack band width $h > 0$. The function is defined by Eq. 4.31.

$$\begin{cases} \dfrac{\sigma_{nn}^{cr}(\varepsilon_{nn}^{cr})}{f_t} = \left(1 + \left(c_1 \dfrac{\varepsilon_{nn}^{cr}}{\varepsilon_{nn.ult}^{cr}}\right)^3\right)\exp\left(-c_2 \dfrac{\varepsilon_{nn}^{cr}}{\varepsilon_{nn.ult}^{cr}}\right) - \dfrac{\varepsilon_{nn}^{cr}}{\varepsilon_{nn.ult}^{cr}}(1 + c_1^3)\exp(-c_2) & se\ 0 < \varepsilon_{nn}^{cr} < \varepsilon_{nn.ult}^{cr} \\ \dfrac{\sigma_{nn}^{cr}(\varepsilon_{nn}^{cr})}{f_t} = 0 & se\ \varepsilon_{nn.ult}^{cr} < \varepsilon_{nn}^{cr} < 0 \end{cases} \quad (4.31)$$

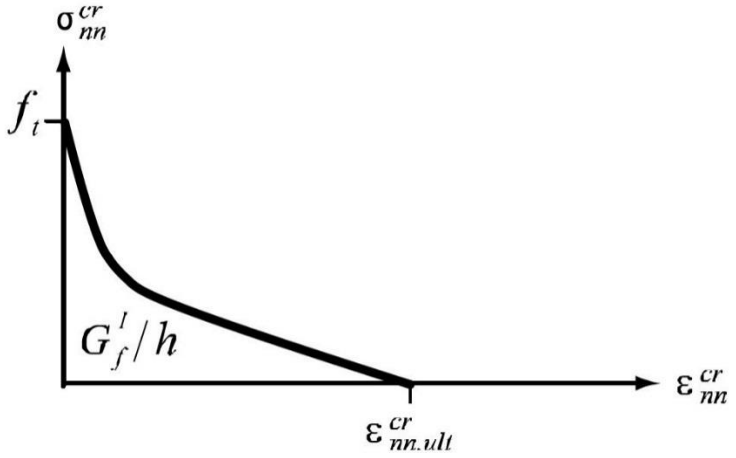

Figure 4.14: Hordijk model.

The parameters $c_1 = 3$, $c_2 = 6.93$.

The ultimate crack strain then is written as:

$$\varepsilon_{nn.ult}^{cr} = \frac{G_f^I}{h f_t} \tag{4.32}$$

- **Reinforcement model**

Rather than defining reinforcements with distinct finite elements, the concept of embedded reinforcements can be used with this software. In this concept the stiffness of the reinforcements is added to the stiffness of the continuum elements in which the reinforcements are located, the continuum elements in which reinforcement is embedded are called mother elements.

In this analysis all the elements are “bar in solid” elements where the stiffness of the divided bar reinforcement segments will be added to the stiffness of the corresponding mother elements. In bar reinforcement segments, 2 integration points are used for the line type and 1 integration point is used for the point type reinforcement. The locations of the integration points are automatically calculated.

Steel for reinforcement is modeled with Von Mises model that is one that is mostly used for analysis of metallic materials. It assumes that yielding occurs when a regular octahedral shear stress τ_{oct} reaches a defined limit.

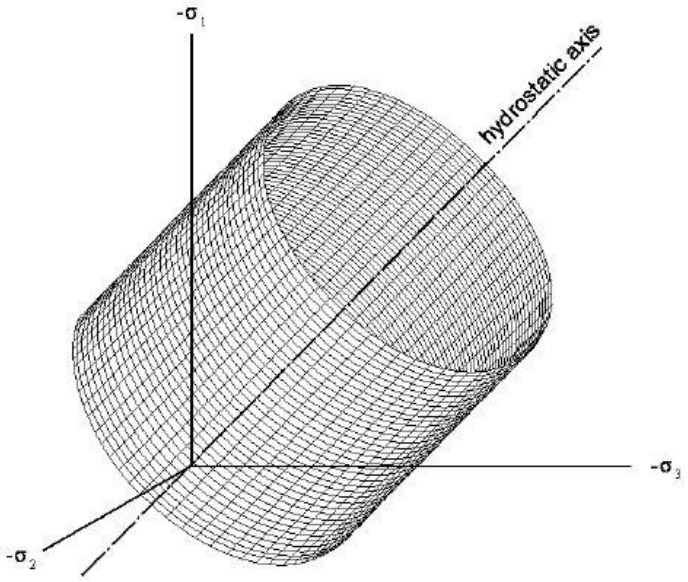

Figure 4.15: Von Mises yield surface.

It was necessary to create a hardening function to describe the response of the steel used in the real test.

Von Mises hardening behavior model follows the strain hardening hypothesis, which assumes that hardening progresses with increase in plastic deformation.

4.2.2 Calculation of the crack bandwidth "*h*"

In order to obtain a good simulation, has been studied the influence of the parameter *h* on the analysis. This parameter is needed in both Feenstra and Hordijk models. For 3D elements the crack bandwidth can be defined as the cubic root of the element's volume [27]. The mesh was formed by tetrahedral elements so initially has been calculated as $h = \sqrt{V} = 15mm$. Then, using code provisions from EN 1992-1-1: 2004 [10], were studied all the models using $h = S_{r,\max}$ and $h = S_{r,\max} / 2$, where $S_{r,\max}$ is the maximum crack spacing (Eq. 4.33).

$$S_{r,\max} = k_3 \cdot c + k_1 \cdot k_2 \cdot k_4 \cdot \frac{\phi}{\rho_{p,eff}} \tag{4.33}$$

Where:

ϕ is the bar diameter. Where a mixture of bar diameters is used in a section, an equivalent diameter ϕ_{eq} should be used. For a section with n_1 bars of diameter ϕ_1 and n_2 bars of diameter ϕ_2, the following expression should be used $\phi_{eq} = \frac{n_1\phi_1^2 + n_2\phi_2^2}{n_1\phi_1 + n_2\phi_2}$

c is the cover to the longitudinal reinforcement.

k_1 is a coefficient which takes account of the bond properties of the bonded reinforcement. Is equal to 0.8 for high bond bars and 1.6 for bars with an effectively plain surface (e.g. prestressing tendons).

k_2 is a coefficient which takes account of the distribution of strain. Is equal to 0.5 for bending, 1 for pure tension and for cases of eccentric tension or for local areas intermediate values of k_2 should be calculated from the relation $k_2 = (\varepsilon_1 + \varepsilon_2)/(2\varepsilon_1)$, Where ε_1 is the greater and ε_2 is the lesser tensile strain at the boundaries of the section considered, assessed on the basis of a cracked section.

The values of k_3 and k_4 for use in a Country may be found in its National Annex. The recommended values are 3,4 and 0,425 respectively.

Ultimately ρ_{eff} can be calculated using Eq. 4.34:

$$\rho_{eff} = \frac{A_s}{A_{c,eff}} \tag{4.34}$$

Where $A_{c,eff} = b \cdot h_{eff}$ and $h_{eff} = \min\{2{,}5(h-d);(h-x);(h/2)\}$.

Chapter 5

Simulation of laboratory tests

5.1 Laboratory for test comparison.

Three test specimens belonging to previous researches have been simulated in Midas FEA. The first simulated specimen was a slab-column connection tested by Bamidele Adetifa and Maria Anna Polak (2005) [28] denoted *SB1*. The test specimen *SB1* had no shear reinforcement and the height of the slab specimen was 120 mm with square shape (1800x1800mm). This isolated slab-column connection is loaded through the column and simply supported along the edges with restraints applied at the in-plane distances of 1500 x 1500 mm. The height of the column extending from the top and the bottom faces of the slab was 150 mm. Details and dimensions are shown in Figure 5.1.

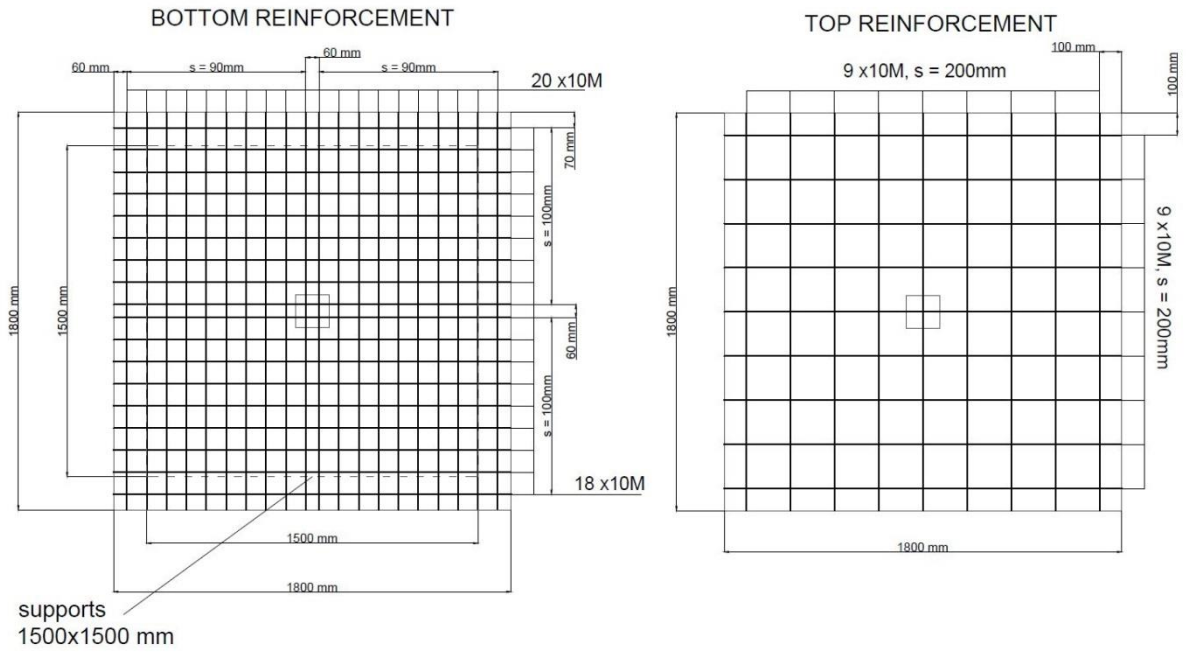

Figure 5.1: Dimensions and flexural reinforcement of *SB1* specimen.

The setup for testing is shown in Figure 5.2 and 5.3.

The setup was built around a testing frame. Simple supports at the edges were achieved by using 40 mm-wide, 25 mm-thick steel plates placed on a rigid pedestal system constructed from W-sections. Neoprene strips were bonded to the bearing plates underneath the slab to ensure uniformity of contact and allow rotations at supports. The specimens were subjected to concentric axial load only through a hydraulic actuator. To simulate continuous slab construction and avoid the slab edges lifting during testing, the corners of the slabs were held down. The slabs were tested by applying a load through the column until failure. The slab was loaded in displacement control.

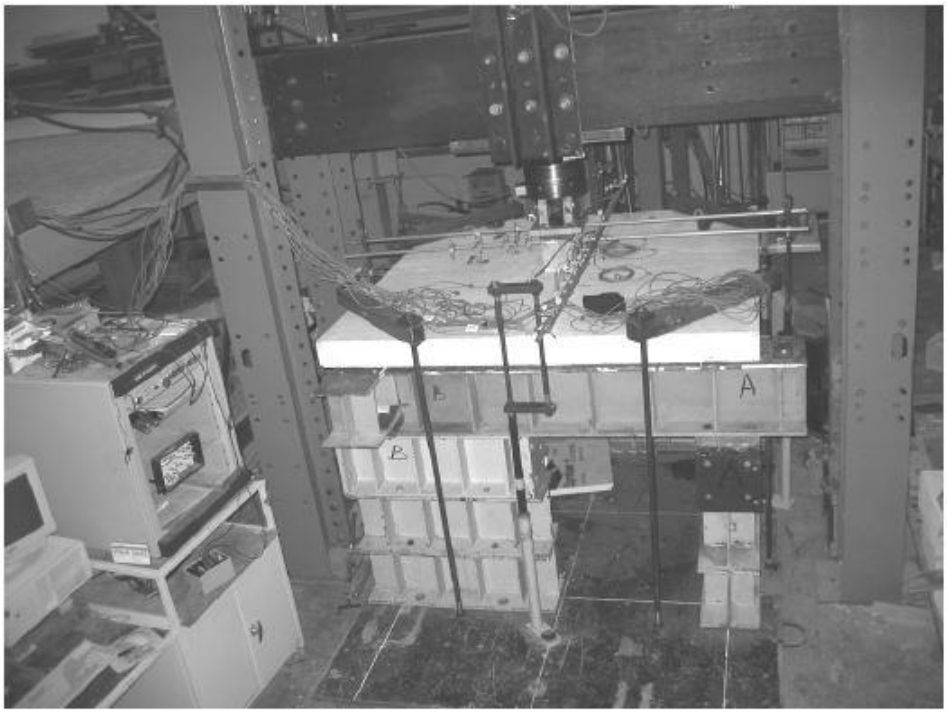

Figure 5.2: Experimental setup with specimen *SB1*.

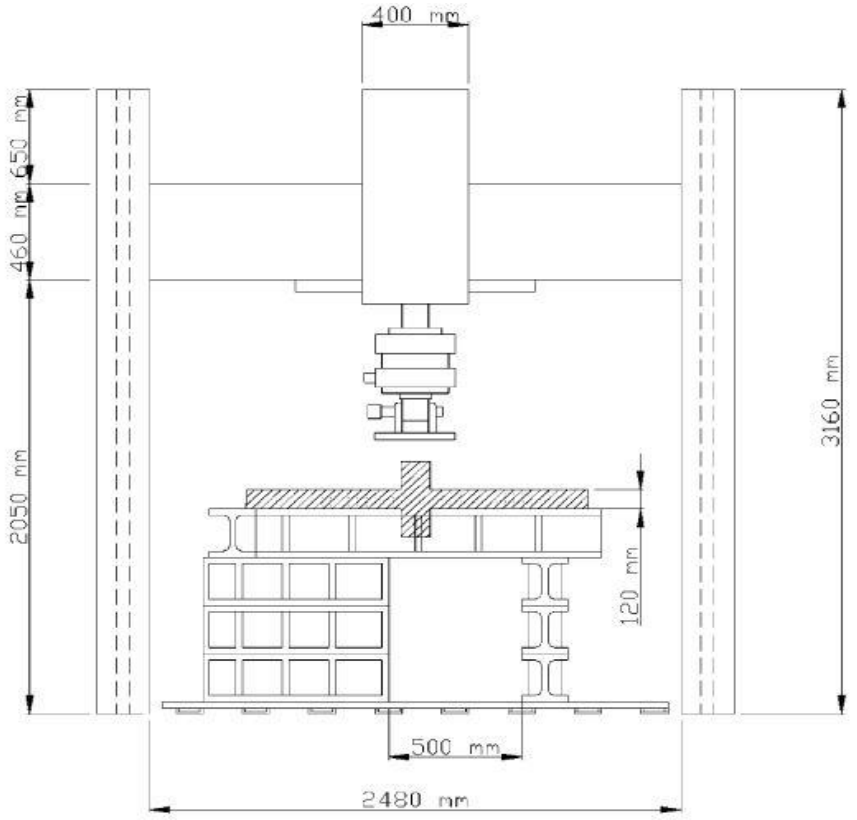

Figure 5.3: Schematic of experimental setup *SB1*.

Slab *SB1* was loaded by applying a velocity that increased from 0 mm/s to 40 mm/s, such that the slab displaced at a rate of 20 mm/s.

The second simulated specimen was the corner supported slab denoted *R1* from the experiments conducted by Ingvarsson (1977) [29]. It consisted of a rectangular slab (1855x2145x120 mm) supported on its corners by rectangular concrete columns, (Figure 5.4).

Loads were concentrated forces applied in 16 neoprene bearings symmetrically disposed around the centre of the slab.

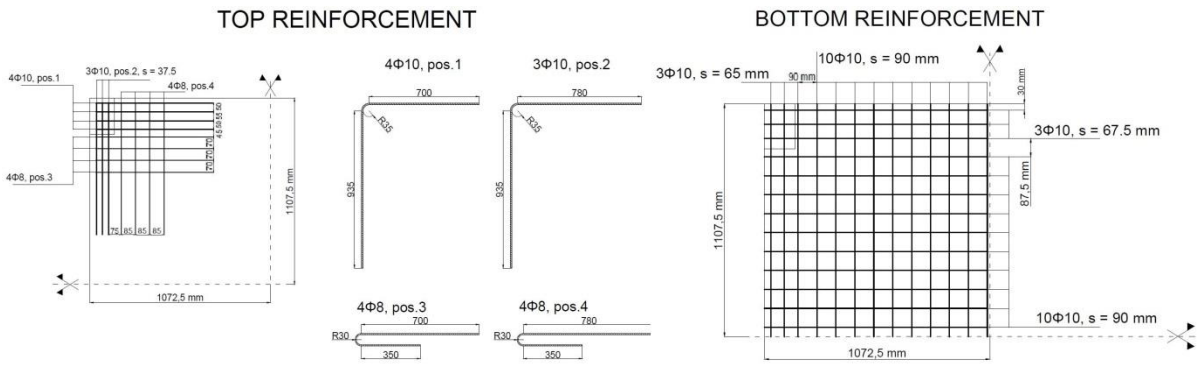

Figure 5.4: Schematic of flexural bottom reinforcement type of slab *R1*.

The last simulated specimen was the edge supported slab denoted *No.2* in the report of Kinnunen (1971) [5]. Specimen *No.2* was a rectangular slab (3000x1800x130 mm) supported on its opposite short edges by square concrete columns (Figure 5.5). Along its longer edges the slab was unsupported and believed to be limited by lines of shear force peaks. All specimens experienced failure in punching shear.

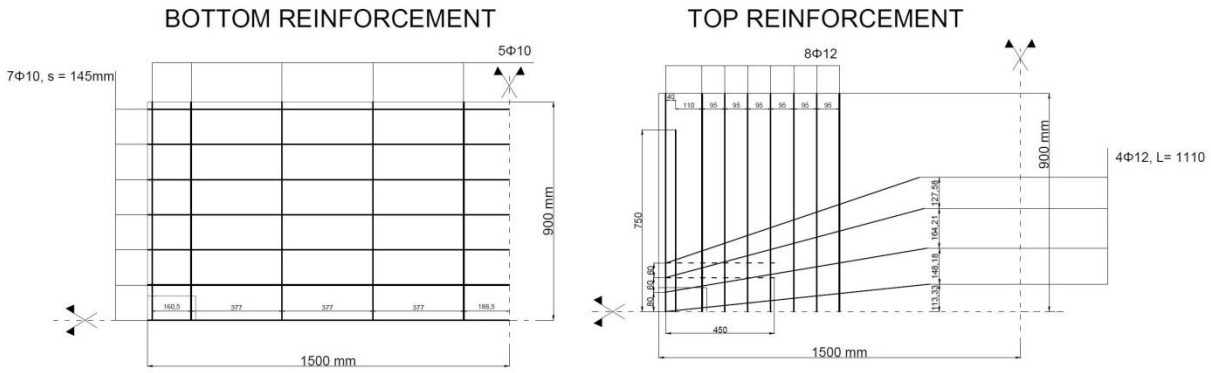

Figure 5.5: Schematic of flexural reinforcement type of slab no.2.

This model was charged on 8 neoprene bearings around the centre. During testing of the specimens, several types of data were measured throughout the loading; reinforcement strains, concrete compressive strains on the bottom surface near the columns, slab deflections and rotations. In addition, observations were made on crack propagation at each load step in order to distinguish the crack patterns. The comparisons have been limited to load-displacement responses, crack patterns and failure modes. In figure 5.6 is shown the response in terms of forces and displacements; applied on top of the column for slab *SB1* and on the neoprene bearings for *R1* and *no.2*. The displacement was measured in the column's centre for *SB1*, and in the centre of the slab for *R1* and *no.2*.

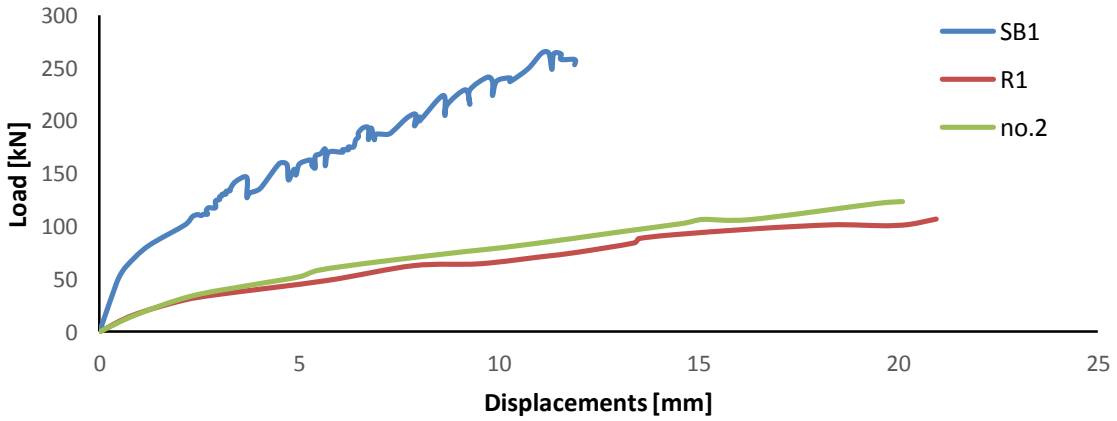

Figure 5.6: Load – displacement measured during tests.

5.2 Simulation of laboratory tests.

The first specimen has been modelled entire;

Slab *SB1* has been simply supported along the edges, but in order to simulate the real behavior it was necessary to use further restraints along the edges of the central column (to avoid buckling) and on the corners of the slab to held them down during the loading process. (Figure 5.7)

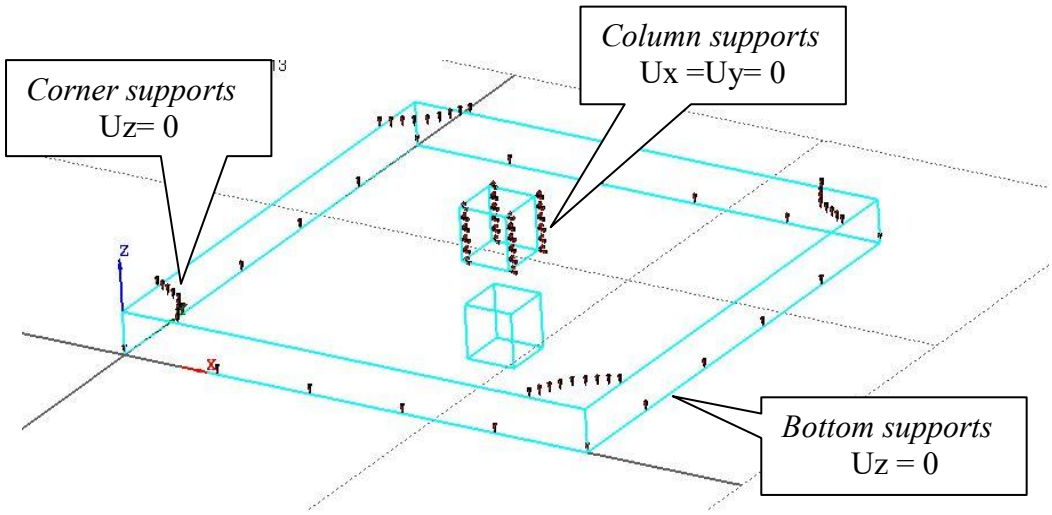

Figure 5.7: Boundary conditions for slab *SB1*.

For specimens *R1* and *no.2* in order to reduce required computer capacity, it was convenient and, due to symmetry, sufficient to only model a quarter of the test specimens. In the symmetries boundary conditions were introduced such that free movement was prevented in the direction with geometrical continuity. Apart from the symmetry lines, boundary conditions were added for the column supports fixing every movement at the base of the structure.

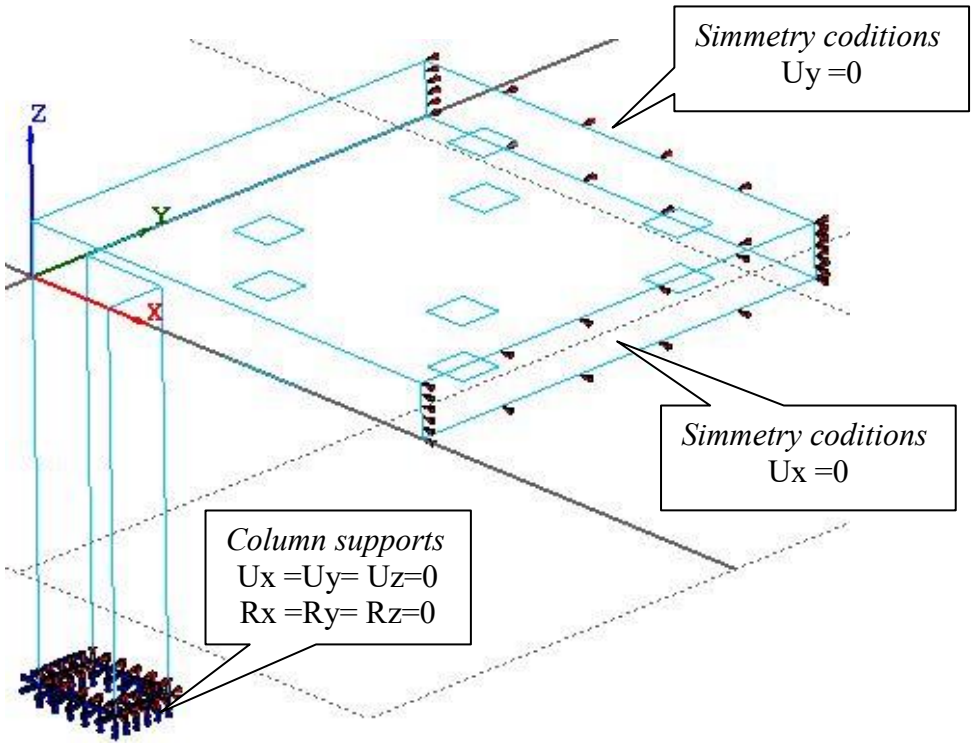

Figure 5.8: Boundary conditions for slab *R1*.

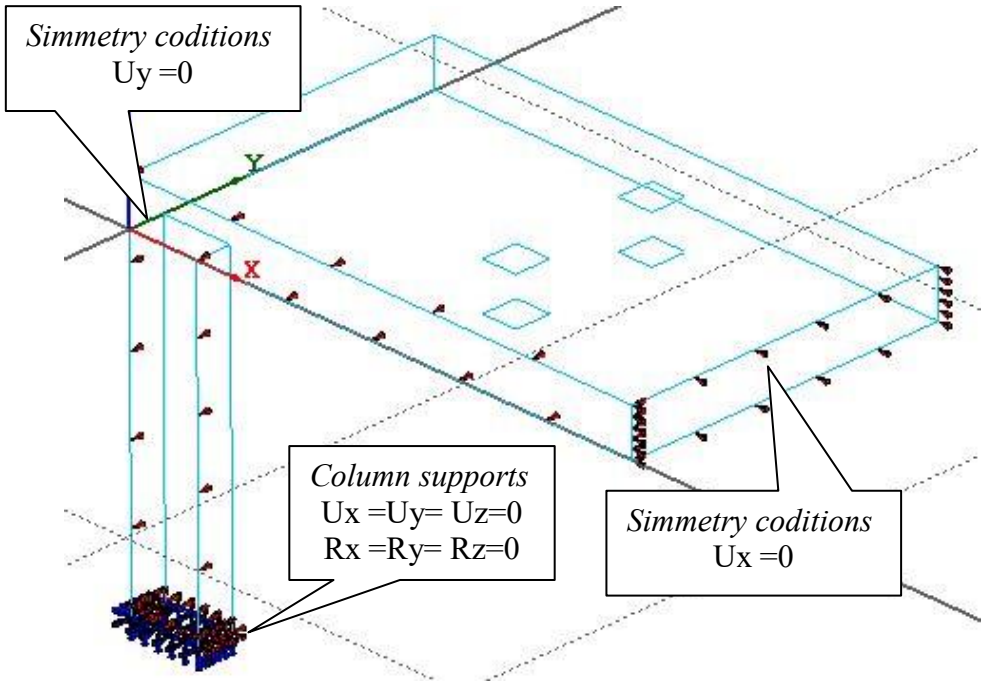

Figure 5.9: Boundary conditions for slab *no.2*.

The mesh of all models was formed by solid tetrahedral elements. Meshed models can be seen in Figure 5.10, where specimen *SB1* was divided into 73468 finite elements, *R1* into 309502 finite elements and specimen *Nr. 2 i*nto 350621 finite elements.

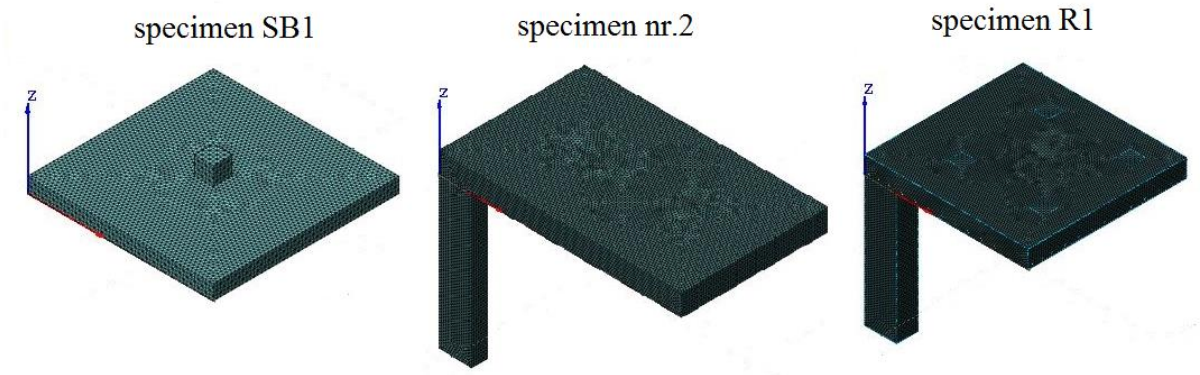

Figure 5.10: Mesh configuration of specimens.

Finally, Reported concrete and steel strengths, for the compared specimens, were determined according to a former European standard. Material data for the three specimens are presented in Table 5.1.

Table 5.1 Material data for specimen

	f_c [MPa]	f_t [MPa]	υ [-]	G_c [N/mm]	G_f [N/mm]	E_c [MPa]	f_y [MPa]	f_u [MPa]	ε_y [-]	ε_u [-]
SB1	44	2.2	0.15	7	0.07	28000	455	650	0.0023	0.05
R1	28	2	0.15	7.251	0.07251	29030	470	470	0.0023	0.05
No.2	26	1.86	0.15	6.913	0.069134	28432	420	420	0.0023	0.05

The column load at failure of specimen *SB1* had the average value of 253 kN, for specimen *R1* the average value for failure was 107 kN and for *no.2* was 123 kN. During the analyses these loads have been divided in 25 load steps.

Each structure has been modelled three times with each compression law, modifying the crack bandwidth, then analysed other 3 times including confinement effect and lateral cracking (only for Feenstra and Thorenfeldt models), reaching a total of 3x3x5=45 analyses.

Analysis combinations are shown in Table 5.2, 5.3 and 5.4 for specimen *SB1*, *R1* and *no.2* respectively.

Table 5.2 Combinations used for *SB1* specimen

	Compression model	Tension model	h [mm]
1	EC2	Hordijk	15
2	Feenstra	Hordijk	123
3	Thorenfeldt	Hordijk	245
4	EC2	Hordijk	15
5	Feenstra	Hordijk	123
6	Thorenfeldt	Hordijk	245
7	EC2	Hordijk	15
8	Feenstra	Hordijk	123
9	Thorenfeldt	Hordijk	245

Table 5.3 Combinations used for *no.2* specimen

	Compression model	Tension model	h [mm]
1	EC2	Hordijk	15
2	Feenstra	Hordijk	92.5
3	Thorenfeldt	Hordijk	185
4	EC2	Hordijk	15
5	Feenstra	Hordijk	92.5
6	Thorenfeldt	Hordijk	185
7	EC2	Hordijk	15
8	Feenstra	Hordijk	92.5
9	Thorenfeldt	Hordijk	185

Table 5.4 Combinations used for *R1* specimen

	Compression model	Tension model	h [mm]
1	EC2	Hordijk	15
2	Feenstra	Hordijk	65
3	Thorenfeldt	Hordijk	130
4	EC2	Hordijk	15
5	Feenstra	Hordijk	65
6	Thorenfeldt	Hordijk	130
7	EC2	Hordijk	15
8	Feenstra	Hordijk	65
9	Thorenfeldt	Hordijk	130

Numerical results are classified with a code like XX-hYYY-ZZZ where: XX can be Th or Fe or PR respectively for Thorenfeldt, Feenstra or Parabolic-rectangle compression curves, h is the crack bandwidth and YYY is its value in mm, calculated according 4.2.2, ZZZ can be NCC for analyses where the effect of lateral compression and lateral cracking is not taken into account or YCC when these two effects are taken into account.

The comparison has been made between numerical outputs and experimental ones in term of ultimate load, P_u, and displacement of the reference point, δ_u.

5.3 Results from analyses, specimen *SB1*.

Table 5.5 presents the final analysis results in terms of ultimate load-displacement for slab *SB1* in every combination made. The simulation gives brittle punching shear failure as in the experiment.

Table 5.5 Ultimate load and displacement for each combination, *SB1* specimen

	Specimen *SB1*	Ultimate displacement [mm]	Ultimate load [kN]
	experimental	**11.90**	**253**
1	**Th-h015-NCC**	15.16	258.7
2	**Th-h123-NCC**	15.56	253.5
3	**Th-h245-NCC**	15.85	269.1
4	**Fe-h015-NCC**	13.27	258.7
5	**Fe-h123-NCC**	15.48	253.5
6	**Fe-h245-NCC**	16.74	269.1
7	**Th-h015-YCC**	14.28	258.7
8	**Th-h123-YCC**	5.71	144.9
9	**Th-h245-YCC**	8.79	181.1
10	**Fe-h015-YCC**	13.27	258.7
11	**Fe-h123-YCC**	15.41	248.4
12	**Fe-h245-YCC**	17.12	263.9
13	**PR-h015-NCC**	12.34	258.7
14	**PR-h123-NCC**	13.92	269.1
15	**PR-h245-NCC**	14.57	263.9

All models provide good solutions in term of load-displacement curves. The effect of confinement and lateral cracking seems not to affect Feenstra model, whereas it leads to premature failure with Thorenfeldt one in association with higher bandwidths.

The model that provides the best accuracy is the parabolic-rectangle in combination with a crack bandwidth equal to h=$\sqrt{V}$=15mm ($P_{u,fem}$ / $P_{u,exp}$ =1.022, $\delta_{u,fem}$ / $\delta_{u,exp}$ = 1.036). Nevertheless it overestimates the stiffness after first cracking, whereas the same model with h = $S_{r,max}/2$ = 123mm underestimates it. A more correct approximation may be reached with a crack bandwidth 15<*h*<123mm.

Specimen *SB1* analyses results are shown in Figure 5.11(*a,b,c,d,e*).

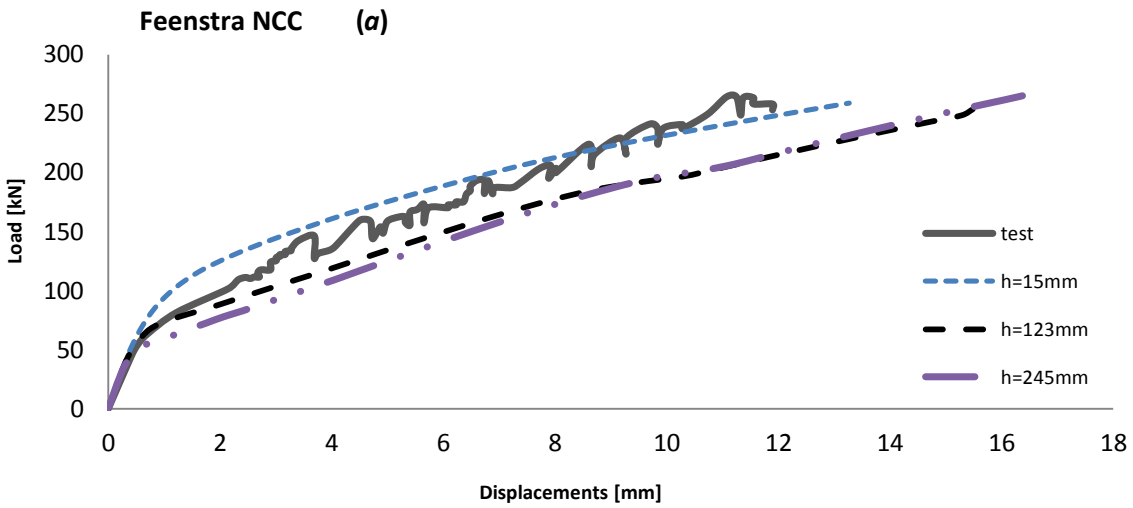

Figure 5.11 (*a*): Results of parametric analysis for *SB1* specimen using Feenstra model.

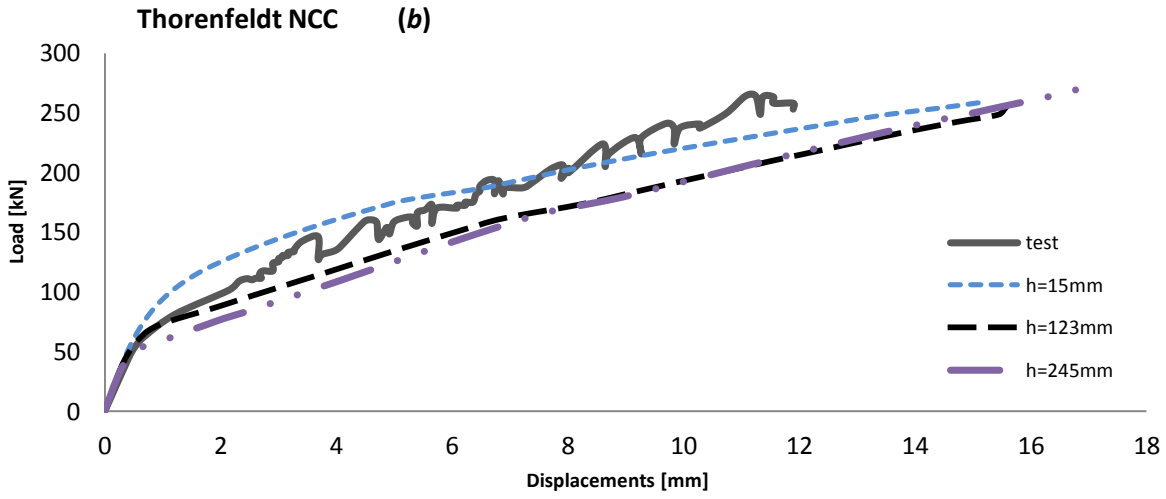

Figure 5.11 (*b*): Results of parametric analysis for *SB1* specimen using Thorenfeldt model.

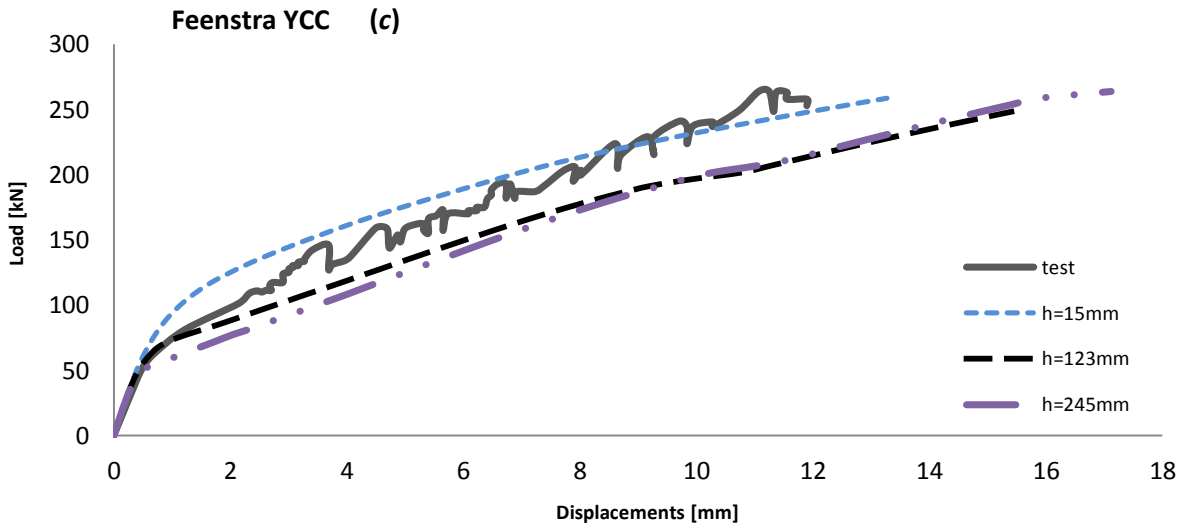

Figure 5.11 (*c*): Results of parametric analysis for *SB1* specimen using confined Feenstra model with lateral cracking.

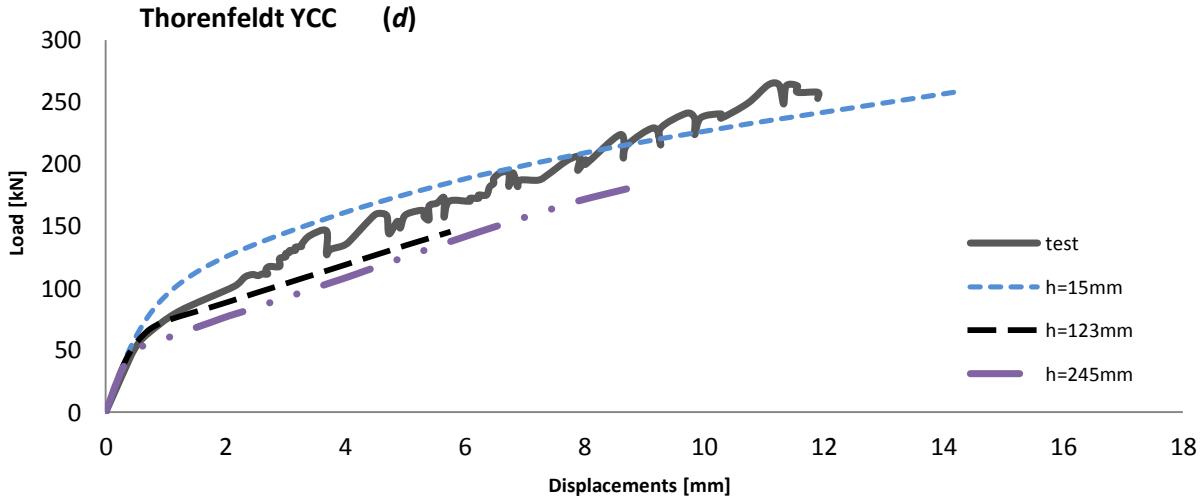

Figure 5.11 (*d*): Results of parametric analysis for *SB1* specimen using confined Thorenfeldt model with lateral cracking.

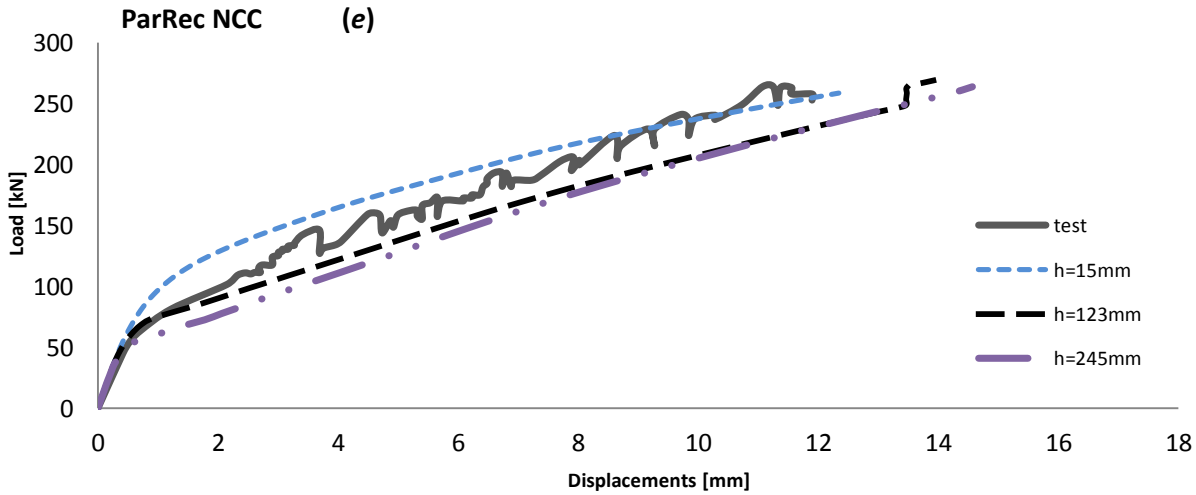

Figure 5.11 (*e*): Results of parametric analysis for *SB1* specimen using Parabola – Rectangle model.

The generic deformed shape of the slab prior to the sudden loss of capacity is illustrated in Figure 5.16 and clearly indicate failure in punching in every analysis as the slab above the column experienced vertical displacements, except for the ones that diverge before failure Compared to the vertical displacements that were observed from the experiment, the analysis is quite well corresponding.

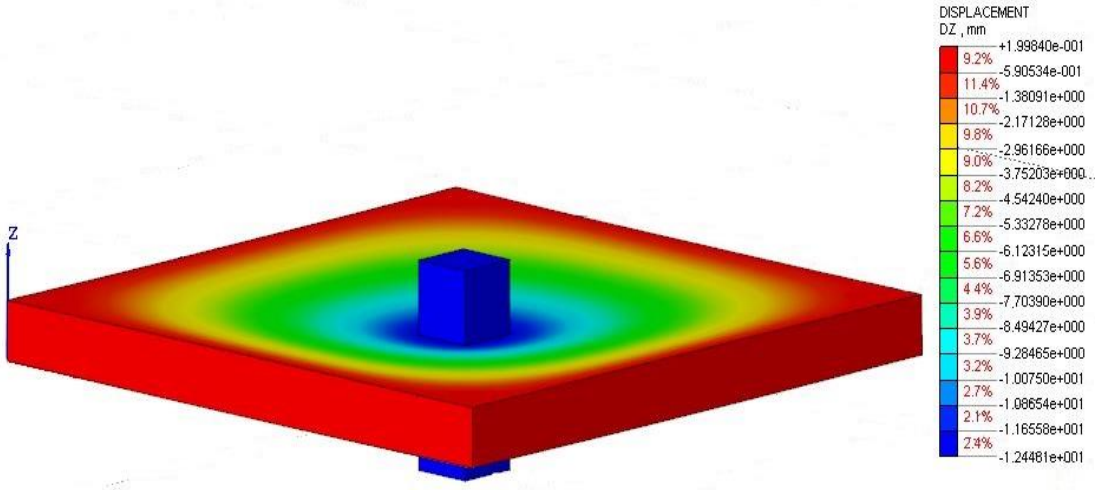

Figure 5.12: Displacements of specimen *SB1* during the last load step with h=15mm and EC2 compression model.

5.4 Results from analyses, specimen *no.2*.

Table 5.6 presents the final analysis results in terms of ultimate load-displacement for slab *no.2* in every combination made. The simulation gives brittle punching shear failure as in the experiment.

Table 5.6 Ultimate load and displacement for each combination, *no.2* specimen

	Specimen *no.2*	Ultimate displacement [mm]	Ultimate load [kN]
	Experimental	**20.11**	**123.3**
1	**Th-h015-NCC**	18.44	143.3
2	**Th-h123-NCC**	20.36	148.4
3	**Th-h245-NCC**	21.10	153.6
4	**Fe-h015-NCC**	19.52	138.2
5	**Fe-h123-NCC**	20.17	148.4
6	**Fe-h245-NCC**	22.12	153.6
7	**Th-h015-YCC**	16.82	138.2
8	**Th-h123-YCC**	21.36	158.7
9	**Th-h245-YCC**	21.83	133.1
10	**Fe-h015-YCC**	15.99	140.8
11	**Fe-h123-YCC**	22.61	158.7
12	**Fe-h245-YCC**	25.02	168.9
13	**PR-h015-NCC**	19.06	133.1
14	**PR-h123-NCC**	22.44	148.4
15	**PR-h245-NCC**	23.45	148.4

All models provide good solutions in term of ultimate load but relevant differences can be seen in term of ultimate displacements. The effect of confinement and lateral cracking seems to affect neither Feenstra nor Thorenfeldt model.

The model that provides the best accuracy ($P_{u,fem}$ / $P_{u,exp}$ =1.079, $\delta_{u,fem}$ / $\delta_{u,exp}$ =0.947) is the parabolic-rectangle in combination with a crack bandwidth equal to h=15mm that is the cubic root of the element's volume. Nevertheless it underestimates the stiffness after first cracking, and overestimates it before failure. A more correct approximation may be reached with a crack bandwidth $S_{r,max}$ /2 <h< $S_{r,max}$.

Specimen *nr.2* analysis results are shown in Figure 5.13(*a,b,c,d,e*).

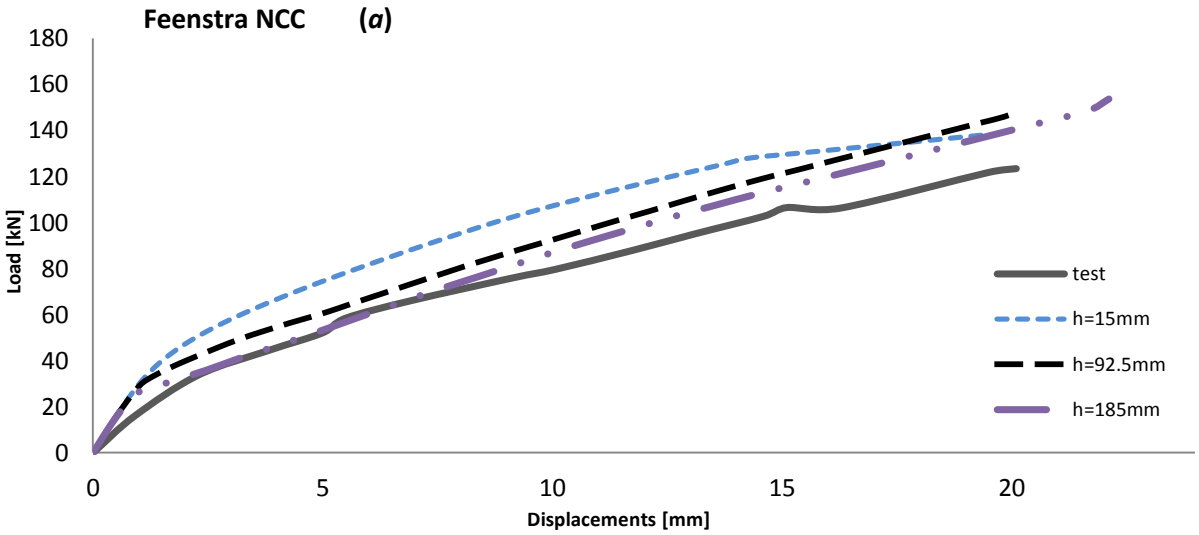

Figure 5.13 (*a*): Results of parametric analysis for *no.2* specimen using Feenstra model.

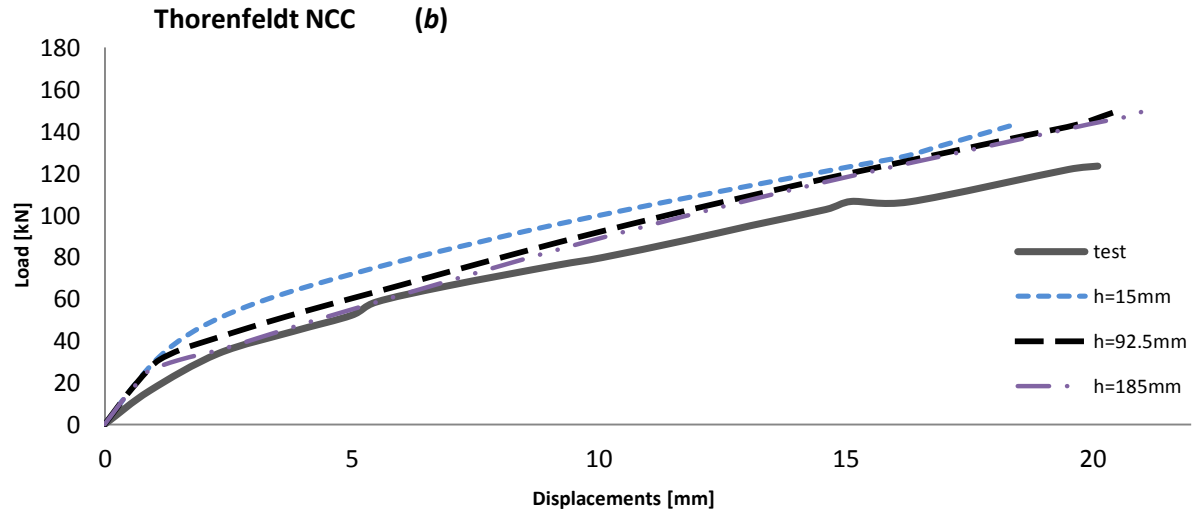

Figure 5.13 (*b*): Results of parametric analysis for *no.2* specimen using Thorenfeldt model.

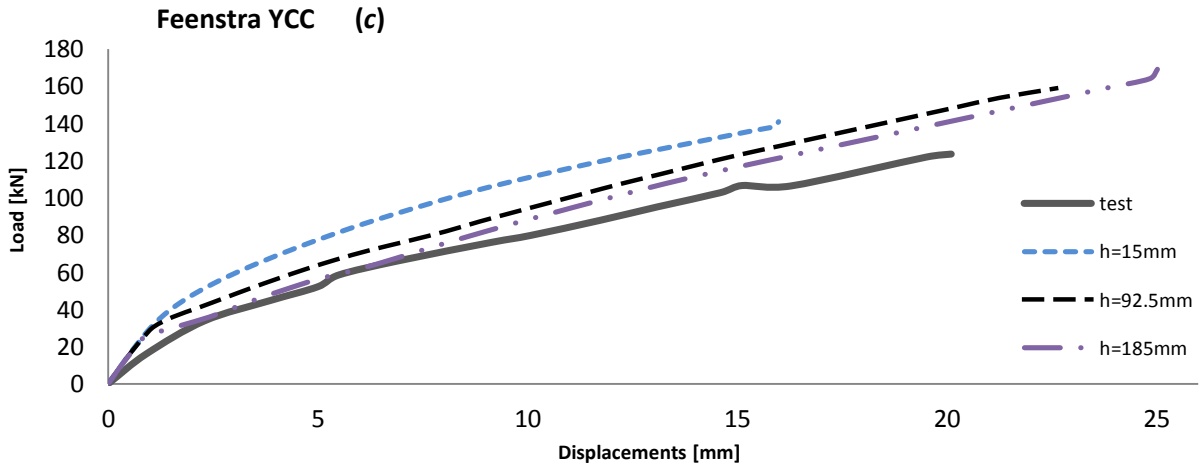

Figure 5.13 (*c*): Results of parametric analysis for *no.2* specimen using confined Feenstra model with lateral cracking.

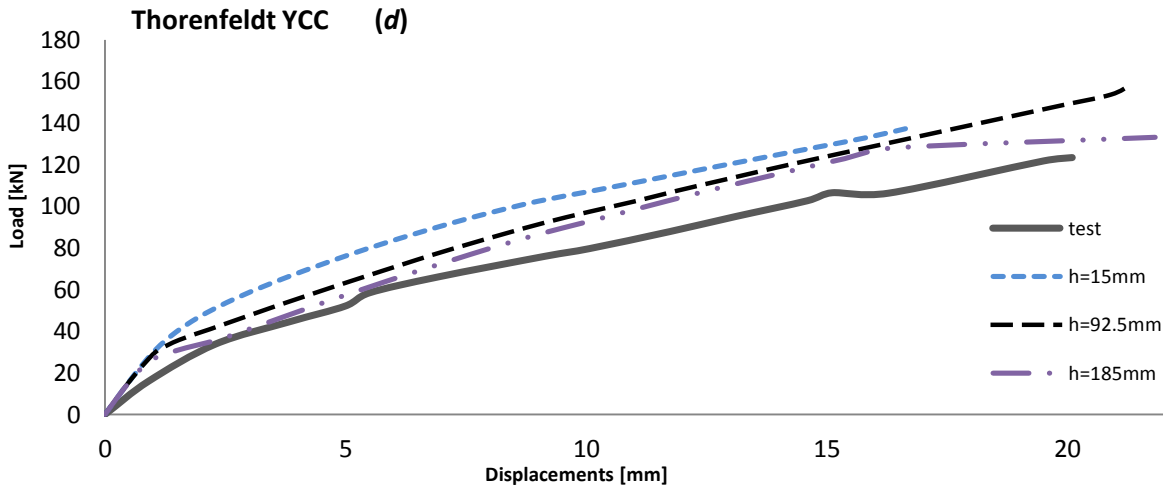

Figure 5.13 (*d*): Results of parametric analysis for *no.2* specimen using confined Thorenfeldt model with lateral cracking.

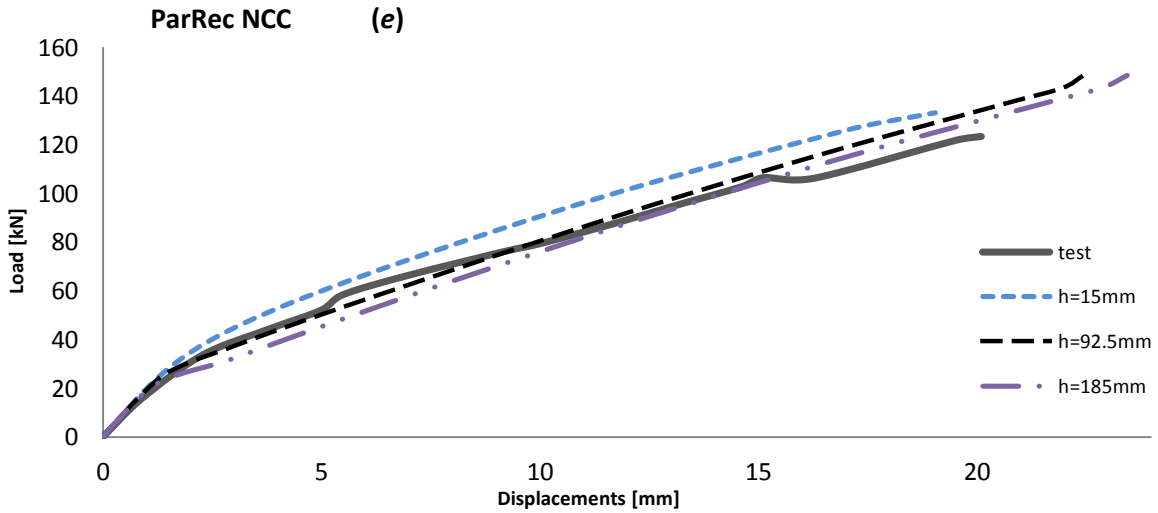

Figure 5.13 (*e*): Results of parametric analysis for *no.2* specimen using Parabola – Rectangle model.

The generic deformed shape of the slab prior to the sudden loss of capacity is illustrated in Figure 5.14 and clearly indicate failure in punching in every analysis as the slab above the column experienced vertical displacements, except for the ones that diverge before failure Compared to the vertical displacements that were observed from the experiment, the analysis is quite well corresponding.

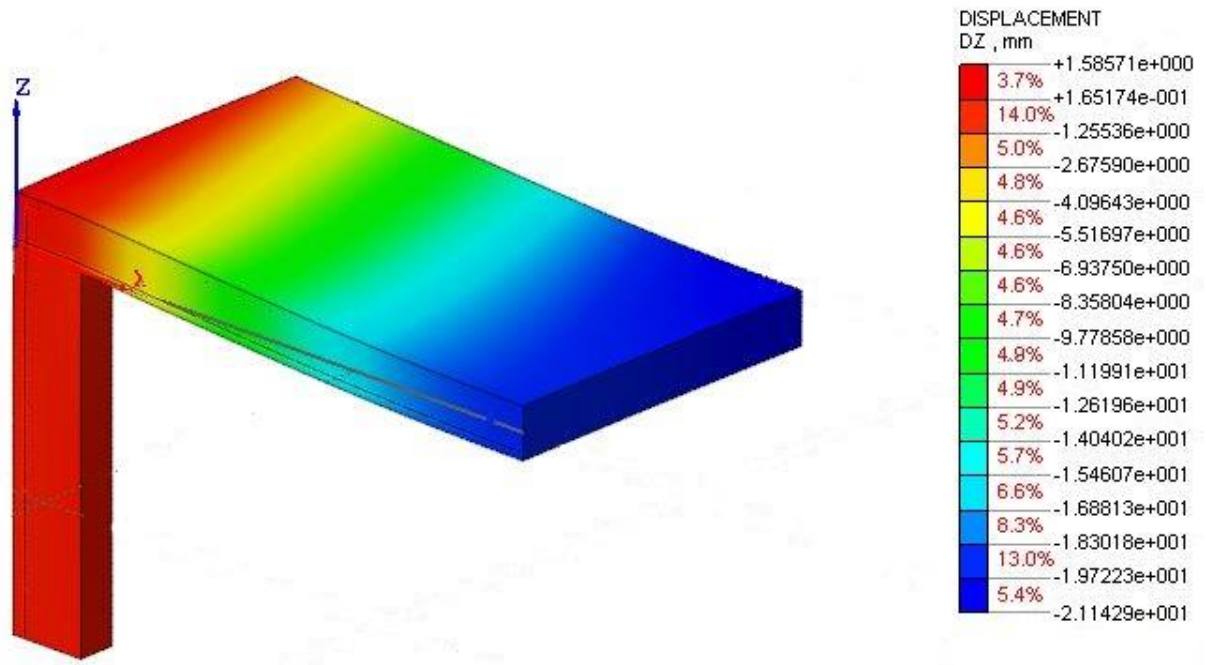

Figure 5.14: Displacements of specimen *no.2* during the last load step with h=15mm and EC2 compression model.

5.5 Results from analyses, specimen *R1*.

Table 5.7 presents the final analysis results in terms of ultimate load-displacement for slab *R1* in every combination made. The simulation gives brittle punching shear failure as in the experiment.

Table 5.6 Ultimate load and displacement for each combination, R1 specimen

	Specimen *R1*	Ultimate displacement [mm]	Ultimate load [kN]
0	**Experimental**	**20.95**	**106.8**
1	**Th-h015-NCC**	23.37	120.6
2	**Th-h065-NCC**	28.39	120.6
3	**Th-h130-NCC**	30.00	133.1
4	**Fe-h015-NCC**	19.05	120.6
5	**Fe-h065-NCC**	20.13	120.6
6	**Fe-h130-NCC**	21.12	124.8
7	**Th-h015-YCC**	17.89	116.4
8	**Th-h065-YCC**	19.77	120.6
9	**Th-h130-YCC**	20.41	124.8
10	**Fe-h015-YCC**	20.22	124.8
11	**Fe-h065-YCC**	20.34	108.1
12	**Fe-h130-YCC**	22.00	108.1
13	**PR-h015-NCC**	20.87	116.4
14	**PR-h065-NCC**	22.76	120.6
15	**PR-h130-NCC**	23.29	120.6

All models provide good solutions in term of ultimate load but tend to underestimate the ultimate displacement. The effect of confinement and lateral cracking seems to have nil effect on Feenstra model and very little on Thorenfeldt one.

The model that provides the best accuracy ($P_{u,fem}$ / $P_{u,exp}$ =1.089, $\delta_{u,fem}$ / $\delta_{u,exp}$ =0.996) is the parabolic-rectangle in combination with a crack bandwidth equal to h=15mm that is the cubic root of the element's volume. Nevertheless it underestimates the stiffness after first cracking, and the ultimate displacement.

Specimen *R1* analysis results are shown in Figure 5.15(*a,b,c,d,e*).

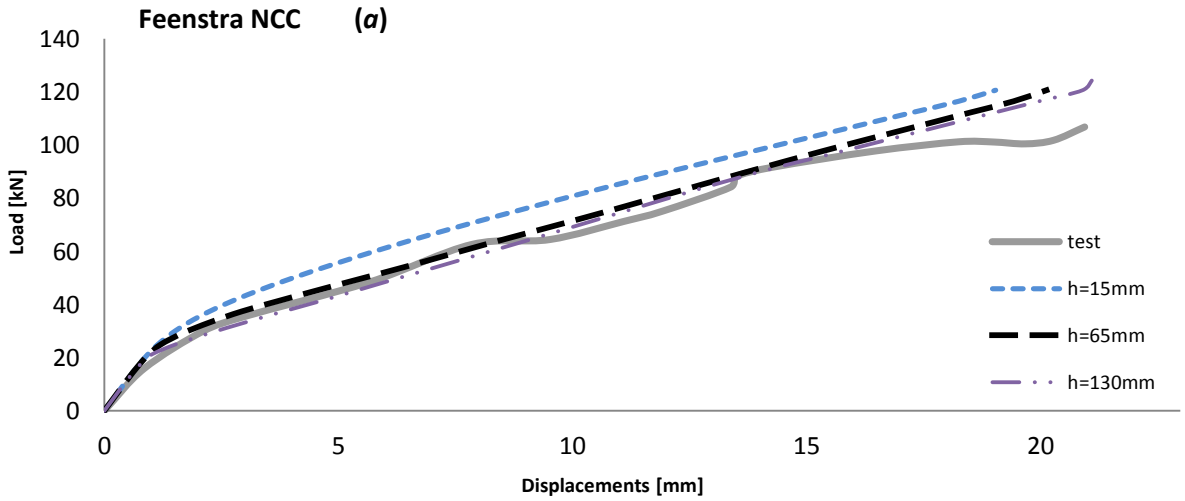

Figure 5.15 (*a*): Results of parametric analysis for *R1* specimen using Feenstra model.

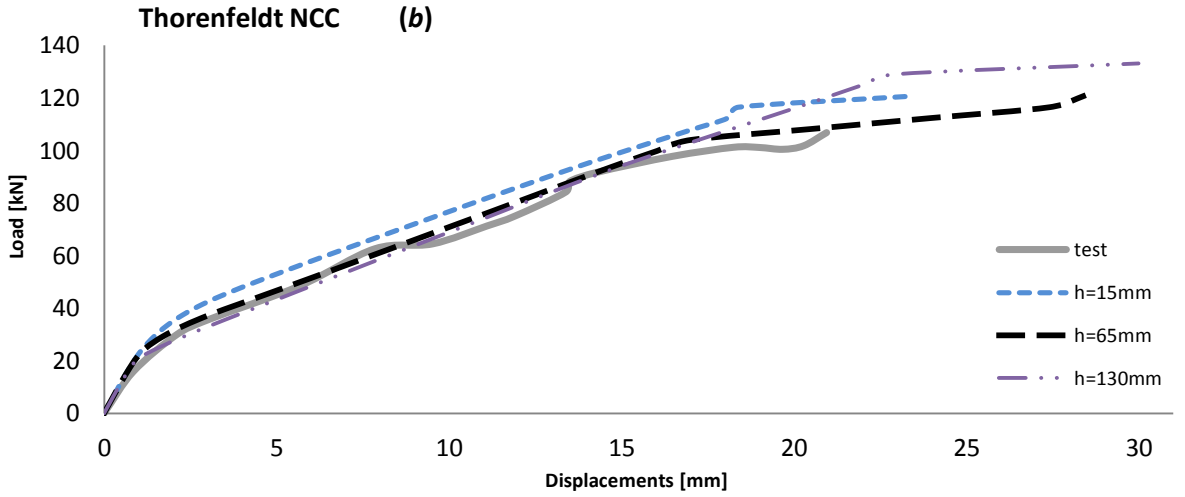

Figure 5.15 (*b*): Results of parametric analysis for *R1* specimen using Thorenfeldt model.

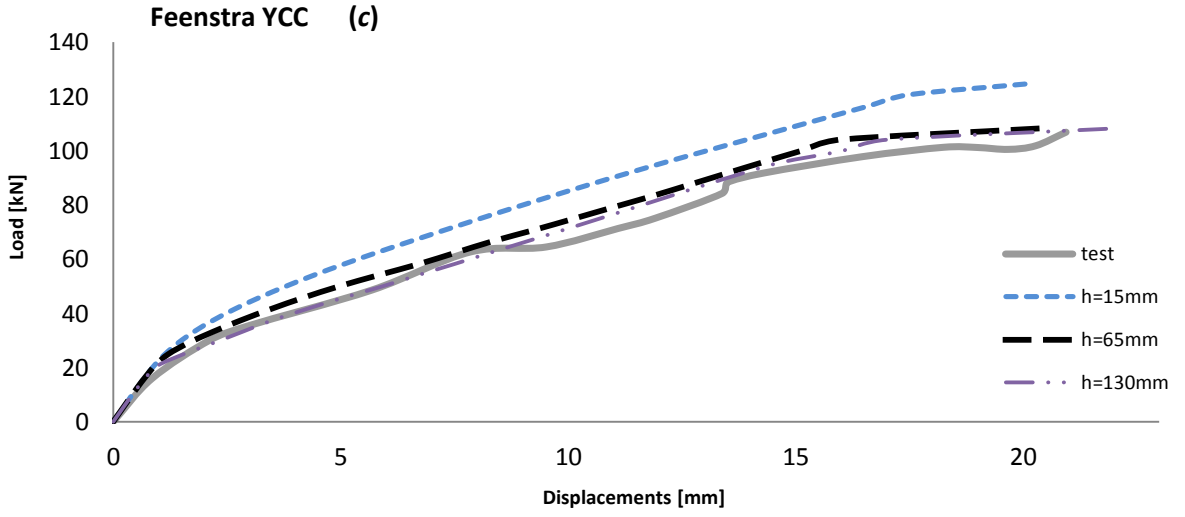

Figure 5.15 (*c*): Results of parametric analysis for *R1* specimen using confined Feenstra model with lateral cracking.

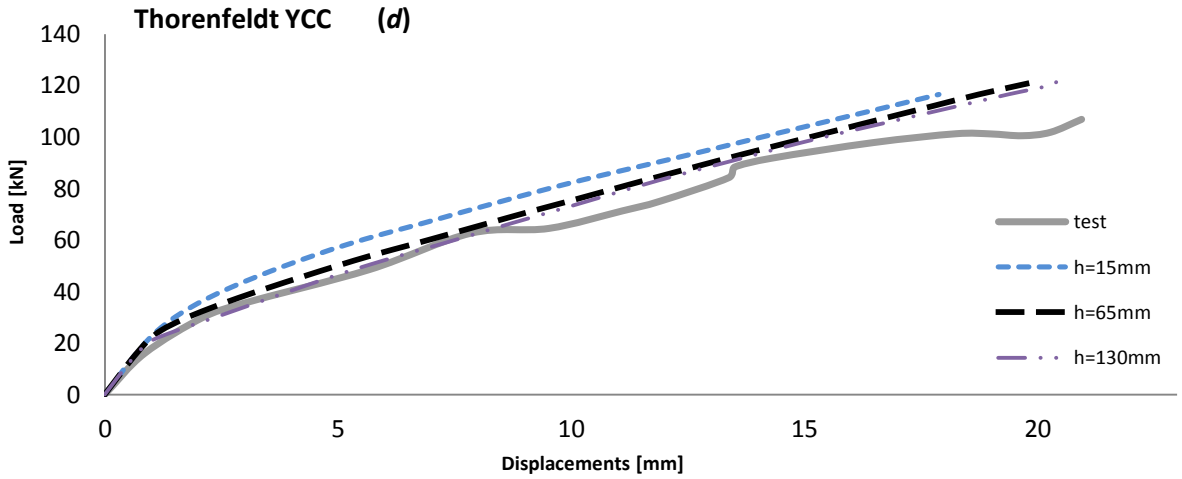

Figure 5.15 (*d*): Results of parametric analysis for *R1* specimen using confined Thorenfeldt model with lateral cracking.

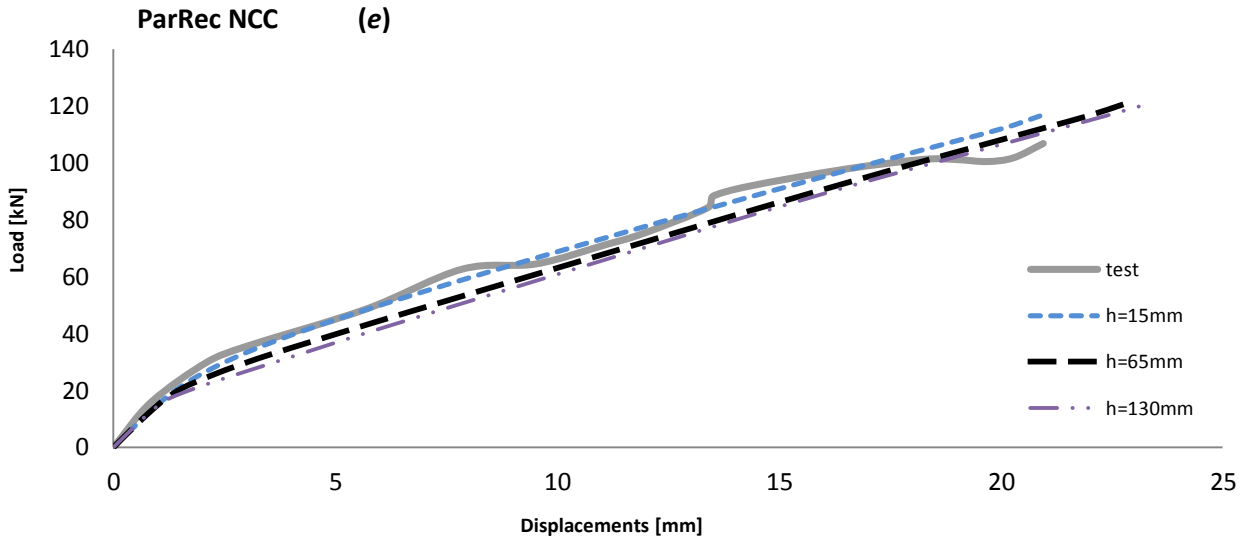

Figure 5.15 (*e*): Results of parametric analysis for *R1* specimen using Parabola – Rectangle model.

The generic deformed shape of the slab prior to the sudden loss of capacity is illustrated in Figure 5.16 and clearly indicate failure in punching in every analysis as the slab above the column experienced vertical displacements, except for the ones that diverge before failure Compared to the vertical displacements that were observed from the experiment, the analysis is quite well corresponding.

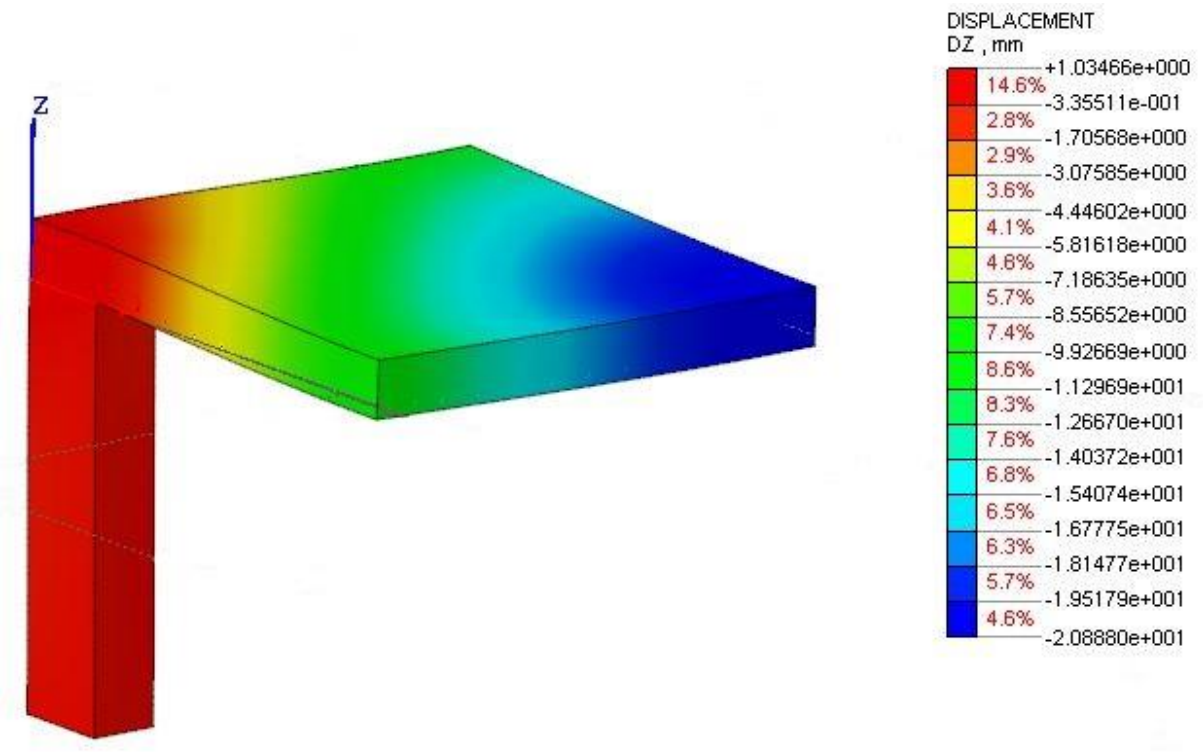

Figure 5.16: Displacements of specimen *R1* during the last load step with h=15mm and EC2 compression model.

5.6 Validation of code provisions and new model

The shear punching strength predictions of all tested beams obtained with nonlinear analysis have been compared with experimental results, all FEA values have been divided by experimental failure load in Table 5.7, furthermore, three current structural codes (EC-2, Model Code 2010, ACI-318-08) and the proposed model seen in 3.2.2 have been compared with experimental results, to see which one is able to better predict specimen's behaviour, Figure 5.17. All explicit partial safety factors have been removed from the original formulations, and the mean value of the materials strength has been used for these calculations. The proposed model correlates significantly better with the tests results than any of the three considered code formulations.

Table 5.7 Comparison between ultimate load predicted by FEA and code predictions.

	$P_{uFEA} / P_{u,exp}$			$\delta_{uFEA} / \delta_{u,exp}$		
Analysis	*SB1*	*No.2*	*R1*	*SB1*	*No.2*	*R1*
Th-h$\sqrt{\mathbf{V}}$-NCC	1,02	1,16	1,13	1,27	0,92	1,12
Th-hS_{rmax}/2-NCC	1,00	1,20	1,13	1,31	1,01	1,36
Th-hSr_{max}-NCC	1,06	1,25	1,25	1,33	1,05	1,43
Fe-h$\sqrt{\mathbf{V}}$-NCC	1,02	1,12	1,13	1,12	0,97	0,91
Fe- hS_{rmax}/2-NCC	1,00	1,20	1,13	1,30	1,00	0,96
Fe- hSr_{max} -NCC	1,06	1,25	1,17	1,41	1,10	1,01
Th- h$\sqrt{\mathbf{V}}$-YCC	1,02	1,12	1,09	1,20	0,84	0,85
Th- hS_{rmax}/2-YCC	0,57	1,29	1,13	0,48	1,06	0,94
Th- hSr_{max} -YCC	0,72	1,08	1,17	0,74	1,09	0,97
Fe- h$\sqrt{\mathbf{V}}$-YCC	1,02	1,14	1,17	1,12	0,80	0,97
Fe- hS_{rmax}/2-YCC	0,98	1,29	1,01	1,29	1,12	0,97
Fe- hSr_{max} -YCC	1,04	1,37	1,01	1,44	1,24	1,05
PR- h$\sqrt{\mathbf{V}}$-NCC	1,02	1,08	1,09	1,04	0,95	1,00
PR- hS_{rmax}/2-NCC	1,06	1,20	1,13	1,17	1,12	1,09
PR- hSr_{max} -NCC	1,04	1,20	1,13	1,22	1,17	1,11

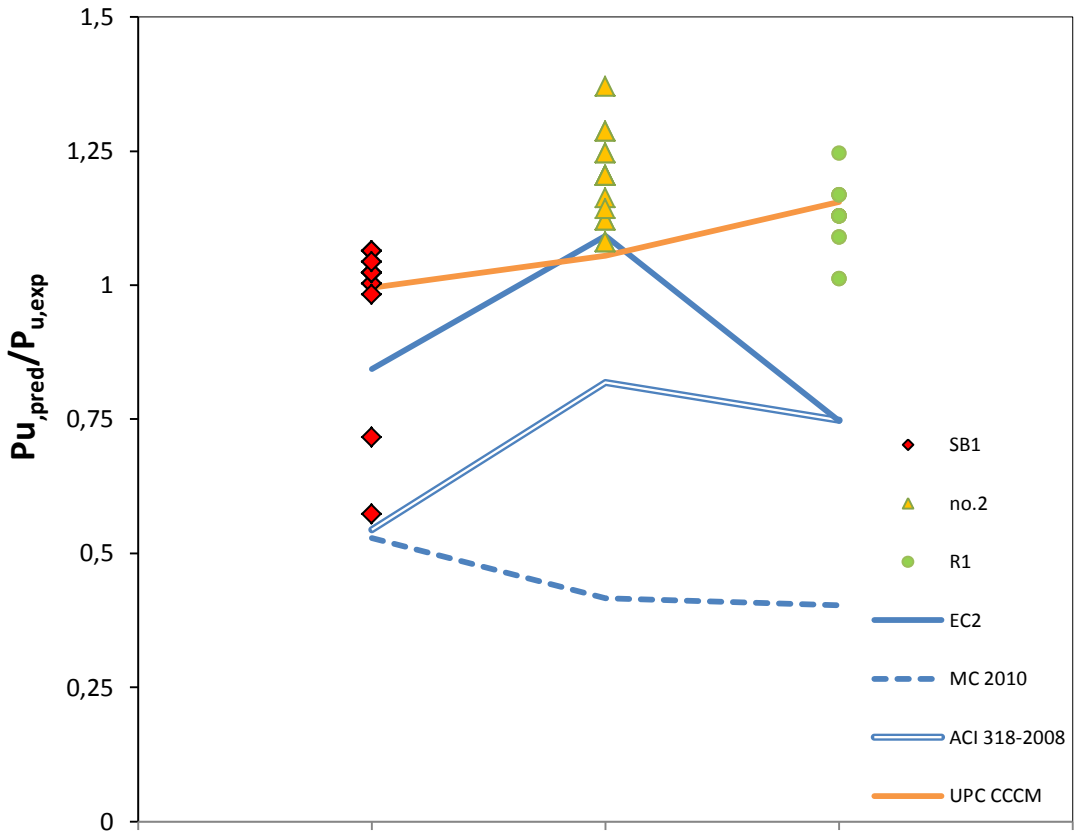

Figure 5.17: Ratio between predicted failure load by FEA, and codes and experimental result.

Chapter 6

Conclusions

Nonlinear finite element analyses have been conducted in order to assess the structural behaviour with respect to punching shear of flat. The simulation of the test specimens *SB1, R1* and *No. 2* showed good correspondence to the observations from the experiments.

However, certain observations were made, namely;

- The FE-analyses showed a somewhat stiffer response than the conducted experiments. This is believed to derive from the smeared crack formulation that is used in the concrete model.
- The ultimate load was very well corresponding to reality, although predicted deformations tends to be much larger than experimental. This might be due to the inability of the FE-analysis to simulate fracture between the elements.
- An higher crack bandwidth value provides much elasticity to the model, its value should be chosen in between cubic root of elements volume and a half of maximum crack spacing.
- For design purposes software for 3D analysis have good reliability, but their results must be supported by previous analysis conducted with traditional methods.
- A simplified compression model for concrete, as the Parabola-Rectangle, is able to provide a good ultimate displacement and fit the experimental results even better than more complex models.
- The predictions of compression chord capacity model fit very well the experimental results and also with FEA results. The mechanical character of the model provides valuable information about the physics of the problem and incorporates the most relevant parameters governing the shear strength of structural concrete members. Due to this fact and the simplicity of the derived equations it may become a very useful tool for structural design and assessment in engineering practice.

Chapter 7

Literature references

[1] Wood J. G.M. Pipers Row Car Park, (2002) Wolverhampton Quantitative Study of the Causes of the Partial Collapse on 20th March 1997, SS&D Contract Report to HSE http://www.hse.gov.uk/research/misc/pipersrowpt1.pdf

[2] Salem H., Issaa H., Gheith H., Farahata A., (2012) Punching shear strength of reinforced concrete flat slabs subjected to fire on their tension sides. HBRC Journal, Vol. 8, No. 1, pp. 36-46.

[3] King, S., and Delatte, N. (2004). "Collapse of 2000 Commonwealth Avenue: Punching Shear Case Study." J.Perform.Constr.Facil., 18(1), 54-61.

[4] Kinnunen, S., Nylander, H. (1960): Punching of Concrete Slabs Without Shear Reinforcement. Transactions of The Royal Institute of Technology, No.158, Stockholm, Sweden, 1960, 112 pp.

[5] Kinnunen, S. (1971): Försök med betongplattor understödda av pelare vid fri kant. Statens institut för byggnadsforskning, Rapport R2, Stockholm, 1971, 103 pp.

[6] Broms, C. E., (1990): Punching of flat plates – a question of concrete properties in biaxial compression and size effect. ACI Structural Journal, Vol. 87, No. 3, May-June 1990, pp. 292-300.

[7] Guandalini, S., Burdet, O.L. and Muttoni, A., 2009, "Punching Tests of Slabs with Low Reinforcement Ratios," ACI Structural Journal, ACI, V. 106, No. 1, pp. 87-95.

[8] Cladera, A., Marí, A., Bairán, J. M., Ribas, C., Oller, E. and Duarte, N. (2016), The compression chord capacity model for the shear design and assessment of reinforced and prestressed concrete beams. Structural Concrete, 17: 1017–1032. doi:10.1002/suco.201500214.

[9] Muttoni, A., 2008, "Punching Shear Strength of Reinforced Concrete Slabs without Transverse Reinforcement," ACI Structural Journal, V. 105, No. 4, pp. 440-450.

[10] European Committee for Standardization. Eurocode 2: Design of Concrete Structures: Part 1: General Rules and Rules for Buildings. 2002.

[11] Fédération Internationale du Béton (fib). (2010). Shear and punching shear in RC and FRC elements. fib Bulletin 57.

[12] ACI Committee 318, 2008, Building Code Requirements for Structural Concrete (ACI 318-08) and Commentary, American Concrete Institute, Farmington Hills, MI, 465 pp.

[13] Gardner, N.J., 2005, "ACI 318-05, CSA A.23.3-04, Eurocode 2 (2003), DIN 1045-1 (2001),BS 8110-97 and CEB-FIP MC 90 Provisions for Punching Shear of Reinforced Concrete Flat Slabs," SP-232, Ed. Polak, M.A., American Concrete Institute, Farmington Hills, MI, pp.1-22.

[14] FIP 12. Punching of structural concrete slabs. CEB-FIP task group. Lausanne (Switzerland), 2001.

[15] Yu, Q., Le. J.L., Hubler, M.H., Wendner, R., Cusatis, G. and Bažant, Z.P.: Comparison of Main Models for Size Effect on Shear Strength of Reinforced and Prestressed Concrete Beams, Northwester University, Structural Engineering Report No. 15-03/936x, 2015, 29 pp.

[16] Zararis, P.D. and Papadakis, G.C.: Diagonal shear failure and size effect in RC beams.

[17] Hasegawa, T., Shioya, T. and Okada, T.: Size effect on splitting tensile strength of concrete. In Proceedings 7th JCI Conf. Japan Concr. Inst., Tokyo, 1985, 309–312.

[18] Bažant, Z.P., Hasegawa, M.T. and Mazars, J.: Size Effect in Brazilian Split-Cylinder Tests: Measurements and Fracture Analysis. Mater J, 1991, 88, 325–332.

[19] Bažant, Z.P., Yu, Q., Gerstle, W., Hanson, J. and Ju, J.W.: Justification of ACI 446 Proposal for Updating ACI Code Provisions for Shear Design of Reinforced Concrete Beams. ACI Struct J, 2007, 104, 601–610.

[20] L. Franzens, Critical review of EC2 regarding punching and improving the design approach, Ph.D. Dissertation, Univ. of Innsbruck, 2014.

[21] Broo, H., Lundgren. K., Plos, M. (2008) A guide to non-linear finite element modelling of shear and torsion in concrete bridges. Department of Civil and Environmental Engineering, Chalmers University of Technology, Report 2008:18, Göteborg, Sweden, 2008, 27 pp.

[22] Thorenfeldt, E., Tomaszewicz, A., and Jensen, J. J., Mechanical properties of high-strength concrete and applications in design, In Proc. Symp. Utilization of High-Strength Concrete (Stavanger, Norway) (Trondheim, 1987), Tapir.

[23] Vecchio, F. J., and Collins, M. P., Compression response of cracked reinforced concrete, J. Str. Eng., ASCE 119, 12 (1993), 3590–3610.

[24] Thorenfeldt, E., Tomaszewicz, A., and Jensen, J. J., Mechanical properties of high-strength concrete and applications in design, In Proc. Symp. Utilization of High-Strength Concrete (Stavanger, Norway) (Trondheim, 1987), Tapir.

[25] FEENSTRA, P. H., Computational Aspects of Biaxial Stress in Plain and Reinforced Concrete, PhD thesis, Delft University of Technology, 1993.

[26] Hordijk, D. A. Local Approach to Fatigue of Concrete. PhD thesis, Delft University of Technology, 1991.

[27] J. Oliver, M. Cervera, S. Oller, Isotropic damage models and smeared crack analysis of concrete., Proceedings of SCI-C 1990 (1990) 945–958.

[28] Adetifa B, Polak MA. Retrofit of slab column interior connections using shear bolts. ACI Struct J 2005;102(2):268–74.

[29] Ingvarsson, H. (1977): Betongplattors hållfasthet och armeringsutformning vid hörnpelare (Load-bearing capacity of concrete slabs and arrangement of reinforcement at corner columns). Department of Structural Engineering, The Royal Institute of Technology, Meddelande Nr 122, Stockholm, Sweden, 1977, 143 pp.